16)

Control of the Growth Interface Location and Morphology in Vertical Bridgman Geometries

by

Satyavolu Srinivas Papa Rao

Bachelor of Technology (Metallurgical Engineering)
Indian Institute of Technology, Madras
(1988)

Submitted to the Department of Materials Science and Engineering
on May 3, 1996 in Partial Fulfillment of the Requirements for the Degree of

Doctor of Philosophy

at the
Massachusetts Institute of Technology
June 1996

Signature of Author............... ....
Department of Materials Science and Engineering
May 3, 1996

Certified by............. ....
August F. Witt
Thesis Supervisor

Accepted by...................... ....
Michael F. Rubner
TDK Professor of Materials Science and Engineering
Chair, Departmental Committee on Graduate Students

Control of the Growth Interface Location and Morphology in Vertical Bridgman Geometries

by

Satyavolu Srinivas Papa Rao

Submitted to the Department of Materials Science and Engineering
on May 3,1996 in Partial Fulfillment of the Requirements
for the Degree of Doctor of Philosophy in Electronic Materials

Abstract

In conventional vertical Bridgman crystal growth furnaces, the location of the crystal-melt interface with respect to the furnace, and its shape, change during growth. Interface relocation is due to changing thermal coupling between the furnace and the charge during translation of the charge, and it affects the radial dopant segregation, stresses, facetting, increases polycrystallinity, and causes the growth rate to diverge from the translation rate. Interface relocation transients are accentuated, and prevail over the entire course of the run, for short charge lengths.

Interface location control was incorporated in the design of a heat-pipe based vertical Bridgman growth system. The temperature at two closely spaced points within the gradient zone is sensed. This information is used by two independant feedback loops to control the heater power in the hot and cold zones, in order to keep the melting point isotherm at a fixed location between the control points. Interface relocation is thus prevented by automatically compensating for transient thermal effects seen in conventional furnaces during growth, through appropriate changes in power input to the heaters.

With a graphite dummy to mimic a crystal charge in the gradient freeze growth mode, thermal field stabilization was demonstrated at typical growth rates (3 cm/hr). It was shown that gradients as low as 5°C/cm could be sustained over conventional crystal growth lengths. Thermal studies (with a BN dummy) in the conventional Bridgman configuration established the importance of gradient zone design and related radial heat fluxes, as well as the techniques for proper temperature measurement therein. The ability to control the thermal field within the gradient zone at typical growth rates was demonstrated, when the afore-mentioned control modifications were utilized.

Gallium doped germanium (seeded in the <111> orientation) was grown in the Bridgman mode, with the temperatures within the gradient zone being stabilized as described above. Growth rate measurements show that, following an initial transient, the growth interface location is held constant.

Radial and axial dopant segregation measurements showed that a toroidal convective flow exists near the interface. The interface shape was found to be tilted by 1.5°, but this asymmetry was not noticeably reflected in the radial segregation behavior. Axial segregation data showed that the k_{eff} decreased from 0.1 to 0.083 as the melt aspect ratio shrank from 5:1 to 2:1. An increase in striation contrast was observed along the growth direction. No evidence was seen of extended facet formation at any radial position. Most crystals showed spurious nucleation at the crucible wall (graphite and quartz). These grains extended into the bulk of the crystal during growth, resulting in polycrystallinity (with fewer than 3 crystallites, typically). The interface demarcation lines were found to be continuous across the grains. The polycrystallinity was found not to interfere with growth or segregation behavior studied in this work.

The support of the Intel Foundation, the National Science Foundation and of the National Air and Space Administration is gratefully acknowledged.

Thesis Supervisor: August F. Witt
Title: Ford Professor of Engineering, MacVicar Faculty Fellow

Table of contents

List of Figures and Tables

Acknowledgments

I would like to thank Professor Witt for guiding me so skilfully over the years. I am still amazed at how patiently he worked to educate me - and how optimistic he has been that I *would* become a productive member of the research fraternity. I have the duty to always produce research of high enough quality, and of improving over time, to ensure I remain counted as one of the students he has advised. I hope always to apply the principles that he has taught me to bring to research - meticulousness of experiment design, thoroughness of preparation, "parallel processing" of research ideas, fertility of imagination, elegance of presentation, and wry humor. I have yet to figure out his uncanny ability to divine what I was thinking just by looking at me - that would be useful gift to have! I thank Professor Kimerling, and Professor Mikiç for being on my thesis committee and giving me the benefit of their expertise, and particularly for being so patient with me!

I would also like to thank Dr. Manfred Lichtensteiger for appearing magically when my spirits hit their lowest spots, and just as magically helping me out of the doldrums. It was instructive to watch his lightning mind at work - anticipating problems keenly or solving them elegantly. Dr. Piotr Becla is another person who has inspired me over the years with the way he works miracles in the lab. I wish I had started working closely with him right from my first day at MIT. Someday, I hope, I too will have a lithography setup in my basement! Dr. Shahryar Motakef is a person who somehow radiated camaraderie toward graduate students even though he was a professor at MIT - I do thank him for all his advice, the energetic discussions we had, and for the depth of his concern over my progress.

Dr. Xuezhong Cao, Dr. Doug Carlson, Dr. Craig Counterman, Dr. Chenting Lin, and Dr. Michael Wargo have all helped me so much in so many ways over so many years that I do hope they don't expect me to requite even a fraction of the debt I owe each of them!

I don't have enough words to express my regard for Ms. Gloria Landahl. She had the most untiring ear for all my songs of despair, and was the most uncomplaining recipient of my hurrahs when things went well. I also have to thank her for taking the time to teach me American pronunciation, for introducing me to my first Thanksgiving, to cats and New England - not that they go together, even if it might seem like it to my foreign eyes. I would also like to thank John DiFrancesco for all the help he has given me - in spite of my seeming efforts to foil him at his task, with mistakes in my drawings and so on. His (off-!)Broadway renditions made life, shall I say, interesting?

My roommates, John Paul Mattia and Thomas Lee, have borne the brunt of many troubled, 'Pops-is-talking-in-his-sleep-again-#@&%!*", nights - and are kind enough to remain my friends! They and Richard Stone are responsible for teaching me about music, and how books ought to mulled over. Richard can rest easy knowing that he has talked the last vestiges of liberalism out of me. I thank David & Lynn Chalfoun, their cats, Kirsten Bremke, and JP, among others, for making me such a part of their families, even. My cousins, Anupa & Ashutosh Rao, and my undergrad friends, V. Mahadev and S. Karthik took able care of the long-distance therapy-for-Papa Rao department. Ashdown House, Tan Trinh, and my other fencing pals, Huey Pin Ng, Yee Chuan Koh, Beethoven Cheng, and other badminton friends, Brad and Lam Bauman, Anil Chakravarty, Karin Ellison, Jim Foresi, Laura Giovane, Diane Ho, Prof. Vernon & Beth Ingram, Young-Chang Joo, Shane &JeeHoon Krska, Serena Losonczy, Josephine Louie, John Matz, Kathy Misovec, Charles Pieczulewski, Srikanth Samavedam, Julie Tsai, Anne Townes, Yu Zheng – they made the years so interesting. I know I haven't made a dent in the list of friends that are so important to me - but I hope to be forgiven for stopping here, and thanking them in person later.

I thank Daphne Png for all the friendship she is so kind to bestow on me, and for the warmth, sweetness and light she radiates to all around her. Her smiling, level-headed nature has been a wonderful and steadying influence, for which I am very thankful.

I thank my parents, Shri. Seshagiri Rao and Shrimati. Ratnamala, for bringing me up so expertly, against all odds! I thank my brother, Devesh, for his love and support, and for his forbearance in not telling me I seem to be taking forever to get my Ph.D. I am blessed to have parents and a brother such as they! I thank God for everything.

The support of the Intel Foundation (through the Graduate Fellowship Program), the National Science Foundation (NSF), and of the National Air and Space Administration (NASA), which supported this research continuously, through thick and thin, is gratefully acknowledged.

Chapter 1 Introduction

In this Introduction, the importance of crystal growth to substrate properties and ultimately to device performance is adumbrated. The crystal-melt interface is an important crystal growth parameter. The mechanics of how the interface impacts crystal properties are outlined, and the benefits to be gained by controlling its location and shape are presented.

Crystal growth techniques have been around for so long, it seems incongruous that, as recently as 1963, a book could bear the title "The *Art* and Science of Growing Crystals"[1]. While it might have been true that, at that point of time, empirical approaches to crystal growth were dominant, the microelectronic revolution, with its relentless drive towards scaled-down device dimensions, has since spurred intense research into the science of crystal growth. It is hoped that this thesis will be considered a contribution towards narrowing the gap between theory and experiment that still exists.

As device dimensions approach (and even exceed) defect dimensions, a device is more likely to be fatally affected by the presence of a defect. Hence, as device dimensions have shrunk, defect tolerances in chip fabrication have been lowered, to maintain high chip yields. A semiconductor wafer that has been sliced from the boule will find use either as a substrate for the epitaxial growth of active layers (within which devices are fabricated), or it may have devices fabricated directly on its surface (by ion-implantation, as in GaAs monolithic microwave IC fabrication). If the devices are fabricated in an epilayer, it has been found that defects in the substrate - threading dislocations, for example - propagate into the epilayer. It has to be kept in mind that, while the use of an epilayer places the devices in a layer grown with better property controls, it increases the cost of the chip. So, it would confer a competitive advantage to a manufacturer whose crystal growth technology is able to produce wafers of high enough quality not to need epilayer growth prior to device fabrication. If the device fabrication proceeds without an epilayer being grown, the substrate properties - resistivity, dislocation density, trap density and so on - are clearly important.

The influence of defects on device performance is well-documented. The presence of dislocations in the GaAs substrate affects the threshold voltage of nearby MESFET's[2], causing problems in chip yield. Oxygen content of silicon wafers needs to be controlled, for optimal results to be obtained through the intrinsic gettering process, where a denuded zone is formed at the top surface of the wafer, and fine oxide precipitates (gettering sites) are formed throughout the bulk of the wafer. The oxygen content of the wafer has to be within certain limits to increase resistance of the wafer to warpage during processing (the strengthening comes both from solution hardening and from dislocation pinning at the precipitates). Oxide precipitates, 'swirl'[3] and 'haze' defects in silicon wafers can be nucleation points for oxidation-induced stacking faults (OISF's). Trace levels of metal contamination increase leakage currents across junctions and adversely affect the behavior of DRAM chips, for example[4]. Point defects and clusters of point defects affect the minority carrier lifetime - the thermal history that the crystal experiences affects point defect density and distribution. Resistivity variation across the diameter of a silicon wafer needs to be controlled (typically, to less than 10%). Changes in dopant segregation from wafer to wafer are also undesirable, from the quality control standpoint. Random fluctuations in dopant concentration on the microscopic scale on a wafer can have deleterious effects on chip yield.

The origins of the various defects during crystal growth need to be understood, if the formation of defects is to be controlled. Considerable understanding has been gained over the past 15 years, about dislocation generation during crystal growth and cool-down. The availability of high performance computing has made it possible to employ extensive finite element models to study convection patterns in the melts of different crystal growth techniques, and to understand the nature of radial and axial segregation, and of microsegregation. In GaAs crystal growth, the influence of melt stoichiometry and other crystal growth parameters on the distribution of the EL2 defect, and on implant activation behavior is being understood more clearly. Still, there are many unanswered questions in the science of crystal growth. But there is as much work that needs to be done to advance the engineering aspects of crystal growth[5]. Control of crystal growth processes is an area of burgeoning importance. Processes need to be designed that are more robust, more reproducible, with higher degrees of automation and capable of benefitting from modeling input - whether real-time or off-line.

An important issue in Bridgman geometries is control over the interface - its location within the furnace, its constancy during growth, and its shape. Many of the past improvements in crystal growth technology can be viewed as efforts that primarily target crystal-melt interface control, to gain a variety of benefits. Several theoretical analyses, both analytical and numerical, have dwelt on the interrelationship between the interface shape and radial dopant segregation characteristics, and on the relationships between the thermal fields in the charge, the interface, and the defect densities in the grown crystal. These analyses point to the need for improved interface control in growth systems in general and in vertical Bridgman furnaces in particular.

Control over the interface location would mean confidence, *a priori*, of the seeding point, without the need for trial and error every time a change is made, say, in ampoule design or even in the nature of the furnace insulation. Interface control would mean that the actual growth rate equals the chosen ampoule translation rate for the entire duration of the run. One can be confident that the axial thermal gradients in the vicinity of the interface are under control - which can be used to advantage in control of constitutional supercooling. Constitutional supercooling[6] is an important constraint that defines the condition when spurious nucleation can occur ahead of the growth interface. It is a constraint that is particularly important during the growth of alloy semiconductors alloys like Si_xGe_{1-x}. Knowledge of the interface shape, when coupled with control over its location, could even be used to control the radial segregation over a growth run. It would even be possible to use a thin fiber bundle, sent in through the gradient zone, to monitor the interface since the interface is localized to within a small extent during the entire growth run.

In this thesis, control over the crystal-melt interface location in a vertical Bridgman geometry is tackled. It has been shown that the interface location can be stabilized, so the benefits mentioned above are realized. The improvements have been obtained with modifications to conventional furnaces - the incorporation of heat-pipes, changes to gradient zone design and to the control structure of the furnace. It is expected that the simplicity of the resultant furnace would make it easy to use the modified Bridgman-Stockbarger furnace for further analyses of fundamental crystal growth issues, and to incorporate similar modifications into industrial production furnaces (upon scale-up).

The most tantalizing application of the methodology of interface control presented in this work would be to the development of a 'continuous Bridgman'[5] growth technique. A 'continuous Bridgman' technique would remove the batch nature of the growth process, and associated transients in segregation characteristics. This idea is presented in more detail in the concluding chapter.

Photographs of the crystal growth system developed in this work are provided in Figures 1.1 and 1.2.

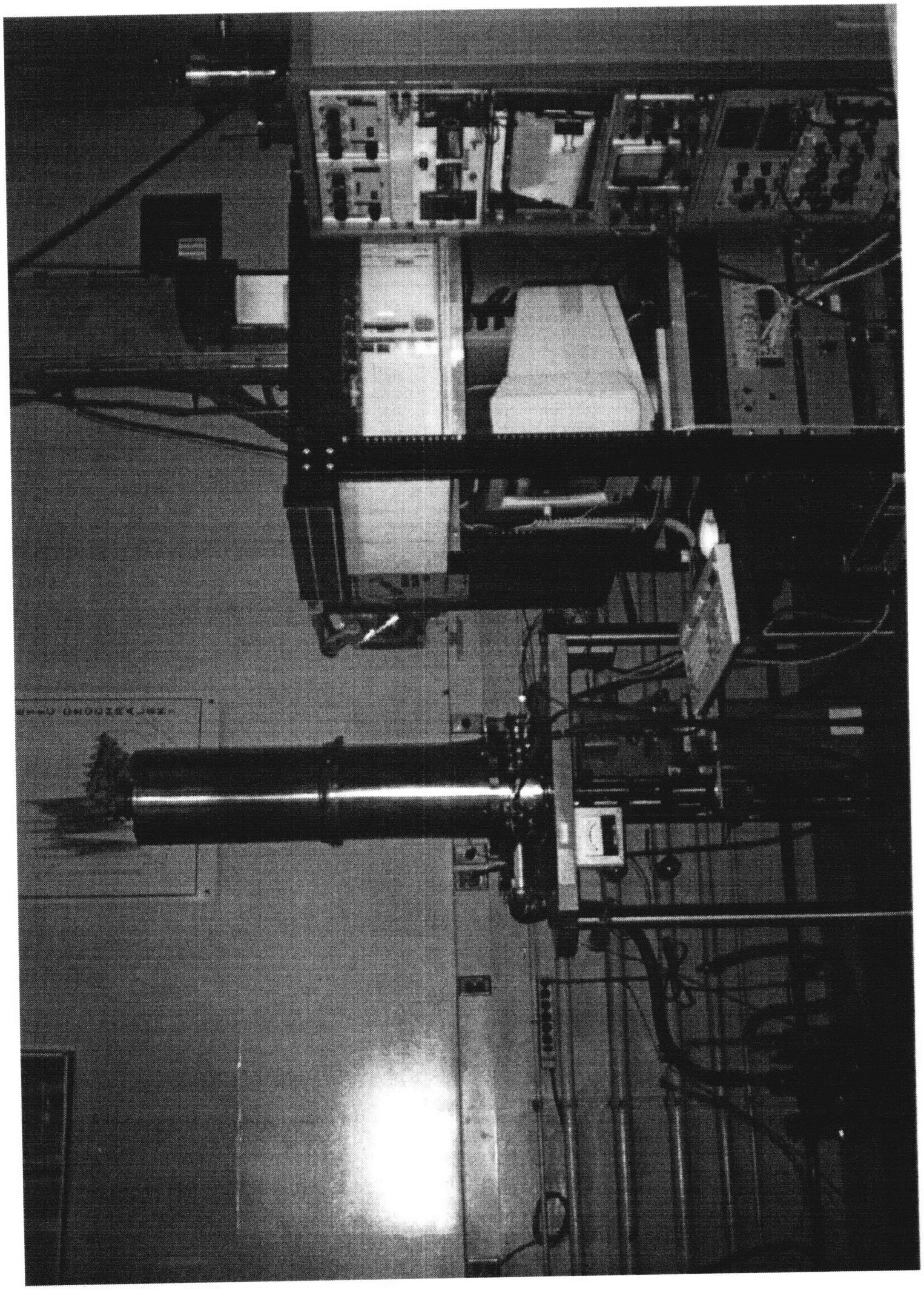

Figure **1.1** : The Bridgman-Stockbarger system.

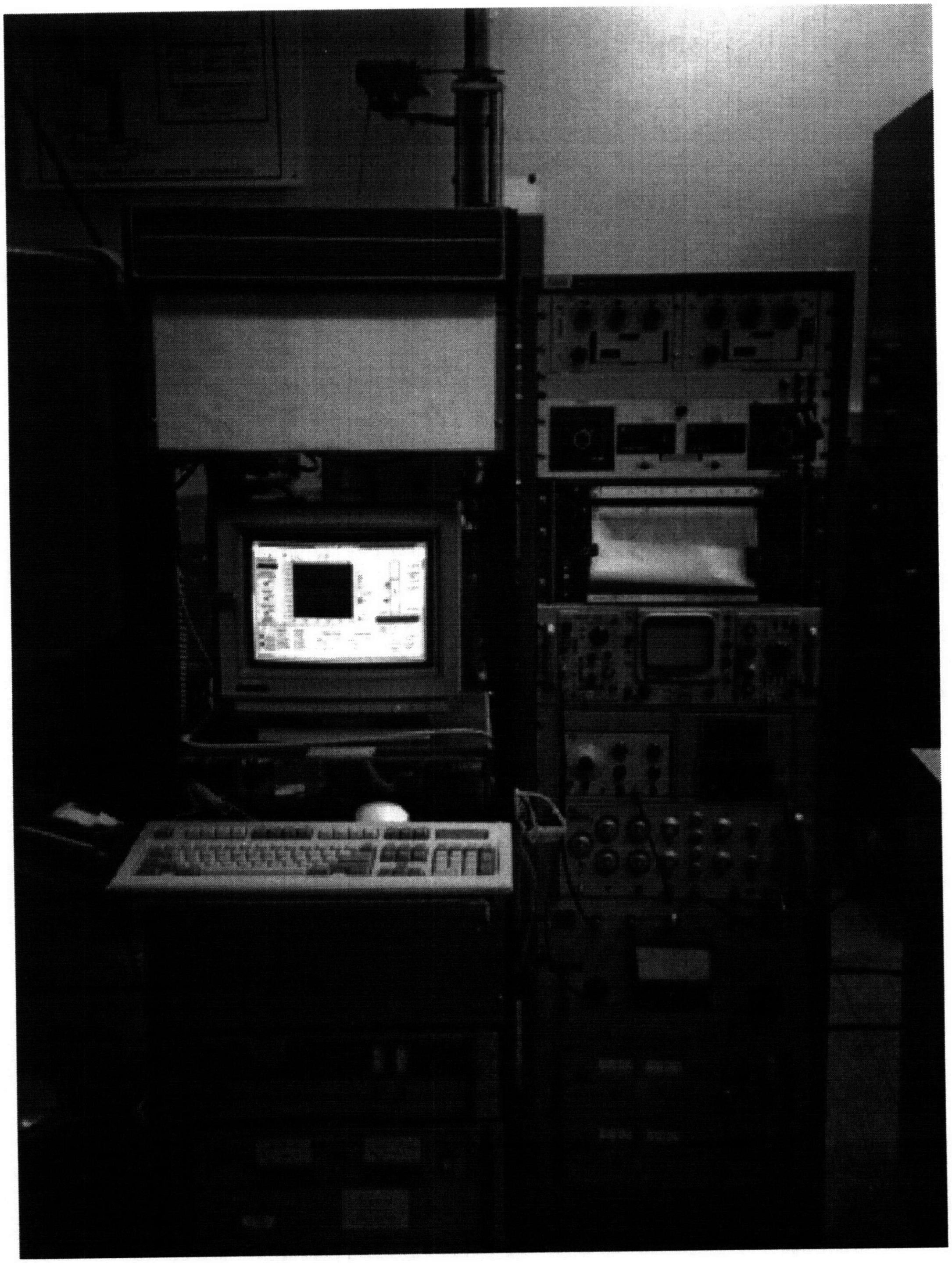

Figure **1.2** : The instrumentation racks.

Chapter 2 Literature Review

> This literature review serves two purposes. The first aim is to provide perspective on the place of vertical Bridgman family of growth techniques - by presenting a broad survey of crystal growth techniques, and their relative advantages and disadvantages. The second aim, intertwined with the first, is to not only include work that directly presages the idea of improving control over interface location, but also to present work that highlights the importance of interface control to material property control.

2.1 The Czochralski technique

In the Czochralski ('Cz') technique, the melt is contained in a crucible, which is held under a controlled ambient. A seed of known orientation is brought in contact with the melt, and then slowly withdrawn to form the crystal. (Figure 2.1)

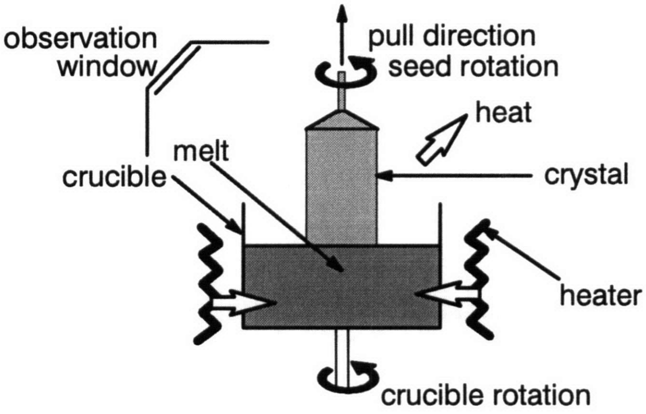

Figure **2.1** : The Czochralski configuration.

The power input to the heater, and the rate of withdrawal of the seed (the 'pull rate') are carefully controlled to grow crystals of desired geometry and good quality. The crystal is rotated to even out the thermal asymmetry. The crucible can also be rotated either in the same direction or opposite to the direction of seed rotation.

The Czochralski technique is the mainstay of commercial production of electronic, optoelectronic and optical materials in single crystal form. It is also a technology that has proven itself to be scalable to growing crystals (of silicon) of 300mm diameter, weighing over 100 kg. It has the advantage of producing a crystal with a free surface, unlike other techniques which confine the growing crystal in an ampoule. The absence of such a crystal-confining ampoule obviates concerns about wetting between the ampoule and the melt, which might result in stresses during cooling of the solidified crystal[7]. The furnace design permits the growing crystal to be easily observed, so that remedial action can be taken if, for instance, the seeding was improper, resulting in polycrystallinity. This feature is useful in maintaining the yield of good crystals, in an industrial context.

The Czochralski technique has several disadvantages too. The melt is unstable with respect to natural convection, since the coldest region in the melt (at the crystal-melt interface) is located at the top. The intensity of natural convection scales as the third power of the critical length dimension of the melt, and so as crystal diameters are increased, convection becomes increasingly an issue. In Czochralski systems, crystal and crucible rotation cause forced convection, while the temperature gradients across the extensive free surface of the melt give rise to surface-tension driven ('Marangoni' convection)[8]. Convection in the melt, especially when system dimensions place it in the turbulent regime, causes large, random, fluctuations in dopant incorporation in the growing crystal[9]. It also contributes to increased erosion of the crucible, and oxygen incorporation in Czochralski growth of silicon. It should be noted that while oxygen at around 25ppm levels is desirable in the starting silicon wafer, and the erosion of the crucible does provide the necessary oxygen, control over the oxygen content has not yet been satisfactorily realized.

Control of the diameter of the growing crystal is also a concern, particularly in compound semiconductors, though several innovative techniques[10] have been implemented to automate the diameter control process. Another complication in the Czochralski technique is that the thermal stresses in the grown crystal are high. In GaAs growth, they are typically high enough to activate slip on the inclined {111} planes, resulting in a characteristic 4-fold symmetry of the dislocation density about the [100] crystal growth direction, with a W-shaped variation across the wafer diameter[11]. Several techniques have been explored to control the dislocation density in GaAs, from doping with indium, to the design of special devices to control the heat-transfer from the crystal surface[12]. When one wishes to model the growth process, difficulties are posed by the complex 3D geometry, and by the complexities of fluid flow and heat transfer of Czochralski crystal growth systems.

The Czochralski technique (like most crystal growth techniques currently in use) suffers from the limitations of being a batch process, dominated by transient effects. The segregation of dopants varies continuously along the length of the crystal, which necessitates sorting of the wafers from a crystal into quality classes, adding to cost and to wastage. Continuous, or semi-continuous Czochralski growth, once it is commercially feasible, will reduce macrosegregation, since a steady-state concentration of the dopant can be built up and maintained.

2.2 Bridgman-type furnace geometries

Crystal growth techniques based on the vertical confined-crystal geometry (referred to as Bridgman geometries) include the Bridgman technique, the Bridgman-Stockbarger technique, Vertical Gradient Freeze and the Electrodynamic Gradient Freeze techniques.

2.2.1 The Bridgman-Stockbarger configuration

The Bridgman furnace (Figure 2.2a) was developed by P.W. Bridgman of Harvard. It has only one zone, from which the ampoule is withdrawn into the ambient. The furnace was used to grow unseeded metal crystals, with grain

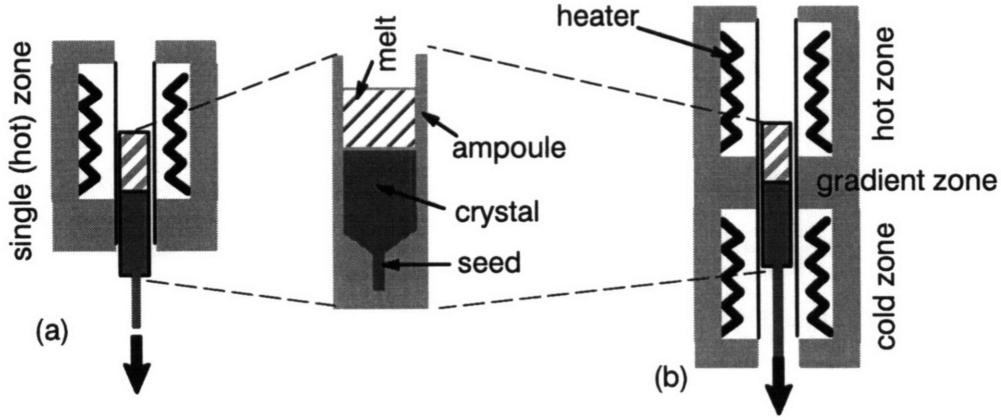

Figure **2.2** : (a) Bridgman furnace, and (b) Bridgman-Stockbarger furnace.

selection being accomplished by a capillary prior to full diameter growth. This design was improved on by Stockbarger of MIT, by adding a second zone held at a lower temperature. The motivation was to reduce the cracking he observed in the growth of LiF and other salts. This had the effect of improving control over the interface location, and giving access, if needed, to higher temperature gradients at the interface. Wilcox and Fu[13] modelled the effects of the addition of an insulating gradient zone between the two actively heated zones. The resulting configuration (Figure 2.2b) decreased the sensitivity of the interface morphology to its position within the furnace. It should be noted that, in the Bridgman-Stockbarger configuration, the furnace can be moved with respect to the stationary growth ampoule.

2.2.2 Gradient freeze technique

The gradient freeze furnace, another member of the family of Bridgman geometries, is similar to a Bridgman-Stockbarger furnace. The difference lies in the way the crystal-melt interface is moved through the charge volume. The Vertical Gradient Freeze furnace (Figure 2.3a) has no moving parts. - the crystal and the furnace are stationary. Growth is accomplished by programmatically ramping down the power into the hot and cold zones, thus sweeping the melting point isotherm of the system in the upward direction. This is being used for growth of a large variety

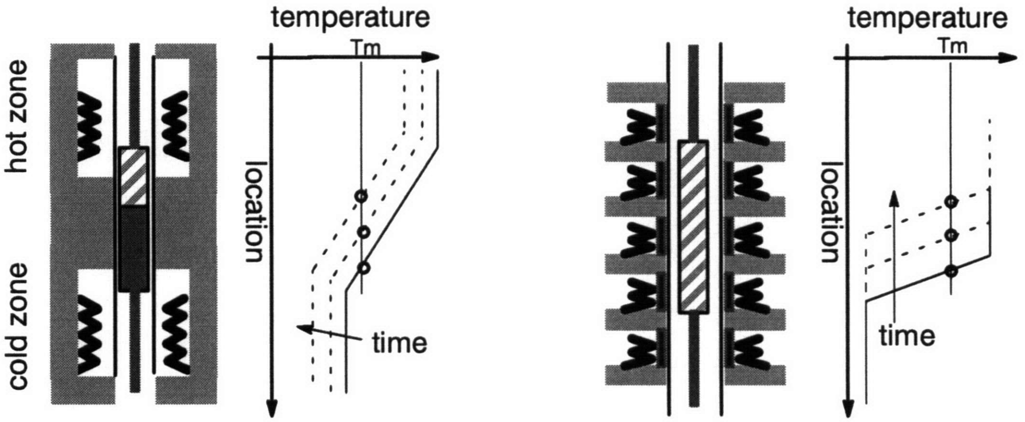

Figure **2.3 :** (a) Vertical Gradient Freeze and (b) Electrodynamic Gradient Freeze.

of semiconductors - Ge[34], GaAs[17], GaP, and InP[18], for instance. The technique is shown to yield boules of lower dislocation density than the Czochralski technique[17].

In the Electrodynamic Gradient Freeze (EGF) furnace, the gradient freeze concept is taken further, by using tens of independently controllable zones (Figure 2.3b gives a schematic). The temperatures of the zones follow a preprogrammed path so as to sweep the melting point isotherm from the seeding position to the end of the growth ampoule. This technique takes advantage of the availability of modern, multi-channel controllers, and confers flexibility in the adjustment of axial gradients over the length of the growth ampoule. In the system used by Momberg *et al*[14], each zone has an independent controller. Each heater is insulated, with the insulation immediately surrounded by an aluminum chill-plate. This design removes coupling between adjacent zones, allowing the use of independent controllers - otherwise a more complicated multiple-input - multiple-output (MIMO) controller based on 'state-space representation' techniques would be needed. It has been suggested[15], however, that the use of such chill-plates might cause the growth rate to be modulated with a periodicity that matches the width of a single zone. This has not been addressed by Momberg *et al*[14]. On the other hand, the interface shape (to the accuracy that can be attained in macrographs of striations) remains constant throughout the growth. A handicap of the EGF technique appears to be the physical complexity, and the attendant maintenance problems associated with a system having 20 or more zones, with that many heaters, coolers and thermocouples and control loops. Maintaining the calibration confidence of all these thermocouples is an additional burden.

The EGF technique has the capability of allowing the interface shape to be chosen, through appropriate design of the axial thermal profile. In the application of the EGF technique to the growth of 50mm diameter gallium doped germanium[16], the authors report the first achievement of a convex solid-liquid interface in the vertical Bridgman growth of 50 mm diameter semiconductors. Such advantages notwithstanding, the EGF technique is not widely used, neither in production nor in research, due to the high maintenance required.

2.3 Advantages of Bridgman geometries

The Bridgman geometry is simple - as a result, the furnace is capable of rapid assembly. Design changes are easier to incorporate, and as such it is an ideal research tool. It is also applicable to a wide variety of solidification temperatures, and pressures.

Another advantage of the vertical Bridgman geometries is that the axial temperature gradient in the melt is such that the coldest (and densest) liquid is at the bottom, near the crystal-melt interface. Hence, the axial temperature gradient does not set off buoyancy-driven natural convection. Convection in vertical Bridgman geometries is driven by the smaller radial gradients, and is weaker than in typical Czochralski systems. The free surface in vertical Bridgman geometries is not very large (particularly if bubble formation on the crucible wall is not an issue). As a result, Marangoni convection is not very important in vertical Bridgman furnaces (on Earth).

The Bridgman geometry is easier to model than the Czochralski process. Furthermore, with the use of heat-pipes as furnace liners in Bridgman geometries, realism of analytical and computer models is easier to attain than for the Czochralski process. Assumptions of isothermality and of azimuthal symmetry are more justifiable, viewfactor calculations for radiative heat-transfer are easier, and geometry specifications are easier, to name a few of the reasons why modeling of advanced Bridgman furnaces is easier. This allows fundamental issues in crystal growth, like radial segregation and interface morphology, to be addressed on a less empirical footing.

In Czochralski systems, radial temperature gradients near the crystal-melt interface are unavoidable, due to the very geometry of the system. They might also be considered useful for diameter control - a higher average radial gradient in the melt, in 'steady state', can be considered to make the crystal diameter less susceptible to undesired high frequency fluctuations. Since diameter control is not an issue in Bridgman geometries, the need to minimize radial gradients can be acted on to the fullest extent. This reduces thermal stresses in the grown crystal, and also reduces interface curvature.

It should be noted that there is a horizontal variant of the Bridgman process. The Horizontal Bridgman technique is commercially important, especially for Si-doped GaAs that can be used as substrate material for laser devices, and II-VI compounds that are used to fashion near- to mid-IR detectors. This technique is very different in its growth characteristics from the vertical Bridgman technique – the interface curvature is high and convection is not weak, for instance. It has lower stresses than Czochralski systems, however, and the free three-phase boundary at the growth interface makes stoichiometry control easier in the growth of compound semiconductors.

2.4 Unresolved issues in Bridgman type crystal growth

As mentioned in Section 2.3, the Bridgman technique is particularly suited to studies aimed at elucidating fundamental problems of crystal growth - the interplay between interface shape and radial dopant segregation, for example. The usefulness of the Bridgman technique arises from its simplicity.

However, there are several outstanding issues[19] that need to be addressed, if the Bridgman technique is to become an even better vehicle for crystal growth analyses, and if it is to gain greater acceptance in the crystal growth industry. Currently, very few companies produce vertical Bridgman material for the marketplace - AXT, Inc. is one, producing undoped GaAs (50mm diameter).

The industry has focused its attention on reducing the incidence of polycrystallinity - since current furnace designs of the vertical Bridgman process do not allow the growing crystal to be monitored. This is a major concern since the continued growth of a polycrystal represents wasted resources. The industry has largely ignored interface location and morphology control issues, though they are of fundamental importance to the crystal quality. Thermal stresses during growth and cool-down need to be better understood and controlled. Dopant segregation, crucible-melt interaction, and stoichiometry control are some of the other concerns needing attention. Some of the afore-mentioned issues will be discussed in the following sections.

2.4.1 Thermal fields in the charge

The Bridgman process is a batch process, as has been demonstrated by Wang[20]. In a conventional Bridgman furnace, the growth rate does not reach steady-state conditions at any point during growth (Figure 2.4). The magnitude and nature of the transients have been shown to arise from various end effects, which change the thermal field that the crystal-melt interface is subject to, during growth. The author uses the term 'configurational thermal transient' to refer to the growth transient that stems from the thermal coupling changes caused by specifics of furnace construction - the location of the control point, and the nature of cooling used on the crucible shaft. Such 'configurational thermal transients' in growth rate need to be suppressed, since they do not permit control of the growth rate. In addition, since the thermal fields established by the furnace in the charge are not controlled with any measure of certainty, the initial seeding location cannot be pre-selected except in a highly heuristic manner. This implies that the growth ampoule has to be designed with a long enough seed, so that there is enough leeway to avoid complete loss of seeding due to unanticipated meltback.

Numerical simulations by Lan *et al*[21] of transient effects during growth of GaAs also show that the growth rate in vertical Bridgman furnaces does not reach steady state. They note that the interface deflection might level off - which only indicates that the furnace design makes interface shape insensitive to its location in the furnace.

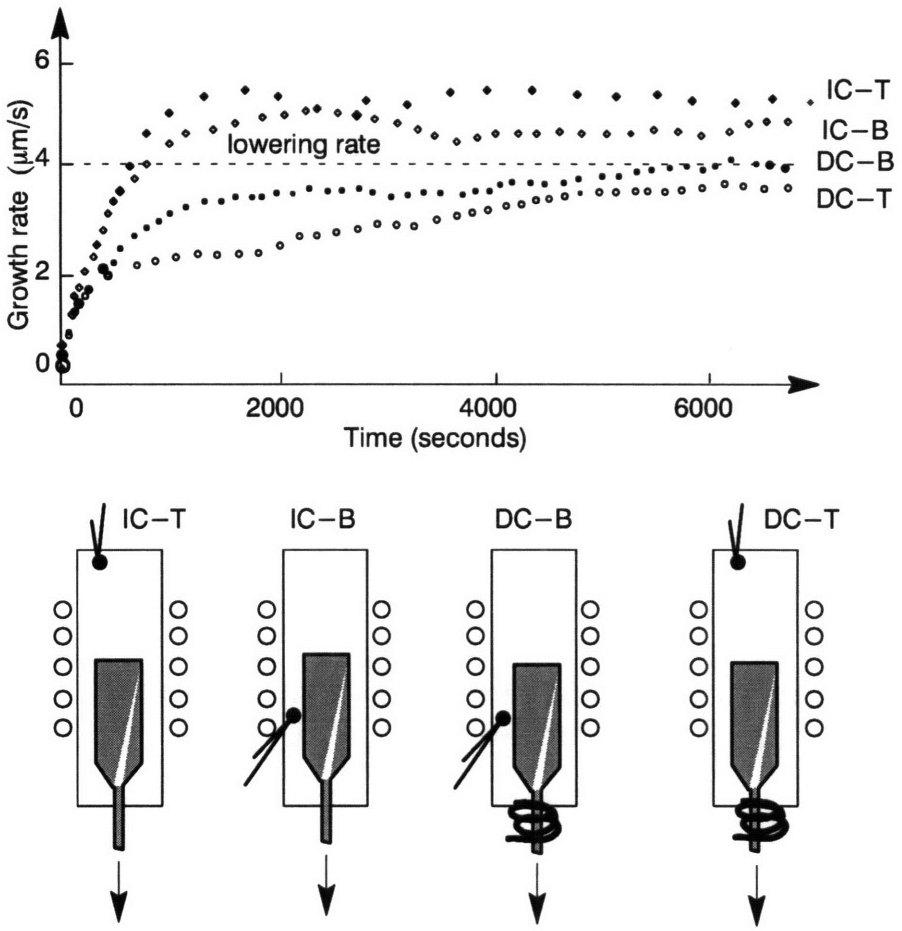

Figure **2.4** : Extended configurational transients in growth rate in a conventional Bridgman furnace, with different control points and cooling mechanisms[20].

Barber *et al*[22] have used 'radio-imaging' of the growth interface in an x-ray transparent vertical Bridgman furnace to measure growth interface curvature and growth rates in real-time. The applied translation rate was about 1 cm/hr, but the measured growth rate of the crystal varied from1.3 cm/hr to over 1.6 cm/hr over a 4 cm length of grown crystal. At no point were the actual growth rate and the translation rate identical. When an unseeded configuration was used, the divergence between the growth rate and the translation rate, as seen by these authors was even stronger. The divergence between the growth rate and the translation rate might arise from the ampoule not being long enough for 'infinite length' criteria to be satisfied (details of the furnace hardware are not provided, and so this is speculative). The 'infinite length criterion' gives the minimum length of charge that must extend into the the hot and the cold zones to avoid transient thermal effects due to changing thermal coupling lengths. The minimum charge length needed for the 'infinite length criterion' to be satisfied can be estimated if the heat transfer characteristics of the furnace are known ([23],[24]).

Batur *et al*[25] proposed the use of optical imaging techniques for the growth of lead bromide in a transparent multi-zone vertical Bridgman type furnace. The temperature controller used is an *adaptive* PID controller, which uses a least squares algorithm for system parameter identification, Ziegler-Nichols tuning, and pole placement techniques, to get the poles of the system into user-specified locations within the unit circle in the Z-plane. A MIMO (multiple-input, multiple-output) controller is used, with the inter-zone interactions lumped into a disturbance term. The open-loop responses are shown to justify the assumption of a first-order system. The growth rates used are very low, ~ 2 cm/day. The authors also propose the use of real-time interface location measurement - using the furnace imaging data, processed through histogram-based segmentation, median filtering, and finally, edge detection to extract the interface location from the image. This information is to be fed into a multivariate controller which adjusts the translation rate and the heater powers in each of the eight zones. No further work could be found.

Shaped Melt Lowering (SML) is a novel technique[26] that was used to grow thin (1 mm) plates of GaSb. The aim of this work was not to demonstrate interface control, but it is interesting to note that, a crucible is used only to hold the melt. The grown crystal is withdrawn from the ampoule through a capillary slit that defines the crystal cross-section (Figure 2.5). It was noticed that a meniscus is maintained, with liquid beneath the slit, supported by the growing crystal. This technique is intriguing in that, when coupled with better interface control and better

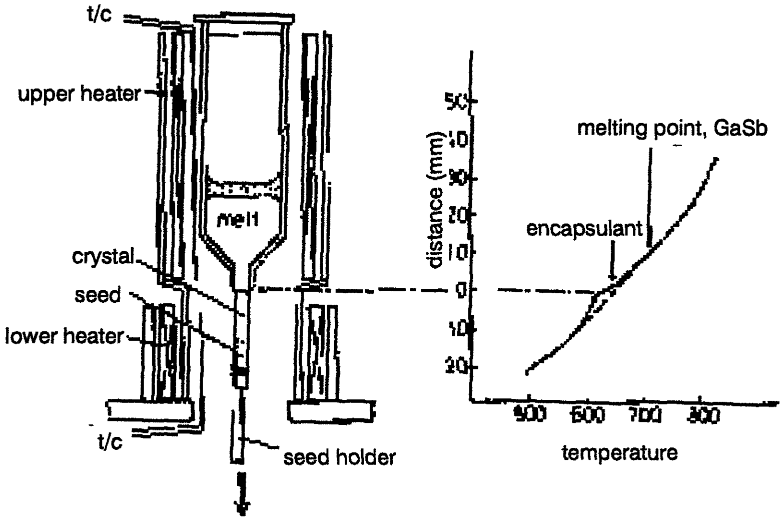

Figure 2.5 : Shaped Melt Lowering (after [26])

furnace design, it might conceivably lead to a continuous-Bridgman crystal growth process.

Wang[27], in her thesis work on the incorporation of heat-pipes in vertical Bridgman growth was able to demonstrate interface location stabilization. The growth rate and the translation rate were identical, after the initial transient (Figure 2.6) - implying that the interface remained stationary with respect to the furnace. It was necessary, however, to ensure that the 'inifinite length criterion' was satisfied.

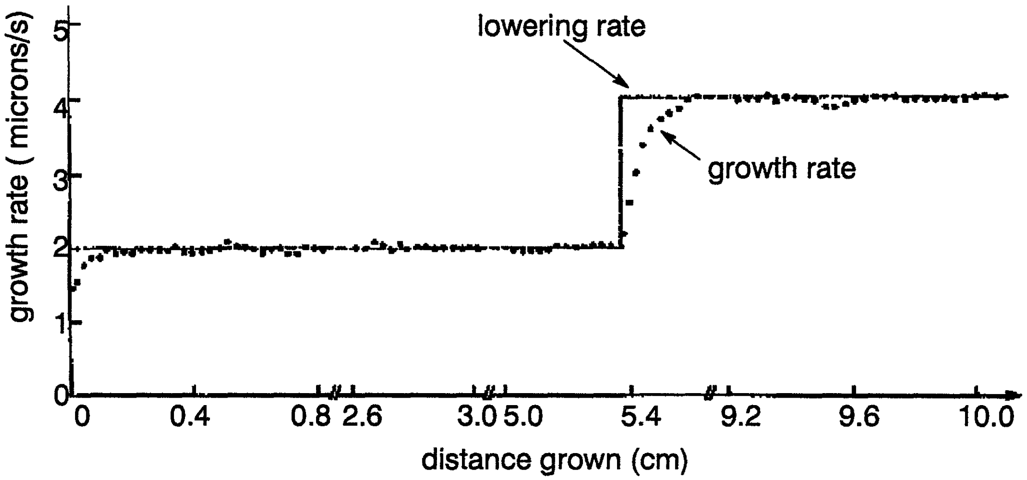

Figure 2.6 : Interface stabilization in a heat-pipe based Bridgman-Stockbarger furnace (after Wang[27]).

For the furnace and ampoule configuration used, the minimum extension length out of the gradient zone into the hot zone was determined to be 44 mm.

A critical feature that should be sought after in Bridgman furnace design is that, the thermal boundary conditions around the growing crystal and the melt can be quantified, controlled, and generated reproducibly. Such reproducibility, quantifiability, and controllability of the boundary conditions are of particular importance when simultaneous modeling efforts are undertaken to fine-tune the process parameters.

2.4.2 Stoichiometry control

In Vertical Bridgman growth of compounds - whether they be semiconductors or oxides - control of stoichiometry is an issue[28]. The question arises because the crystal-melt interface is usually far removed from the gas-melt interface, separated by a volume of melt, whose thickness changes during growth. The gas-melt interface (located at the top of the growth ampoule) is also at a different temperature than the crystal-melt interface, so that control of stoichiometry at the available interface (the gas-melt interface) does not necessarily imply that the same stoichiometry is obtained at the growth interface.

2.4.3 Considerations of crucible-melt interactions

One of the features inherent to the Bridgman geometry is that the grown crystal is confined within a crucible. The choice of the crucible should be based on the following considerations: (i) physical and chemical interactions between the melt and the crucible material, (ii) heat transfer characteristics of the crucible, and (iii) mechanical properties at the service temperature.

The dissolution of silicon into a GaAs melt when it is contained in a quartz ampoule is an example of chemical interaction. The interaction is not entirely detrimental - in the case of GaAs wafers used in laser applications, the n-type doping obtained by growth in a quartz crucible (due to Si) is acceptable. In other instances, such chemical interaction would be intolerable. If the physical properties of the crucible surface are such that it is wetted by the melt, there is a possibility that the grown crystal will be ‘keyed’ into the irregularities of the crucible wall, and so appear to adhere to the wall. This ‘sticking’ prevents the crystal from contracting freely as it cools, resulting in stresses that generate dislocations[7] or even cracks.

Another problem that the confinement causes has been termed the ‘interface effect’[29]. At the interface, there is a discontinuity in the thermal conductivity in the charge (between the melt and the solid), causing a discontinuity in the slopes of the temperature gradients at the interface. The temperature profile in the crucible, on the other hand, does not show such a discontinuity since its conductivity remains constant. This causes localized heat transfer between the crucible and the charge, typically resulting in a concave interface (a concave interface in a vertical Bridgman system is defined as one that is higher at its edge than at other points on its surface). The authors concluded that reversal of the concavity, if it is so desired, can be achieved through techniques that need *a priori* knowledge of the interface location. Ideally, the conductivity of the crucible material in the radial direction, should be very high, while the conductivity along the length of the crucible should be low - this allows high coupling between the furnace wall and the charge, without smearing impressed thermal gradients, or contributing to the ‘interface effect’.

Currently, the choice of the crucible is dictated by expediency. Some new approaches have recently been explored. The vertical gradient freeze growth, by Momberg[30], of InP encapsulated in B_2O_3 within a pyrolytic Boron Nitride (PBN) crucible is an example. The B_2O_3 completely encapsulates the InP, and wets the PBN. But, since the PBN crucible has a laminar structure, a sacrificial layer of PBN is pulled away during cooling, preventing stress from building up in the crystal. Other ‘soft-mold’ approaches which do not generate stresses need to be developed. An example is the use of calcium chloride for the ‘liquid encapsulated Bridgman’ growth of silicon for solar cell applications[31].

Another direction that has not been explored at all is the use of composite crucibles. For example, a thin film sandwich of Pt/Cr could be evaporated (or put down by electroless deposition) onto a quartz ampoule to contain the highly corrosive Bismuth Silicon Oxide melts in Bridgman geometries. A composite crucible has the advantage that its components can be selected for specific, desirable features. In the above example, the Pt thin film confines the melt, with a minimum of chemical interaction, the Cr underlayer serves for adhesion to the quartz. The Quartz ampoule has low thermal conductivity, but will allow radiative heat transfer between the charge and the furnace. Use of a thin film of Pt also reduces cost.

2.4.4 Interface morphology control

Control of the growth interface morphology has been a long-standing concern[32] in Vertical Bridgman-type geometries. The importance of the morphology is many-fold. A highly curved interface in dilute systems is a good diagnostic - it is an indicator of high radial temperature gradients near the growth interface. This could cause thermal stresses that result in a high dislocation density. In non-dilute alloy crystal growth, the curvature of the interface is additionally affected by compositional differences in the melt from the center to the periphery[33]. A convex interface (see Figure 2.7a) reduce the chance that a twinned region or a grain nucleating near the periphery propagates through the entire cross-section of the crystal.

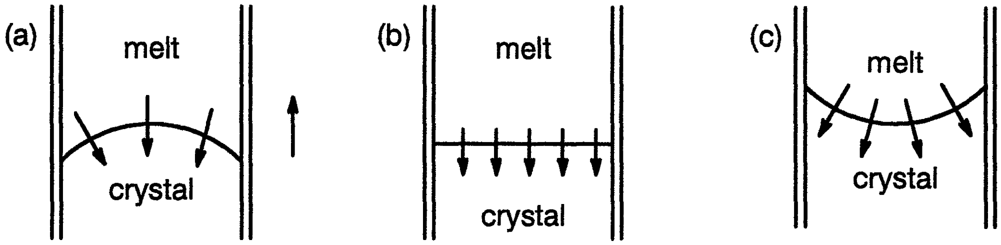

Figure **2.7** : Heat flows in (a) convex, (b) planar and (c) concave interfaces in vertical Bridgman geometries (after [32]).

The shape of the interface needs to be considered along with nature of the solute boundary layer to arrive at the dopant incorporation profile. If dopant uniformity in the radial direction is desired, a planar interface is not necessarily ideal in the presence of convection. For uniform incorporation of dopants at all points of the interface, it is necessary that the boundary layer be uniformly thick at all points of the interface (assuming melt homogenization). In the presence of a single convective roll (Figure 2.8), a slightly concave interface is indeed desirable, to keep the boundary layer thickness (δ) uniform. Convection in Bridgman geometries is lower than in Czochralski systems, and as a result the boundary layer thicknesses are larger in Bridgman growth. As a result, segregation effects become more sensitive to small convective instabilities, and larger radial segregation (at the macro-scale) is seen in Bridgman material than in Czochralski material. Convection needs to be suppressed if one is to get diffusion-limited transport in semiconductor melts. Techniques used achieve diffusion-limited conditions include growth in space, in micro-gravity conditions[34]; and high magnetic fields under terrestrial conditions[35]. When convection is suppressed, particular care has to be taken to ensure bulk melt homogenization prior to growth.

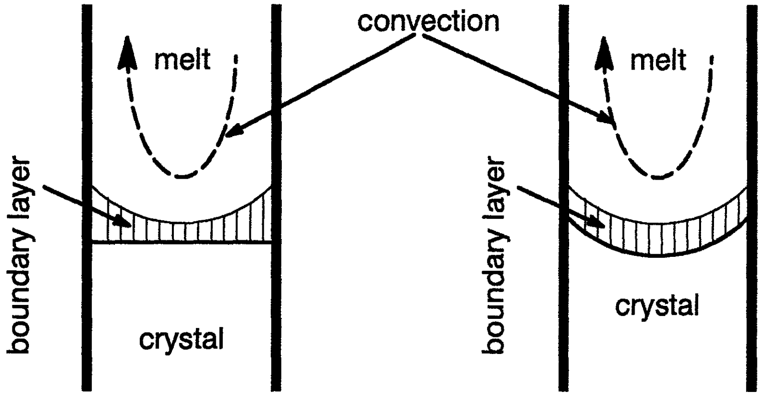

(a) Planar interface but solute boundary layer thickness is non uniform.

(b) Concave interface with uniform solute boundary layer thickness

Figure 2.8 : Interface shape - boundary layer interaction

Experimental work on studying interface shape has taken several routes. Decantation is commonly used. Feigelson and Route[36] measured the interface shape during growth of $CdGeAs_2$ in a single-zone gradient freeze furnace and in a Bridgman-Stockbarger furnace by decanting the melt to halt growth. In the gradient freeze furnace, the interface was severely concave, possibly causing the observed polycrystallinity, which the authors were attempting to avoid. They were able to show that, by tailoring the axial temperature gradients in the gradient zone of the Bridgman-Stockbarger furnace, the planarity of the interface could be improved, and single-crystal boules grown. Dutta *et al*[37] used quenching (by periodic, and sharp, dips in the furnace control temperature) to demarcate the interface during the growth of GaSb in a single zone Bridgman furnace. Growth rate deviations of 25% from the ampoule translation rate were measured, with impressed gradients of 37 °C/cm.

Wang[27] used current pulses sent across the crystal-melt to demarcate the interface during Bridgman-Stockbarger growth of Ga doped Ge. She found that the interface shape did become more concave (by 18%, using her metric) as the growth rate was increased from 2 μm/s to 4 μm/s. This was attributed to latent heat and Peclet number effects. The Peclet number is the ratio of heat transported by motion of the charge to the heat transported by convection. Wang was also unable to reverse the concavity of the interface, irrespective of its location within the gradient zone. Curiously, the 'diabatic gradient zone' (which had increased axial and radial conductivity due to the presence of concentric rings of inconel) did not result in any change in the interface curvature, when compared to the results from the use of an 'adiabatic gradient zone' (which was fabricated entirely of insulating material).

Möller *et al*[38] also used current pulses for demarcation. In contrast to Wang[27], they determined that different growth rates had no significant effect on interface shape, in their furnace. They were unable to achieve a planar interface, but did show that, the concavity could be reduced by moving the interface up in the gradient zone.

Koai *et al*[39] used a numerical finite element model to study the feasibility of modifying interface shapes using furnace modifications that would be operative at different stages of growth. By incorporating a 'booster' heater around the gradient zone, and by using a highly anisotropic gradient zone material (with *high radial conductivity*), the shape of the interface during the constant diameter growth can be modulated at will. The reason for the unusual choice of a high radial conductivity in the gradient zone 'insulation' is to allow the booster heater to influence the thermal profile at the ampoule wall. In other words, it is an 'active' gradient zone. Experimental verification was said to be in progress.

2.4.5 Dopant segregation considerations

As discussed in the previous section, the importance of the interface shape arises from its relevance to radial segregation of the dopant. Coriell and Serkerka[40] developed analytic expressions for the radial segregation behavior during crystal growth with a slightly curved solid-liquid interface, under diffusion-limited conditions (no convective transport in the melt). They showed that, in the limiting case of a very thick boundary layer, the radial segregation is the product of the segregation coefficient, the maximum deviation from planarity of the interface, and the concentration gradient at the interface (as applicable to a planar interface). A concave interface results in a radial segregation profile that has a higher concentration of dopant at the center of the crystal. The results were later extended[41], numerically, to the case of an interface with large curvature.

Möller *et al*[38] conducted an analysis of the dopant segregation of the Gallium doped Germanium crystals grown in a vacuum 3-zone furnace. It was found that the radial and axial segregation behavior was indicative of convective-diffusive transport in the melt. They used Favier's formalism[42], to show that the parameter $\Delta = 1$. Δ is defined as $v\delta/D_l$, where v is the growth rate, δ

is considered the solute boundary layer thickness and D_l is the diffusivity of the dopant in the melt, and a value ~1 implies that convective and diffusive influences are equally important.

Adornato and Brown[44] found that, in a typical Bridgman-Stockbarger furnace, two toroidal convective cells would be present in a Bridgman-Stockbarger furnace. The upper cell, extending into the hot zone, is driven by the radial temperature gradients present at the junction between the hot zone and the gradient zone. The lower, counter-rotating, less intense convective cell is driven by the radial gradients caused by the differences between the thermal conductivities of the melt, the crystal and the ampoule (Figure 2.9). They were able to obtain very good agreement between their simulation and the experimental data of Wang[27] - with respect to interface shapes, interface location, radial and axial segregation

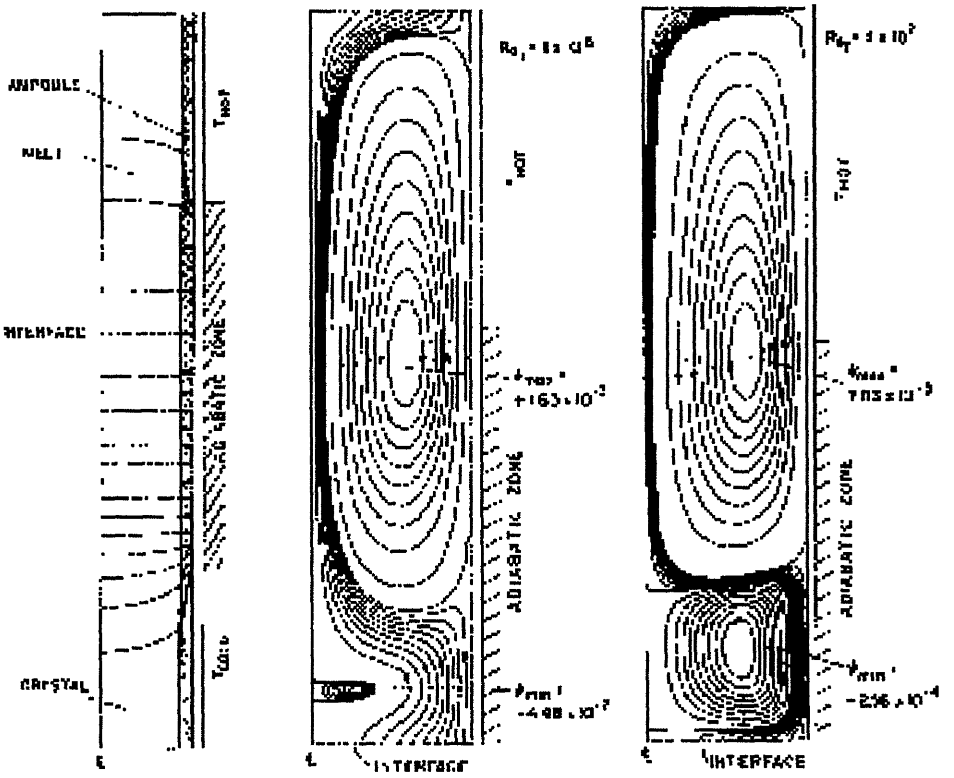

Figure 2.9 : Melt convection cells in a Bridgman-Stockbarger furnace[44].

profiles. Their simulations also showed that the furnace used by Rouzaud *et al* [43], had only one convective cell extending through the length of the melt, due to the fact that their furnace impressed a constant axial gradient on the ampoule.

Kim and Brown[45] conducted simulations of the transient convective and segregation effects for growth of GaAs in a gradient freeze furnace. The shape of the interface was not influenced by convection, but rather by conduction. They concluded also that the liberation of latent heat was responsible for the large interface deflection and the resultant large radial segregation observed in this system. This was attributed to an aspect of the furnace design that reduced the efficacy of heat removal from the growth interface, and to the high (7.6 μm/s) growth rates used in the simulation.

In general, the interface shape during growth of semiconductors (Ge or GaAs, say) is dictated by conductive heat transfer within the charge. Convective effects do not determine interface shape - due to their low Prandtl numbers (the ratio of the kinematic viscosity, ν, to the thermal diffusivity of the melt, $\alpha_{m,}$ is much smaller than 1). The interface shape then interacts with the flow fields in the melt to give rise to radial segregation effects of varying magnitudes.

2.5 Heat-pipes and their use in crystal growth furnaces

A prime modification introduced into vertical Bridgman furnace design by Wang[27], and the study of which is continued in this work, is the use of heat-pipes in the hot and cold zones.

A heat-pipe is a high thermal conductivity device. It is essentially a pressure vessel, filled with a condensible vapor (Figure 2.10). The 'working fluid' could be water (for low temperature applications), or sodium (for operation between ~500°C and 1100°C). Water-based heat-pipes use a variety of materials including glass and stainless steel for the vessel construction. Sodium-based heat-pipes are better contained in Inconel 600 because of its high creep resistance at 1100°C. In the heat-pipe, the heat transfer fluid evaporates under film-boiling conditions in the

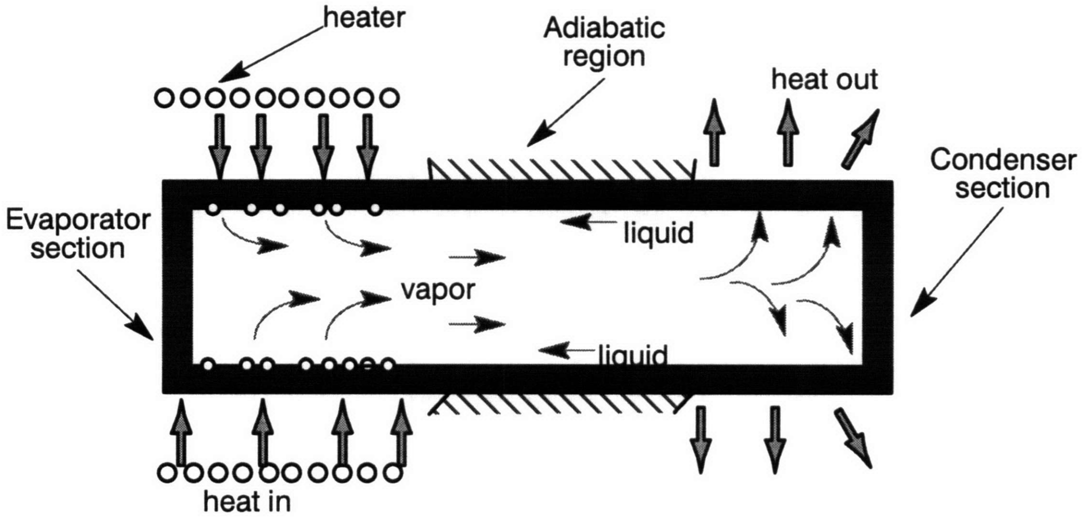

Figure **2.10 :** Schematic of the operation of a heat-pipe, used as a high thermal conductivity device.

evaporator section. The vapor moves to the condensor section, where it releases its latent heat. The heat-transfer coefficient of film-boiling processes is large. Large amounts of heat can be transferred from the evaporator to the condensor by choosing a working fluid with a sizable latent heat. Since the pressure throughout the enclosed volume is almost constant, the equilibrium temperature for the liquid-vapor phase transition is almost the same throughout the heat-pipe. This means that the temperature difference between the condensor and the evaporator is very small. Since high heat fluxes can be transported over long distances (of adiabatic nature), with negligible temperature gradients, the heat-pipe justifies being called a high conductivity device.

The condensed liquid has to be returned to the evaporator section, for the process to continue. If the heat-pipe is used vertically, with the condensor above the evaporator, gravity will accomplish the return. Usually, however, capillary forces are used to assist the return of fluid to the evaporator, and to ensure that all regions of the evaporator are equally wetted by the fluid. Grooves on the inner wall, or a mesh structure can be used (Figure 2.11).

Figure **2.11** :
Cross-section of a (failed) inconel heat-pipe from Dynatherm Inc., showing the annular space where the sodium vapor is contained, and the wick which helps return the liquid to the evaporator region. Heat is applied on the outer wall. (This design, and the application of heat-pipes as isothermal furnace liners, is covered by a patent of Dynatherm, Inc.)

The heatpipe can be used in a manner that exploits the near-isothermality of the enclosed volume. In such applications, it is important to keep in mind that the heat-pipe has limits on the amount of heat it can transfer while still retaining its isothermal character. The limits to its heat-transfer abilities[46] arise from (i) sonic limitation at lower temperatures, when flow gets choked, (ii) entrainment, where the gas prevents the smooth flow of the liquid back to the evaporator, (iii) insufficient wicking, and (iv) boiling - where bubble formation in the evaporator decreases the maximum radial heat flux into the heatpipe. The above constraints mean that a heat-pipe, when used to maintain isothermality of the furnace cavity, must be used with proper care taken to minimize unnecessary heat losses. Bienert[47] shows that the deviation from isothermality over a 20 cm length, degrades from 2 °C when the heat-pipe is enclosed in two radiation shields to over 16 °C when it surrounded by just a quartz tube. He also points out that the isothermality exists only on the inner surface of the heat-pipe, and that different conductive heat fluxes across the heat-pipe wall at different portions of the heat-pipe (due to differences in insulation) will result in loss of isothermality.

The feasibility of the use of heat-pipes to Czochralski crystal growth furnaces, and the improvement in growth rate control realized by such a modification was demonstrated by Martin *et al*[48]. The use of heat-pipes in vertical Bridgman furnaces[27] results in furnace profiles that can be better modeled, and can be used to eliminate configurational transient effects in crystal growth rate, as was discussed earlier.

2.6 Summary

In this chapter, a survey of crystal growth techniques that fall within the family of vertical Bridgman geometries was presented. The issues that remain unresolved in crystal growth science and technology were reviewed. Much work remains to be done in the realm of interface morphology control, since this, along with the melt convection influences the radial segregation behavior directly. The development of a continuous-Bridgman process needs interface location control. A continuous Bridgman technique would eliminate the axial segregation and nonuniformity caused by the batch nature of the Bridgman technique currently used.

Chapter 3 Objectives and structure of the thesis

3.1 Motivation

Experiments by Wang[27] showed that a heat-pipe based vertical Bridgman furnace could stabilize the interface location, so long as care was taken to ensure that the charge was long enough to satisfy the 'infinite length criteria'. Such a configuration would maintain constant coupling with the two zones in a Bridgman-Stockbarger furnace, except for initial and final transients. However, it would be desirable to design a furnace configuration where such limits (*ie,* the use of a long charge) were not placed on the ampoule design.

Knowledge of the interface location during the crystal growth of semiconductors in the Bridgman configuration could confer several benefits - from a better understanding of segregation effects, to better engineering of the crystal growth process itself. The benefits gained from interface location control have been discussed in the preceding chapters. The importance of interface location control stems partly from the fact that the morphology of the crystal-melt interface is dictated in part by the location of the interface within the furnace. The interface morphology is critical to the properties of the grown crystal in many ways, which have been presented in the preceding chapter.

3.2 Objectives of thesis

The main thrust of this thesis, therefore, is the stabilization of the interface location and morphology in vertical Bridgman geometries, in order to achieve radial segregation control in the semiconductor matrix. The process developed was to be reproducible, and capable of optimization through modeling studies. The technology should be simple, so that incorporation into production equipment would not be difficult.

3.3 Stages of thesis work

Dummy charges were extensively used to mimic the presence of a growth ampoule, and the thermal behavior of the furnace studied. The usefulness of a dummy charge stems from the following considerations : (i) It is a cheaper and faster way to explore the behavior of the furnace than through crystal growth runs. (ii) Attempts at measurement of the thermal field within the charge would perturb the growth process being studied, and (iii) The thermal properties of the model material are better known. As a result, the correlation between computer simulations and experimental results is stronger. On the other hand, a dummy charge prevents the effects of latent heat from being modelled, nor does it allow representation of the difference in thermal conductivity between the solid and the liquid.

In experiments using a model charge, the deficiency caused by neglect of the latent heat can be found by comparing the heat flux due to conduction (KdT/dx, where K is the thermal conductivity, and dT/dx is the temperature gradient) and comparing it to the heat generated at the interface by the latent heat of fusion (H_f), due to growth at a velocity v. The ratio of these two heat fluxes is given more conveniently by the ratio of two dimensionless numbers : ($C_p\Delta T/H_f$), and the Peclet number (Pe) :

$$\frac{K(dT/dx)}{v\varrho H_f} \approx \frac{K\Delta T}{Lv\varrho H_f} = \frac{\alpha}{vL}\frac{C_p\Delta T}{H_f} = (\frac{C_p\Delta T}{H_f})/Pe$$

If this ratio $\gg 1$, then effects of latent heat are not important. For germanium, the latent heat of fusion is 4.6×10^5 J/kg[49], the thermal conductivity (of liquid Ge) is 39 W/mK, and its density is 5.48×10^3 kg/m^3; with a solidification rate of 10 μm/s, and a typical gradient of 3500 K/m, the ratio is 5.4 . (Put differently, the axial heat flow due to conduction is 135 kW/m^2, and the rate of evolution of latent heat is about 25 kW/m^2. That is, under the conditions used, the effects of latent heat contribute to about 20% of the total heat flow in the system). Hence the latent heat contribution is not negligible, but neither does the value seriously undercut the usefulness of model charges in studying the thermal behavior of the furnace.

The progress of the thesis work can be divided into three phases:

- Gradient freeze characterization phase : the thermal behavior of the furnace in the 'gradient freeze mode of operation' was studied using a model charge. The control structure of the furnace after the modification, was such that its operation was similar to a Vertical Gradient Freeze furnace, hence the name 'gradient freeze mode of operation'. The work done here is reported in Chapter 4.
- Bridgman characterization phase : the thermal behavior of the modified furnace in the'Bridgman mode of operation' was investigated, again with a model charge, of hot-pressed boron nitride. Chapter 5 describes the hardware and software modifications made for this phase, and concludes by reporting the results of thermal characterization of the modified furnace.
- Ga:Ge growth phase : the modified furnace was applied to the growth of gallium-doped germanium, using current pulses for interface demarcation, which allowed measurement of crystal growth rates on the micro-scale, and accurate measurements of the crystal-melt interface shape during growth. Spreading resistance analyses were also carried out, to measure the dopant distribution in the grown crystal, in the axial and radial directions. The crystal growth runs are discussed in Chapter 6.

Chapter 7 presents the conclusions arrived at during the course of this work, while the concluding chapter dwells on some areas that can be explored further in the future.

Chapter 4 Thermal characteristics of the furnace in the gradient freeze mode

> In this chapter, the thermal characterization of the furnace in the Gradient Freeze mode of operation is described. An introduction to this mode of operation is first provided, and then, the hardware and software features of this version of the furnace are documented. Control issues that needed to be addressed in implementing this concept are discussed. The results showing the feasibility of controlling a vertical Bridgman furnace operated in the gradient freeze mode are presented.

In a conventional Gradient Freeze furnace, crystal growth is accomplished by ramping down the temperature of the hot zone and the cold zone of the furnace (Figure 4.1). This causes the melting point isotherm to move upward through the stationary crystal growth ampoule. If the temperatures of the zones are ramped down linearly though, the rate of motion of the melting point isotherm is not constant. Efforts can be expended to (heuristically) choose a ramp-down program

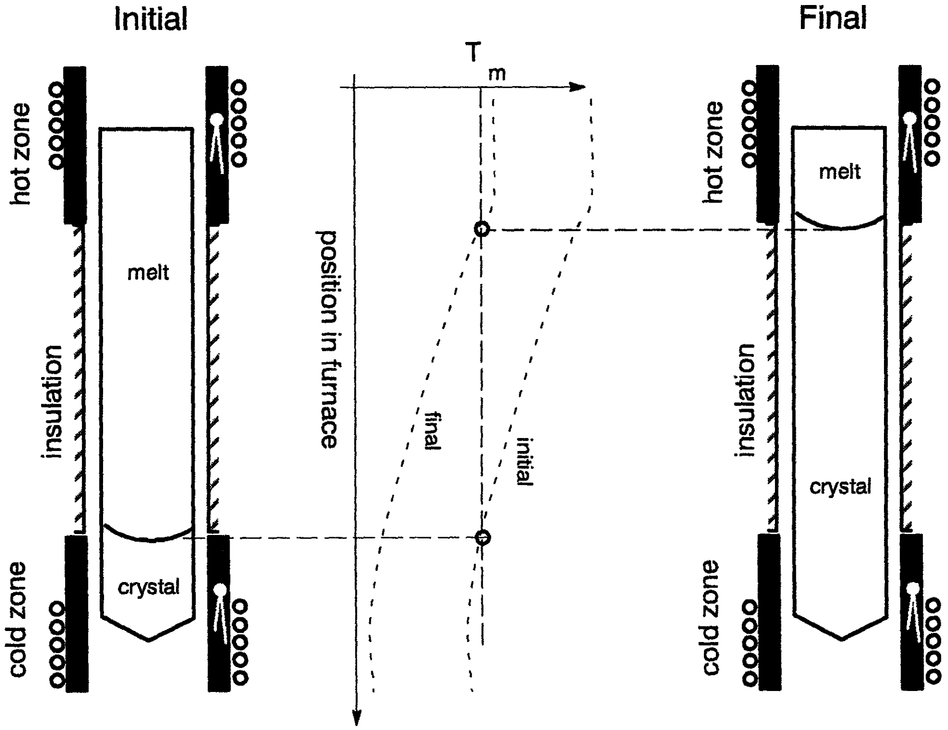

Figure 4.1 : Vertical Gradient Freeze (VGF) Furnace

that changes the setpoints of the hot and cold zone in such a fashion as to move the isotherm at a constant rate, to accomplish growth at a constant rate. Usual practice in industry, however, is to ignore the variation in growth rate.

The 'gradient freeze mode' of operation of the modified furnace is illustrated in Figure 4.2. Two thermocouples functioning as sensors for control for the hot and cold zones are positioned with a fixed (known) vertical spacing in the gradient region at a location where the initial seed-melt interface is to be established. The hot and cold zones are powered so that the temperatures (T_m+x) and (T_m−x) are maintained at the locations of the upper and lower thermocouples respectively. This temperature selection places the crystal-melt interface at the desired postion *and* establishes, at the confining crucible wall, fixed vertical thermal gradient conditions.

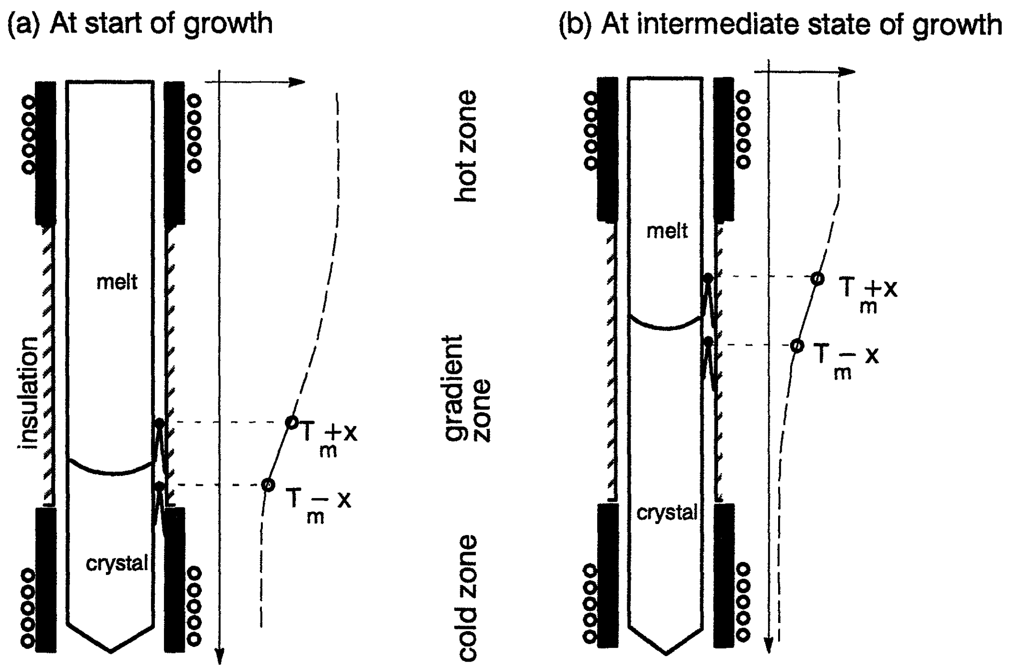
(a) At start of growth

(b) At intermediate state of growth

Figure 4.2 : The 'gradient freeze mode' of operation of the modified furnace.

Crystal growth is initiated and sustained by moving the control thermocouples at the desired growth rate in the upward direction. In this mode of operation, the temperatures in the hot and cold zones self-adjust continuously to provide the set temperature gradient configuration about the moving growth interface. Changes in thermal coupling between the moving charge and the furnace zones are automatically compensated by commensurate changes in the power inputs to the two zones.

4.1 Furnace instrumentation and software features

Temperature and motor control software was implemented in C, on a MassComp 5500 computer, with Real Time Unix extensions (which are particularly useful for fast process control applications). The MassComp had a bank of 12-bit digital-to-analog converters, which were used to control two 2.4 kW power supplies from Electronic Measurements, Inc (Model SCR-80-28-0V), and the translation motor controller (Servo Controller Model C0501, EG&G Torque Systems, now Cleveland Motor Controls). The thermocouple voltages were digitized to 16-bit numbers and linearized to temperatures in degrees Centigrade by a scanner (System 1000, Azonix Corp.), which also recorded the hot zone and cold zone heater voltages and currents. A set of values (temperatures, voltages, and currents) was transmitted to the MassComp over an RS-232 interface once every 2 seconds.

Digital filtering, in the software, of the input thermocouple data was necessary because the electronic scanner used did not have analog lowpass filters. The absence of such filters at the inputs of the Azonix 1000 caused high frequency noise to get aliased into the low frequency region during sampling, corrupting the data (Figure 4.3). It should be noted that , once aliasing has occurred, lowpass filtering the data will alleviate the problem only to some extent, but will not eliminate it. Therefore, a lowpass filter with a very flat and very narrow passband was used. This could be achieved by using a high order filter, with considerable group delay. This delay, however, was not of major consequence, since the crystal growth system is not “fast”. A 29 term Type I FIR filter was

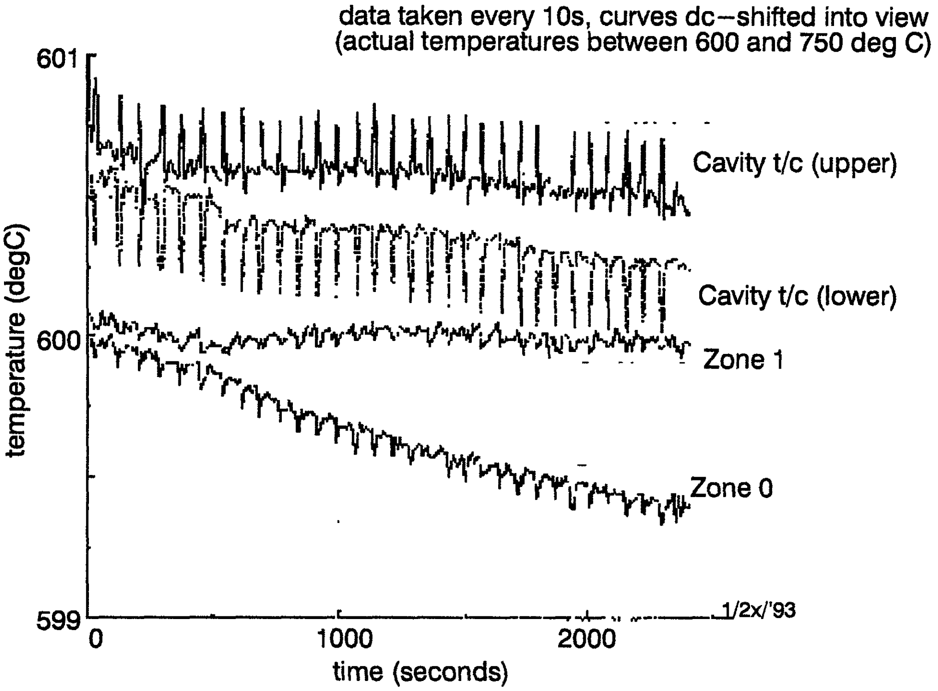

Figure **4.3** : Sample temperature data, showing extent of noise aliased into low frequency region of the spectrum.

designed using the Parks-McClellan algorithm available in Matlab (a software package from MathWorks, Inc.), by choosing an appropriate passband width, and tolerances on the ripple in the passband and stopband regions. The choice was made by an iterative process, using the constraints that the passband had to be wider than the highest frequency exhibited in the step response of the furnace, and the tolerance of gain values in the passband had to be small enough to maintain at least a 0.1 °C accuracy in the filtered temperature data.

The control loops for the cold and hot zones act independently of each other. The control law incorporates proportional and derivative control terms, transformed from the analog to the digital domain using the bilinear transformation[50]. For the furnace design used (described in Section 4.2), it was found that two independent controllers were adequate, and that a multiple-input multiple-output controller was not required.

For growth in the 'gradient freeze mode', it was found (Section 4.3) that the control constants change during growth. The control program was hence written to have the ability to change the PI constants in a feed-forward manner during growth. Another characteristic of the control program used relates to the quantization error on the output channels. The digital-to-analog converters available on the MassComp were of 12 bit accuracy (bipolar). A change in the digital control signal by one, from 1300 to 1301, say, caused a 1 °C change in the temperature of the control thermocouple(Figure 4.8). If control to within 0.1 °C was desired with the bipolar12-bit converter, the control program would settle into a form of pulse-width modulation of the power supply to approach that level of control. If this is to be avoided, higher accuracy is necessary; and the solution : two D-A converters for each power supply. The analog output of the second D-A converter was attenuated by a factor of 50, and added to the output of the first (unattenuated) D-A converter. As a result, the first D-A converter controlled the power supply in a coarse fashion, with a coarse quantization in the heater voltage. The second (attentuated) D-A converter decreased the quantization by a factor of 50. and could control the power supply voltage in finer increments (of 0.008 V).

The essential features of the data acquisition and control software developed can be summarized as:

- Thermocouple data is filtered through a 29 term FIR filter to remove aliased-in high frequency noise as much as possible.
- An independent PI controller for each of the two zones is used. Derivative control was not included because of problems with the residual noise in the thermocouple channels.
- Gain scheduling to compensate for changes in the process constants during growth.
- Compensation of quantization error in the 12-bit output channels.

A flow chart of the data acquisition and furnace control C program used in this segment of the thesis work is given in Figure 4.4, with some details of program segments being provided in Appendix B. [The program version used for the results

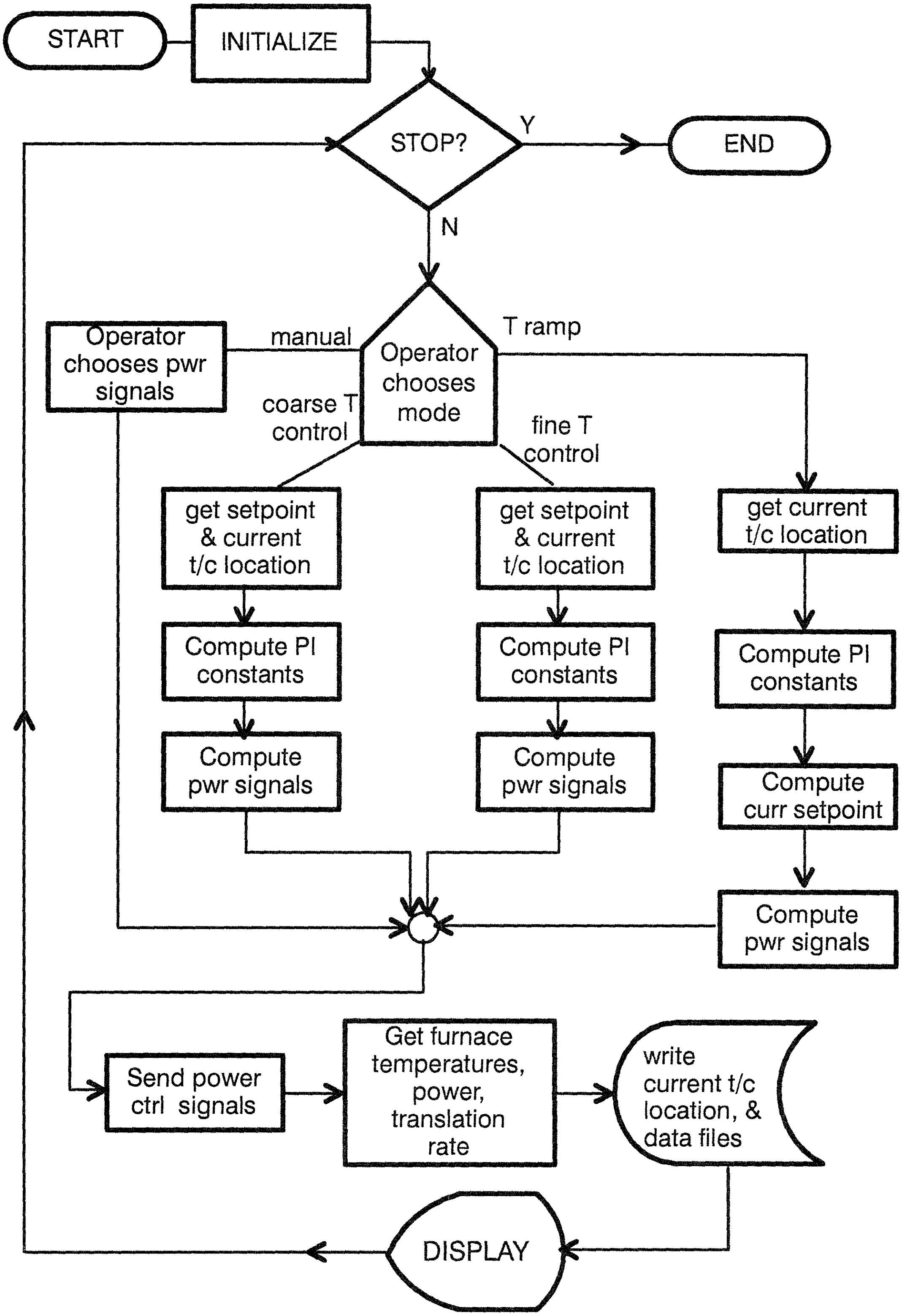

Figure **4.4 :** Flow-chart for “adc5ver3.c” , the data acquisition and control program.

reported in this thesis work is 'version 5.3' of the control program adc.c (originally written for automatic diameter control in a Czochralski furnace) – hence the name adc5ver3.c].

4.2 Furnace hardware features

The furnace is positioned on a rigid platform, in a vacuum-tight enclosure (Figure 4.5). The system can be evacuated to 60 mTorr with a mechanical pump.

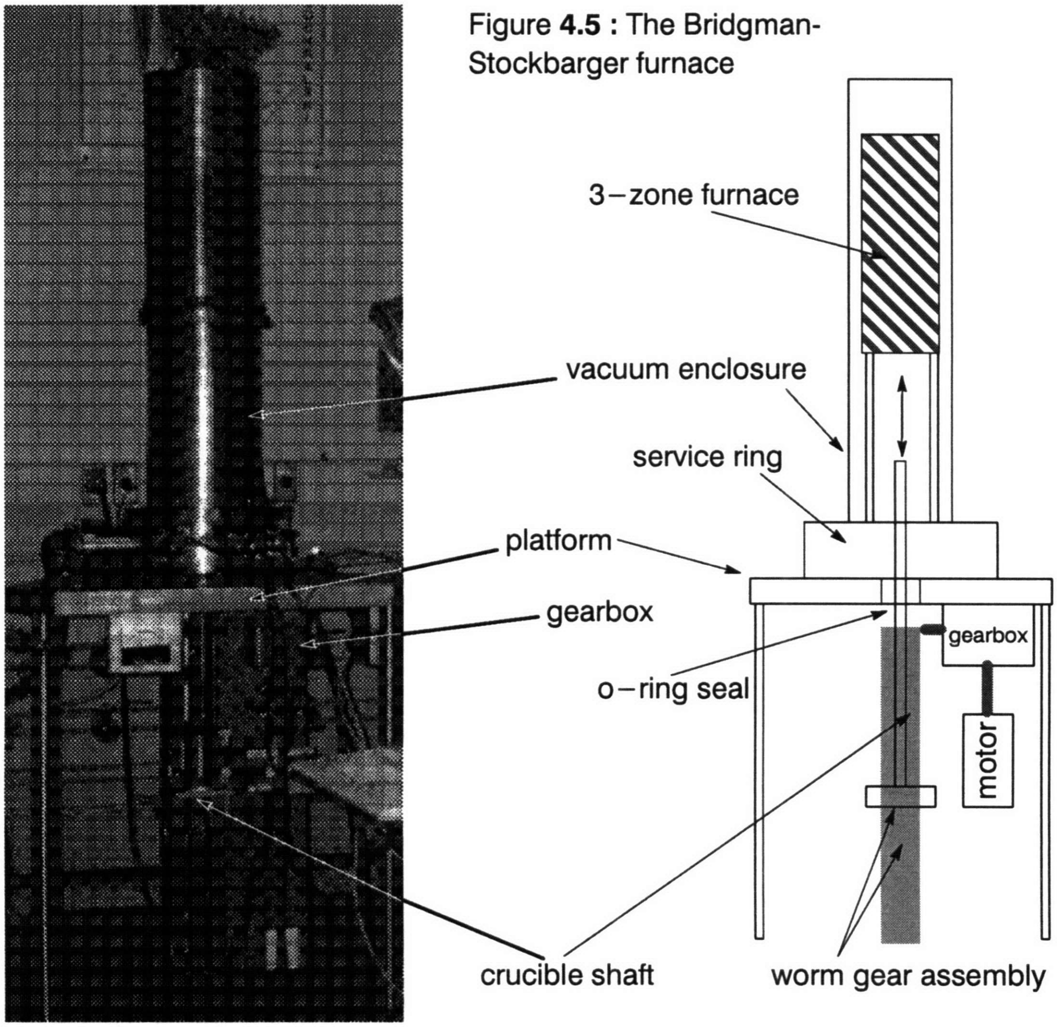

Figure **4.5** : The Bridgman-Stockbarger furnace

The translation mechanism is housed underneath the platform, with the crucible shaft entering the enclosure through an o–ring seal. The motor (EG&G Model MTE-3528-102AJ) and the reducing gearbox (Geartronics Inc.) are coupled with rubber connectors to minimize vibration. A flexible polymeric chain is used to couple the gearbox to the worm, again to minimize transmission, to the crucible shaft, of motor vibration. The worm-gear/spider mechanism moves along the worm, and is rigidly attached to the crucible shaft. A clutch is provided to permit manual repositioning of the worm-gear/spider/crucible-shaft assembly. The crucible shaft enters the furnace enclosure through an o-ring seal.

The 3-zone furnace proper (Figure 4.6) consists of two heated zones separated by a insulating gradient zone. Each heated zone has a pair of split-shell Kanthal heaters (100mm tall), rated for operation to 1200 °C at 1.2 kW per half-shell. Each heater surrounds an Inconel heat-pipe (from Dynatherm, Inc.), rated for operation to 1100 °C. The length of each heat-pipe is 150mm, its outer diameter 40mm, its inner diameter 20.5mm, and the separation between the heat-pipe and the heater is about 10 mm. The configuration thereby satisfies the recommendation of Dynatherm for the use of their heat-pipes as furnace liners – that the heat input extend over at least half the length of the heat-pipe.

For the insulation structure used in the furnace, a modular design was chosen. Rigid fibrous-Al_2O_3 cylinders and insulating boards (Type ALC cylinders, and Type AL-30 boards, from Zircar Products, Inc.) were used. The outer surfaces of the insulation were wrapped with 5mil (125 microns) thick stainless steel shim stock to reduce abrasion during handling. The ease of assembly afforded by this design contributes to maintaining the reproducibility of thermal conditions inside the furnace over repeated use. The spacing between the outer surface of the heater and the inner surface of the insulation package was about 10mm. Smaller separations , though desirable, could not have been obtained without using expensive, dimensionally non-standard furnace components.

A gradient zone length of 50mm was chosen. In a gradient freeze furnace, this zone is usually longer, so as to increase the length of the crystal that can be grown. A gradient zone length akin to that present in a vertical Bridgman furnace was used here, in order to maintain a measure of similarity between this and the ensuing phase of the project (where the Bridgman mode of operation was studied). The gradient zone has an inner wall (2mm thick) of Inconel, which acts as a spacer

Figure 4.6 : Furnace with model (graphite) charge and control thermocouples moving through furnace bore

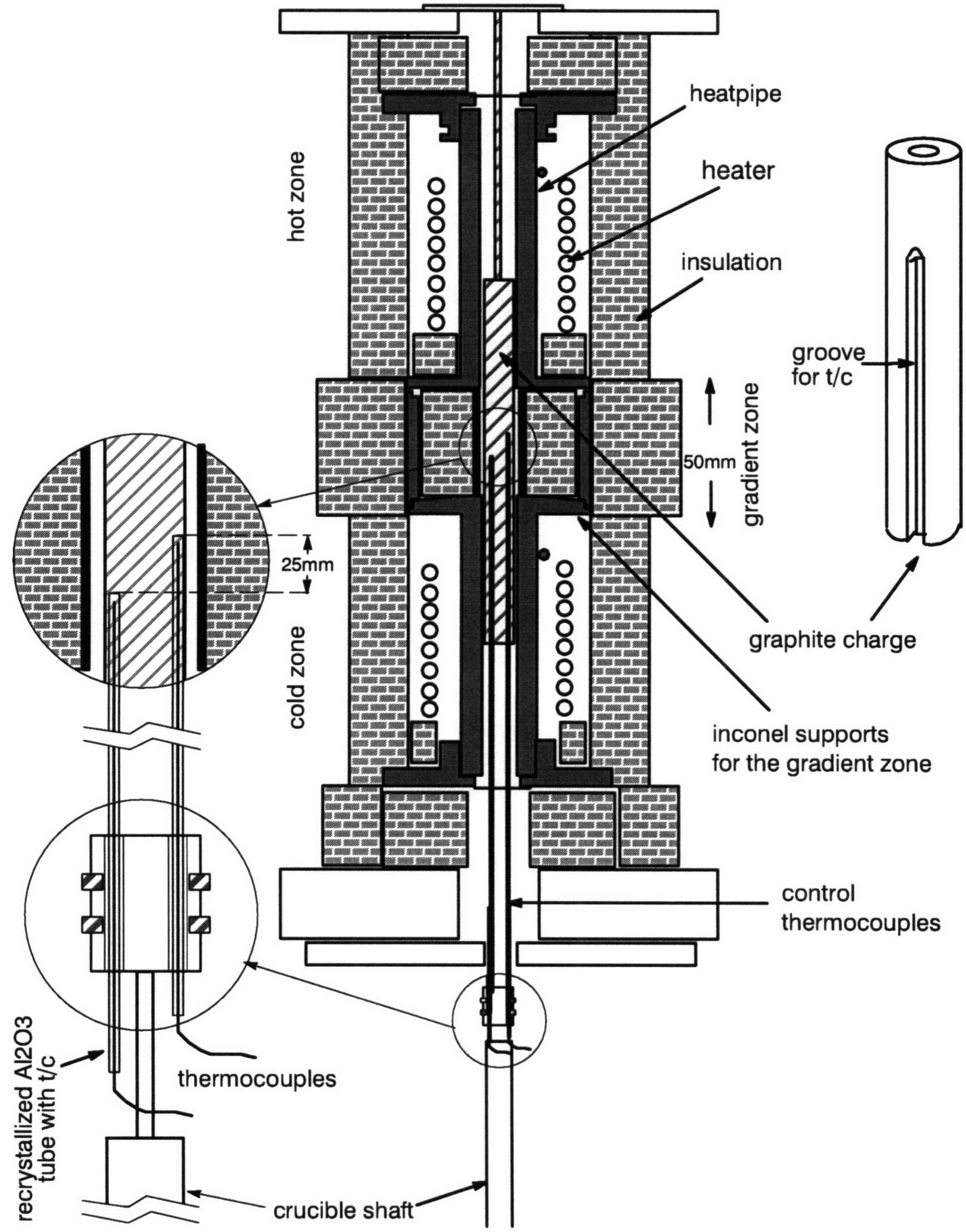

between the heat-pipes, and increases axial heat flow. The spacer is backed by an alumina cylinder (25mm ID, 90mm OD), which is in turn surrounded by an outer Inconel cylinder, of 6mm wall thickness. Outside this inconel cylinder is the final layer of Al_2O_3 insulation, with an outer diameter of 175mm. The gradient zone is bounded, on top and bottom by Inconel flanges that are mounted onto the heat-pipes.

Graphite was used a model material in the thermal characterization of the furnace the gradient freeze mode (GaSb was the material that was being considered for growth in the furnace, after thermal modeling studies were completed). Graphite was selected because : it is a material that has well-known properties (Table 4.1); its thermal conductivity is similar to that of GaSb (which was expected to be grown after thermal modeling was completed); the operating temperature (of about 700°C) is well within the capability of graphite when used in an inert atmosphere; and because it is readily machined.

For the thermal characterization of the system, a graphite rod was used. It was150mm long, and machined to fit into the heat-pipe bore, with a clearance of less than 500 µm on a side. Two 4mm wide grooves were machined into the surface of the graphite charge. The grooves had a closed end, about 35mm away from the end of the top of the graphite rod (Figure 4.6). Thus, during measurements, the tip of the thermocouple riding through the groove was not radiatively coupled to the hotter regions of the furnace, and any 'chimney' effects were avoided. The rod occupied the gradient zone region of the furnace, with equal extensions into the hot zone and the cold zone. It was held rigidly in place by a threaded graphite rod (6mm dia.) fixed to the top-plate of the furnace (Figure 4.6).

Table **4.1** : Properties of POCO graphite

Grade	DFP-1, POCO Graphite Inc, Unocal Co.
Particle size	4 microns
Coeff of thermal expansion	8.1×10^{-6} m/m °C
Compressive strength	145 MPa
Flexural strength	90 MPa

Tensile strength (est. @ 70% of flex str.)	60 MPa
Hardness (SSH)	75
Electrical resistivity	1400 x 10^{-6} ohm-cm
Apparent density	1800 kg/m^3
Thermal conductivity	95 W/mK @25°C, ≈30 W/mK @ 900°C
Oxidation threshold	540 °C (results in 1% wt loss in 24 hrs) .

Type K thermocouples (Omega, Inc., and Industronics, Inc.), inconel sheathed (1.59 mm diameter), with the wires and the junction insulated from the sheath by packed MgO powder, were used in thermal characterization. A thermocouple was used to monitor the temperature of each of the two heat-pipes, and two other thermocouples, capable of moving within the furnace cavity, were used as sensors for control of the hot zone and the cold zone heater powers. The two control sensors were held within hollow recrystallized Al_2O_3 tubes (3.2 mm outer diameter), to provide rigidity while they were being translated in the grooves of the graphite charge. The thermocouples were coupled to the crucible shaft of the furnace by an Aluminum fixture, where the thermocouples were locked in place by set-screws (Figure 4.6). This ensured that the rate of translation of the furnace crucible shaft was equal to the rate of translation of the two control sensors. The temperatures of the two heat-pipes were also monitored during the experiments.

4.3 Thermal characterization of the furnace

Prior to each experiment, the furnace was baked out (at zone temperatures of around 300°C - with the stainless steel enclosure at around 150°C), and back-filled with inert gas (Argon) at 14 psig. Flow of inert gas was maintained during the experiments, and was monitored with a bubbler. Ambient gas entered the system at the top of the furnace, and exited at the bottom.

4.3.1 Reproducibility

The reproducibility of furnace temperature conditions is illustrated through two runs, separated by 24 hours, where the furnace was controlled to the same setpoints (780°C for the lower control thermocouple in the furnace bore, and

820°C for the upper). For this reproducibility test, the thermocouples were held at fixed locations in the furnace, at the middle of the gradient zone. As seen in Figure 4.7, the control thermocouples were within 0.5 °C of the respective setpoints. after the initial transients. The hot zone was also at the same temperature (to within 0.5 °C) in the two runs. The cold zone temperature on the second day's run was 2°C higher than the temperature recorded on the first day's run (709°C). It was found, as is shown in the last pair of plots in Figure 4.7, that the power drawn by the two zones was, to within 1%, the same in both experiments. It was also verified that the power requirements at the same temperature were within 5% of each other, even when the furnace was taken fully apart and reassembled.

4.3.2 Furnace tuning

The furnace was tuned using the Ziegler-Nichols methodology[51]. Both zones of the furnace were brought close to the operating point, under manual control of the power input, and allowed to equilibrate. One zone was left at constant power, the other was subjected to a unit step in the power input (using the attenuated AD converter (ADC) described in Section 4.1, the total signal was raised from 1300 to 1301 ADC counts). The step response of the relevant thermocouple was recorded. This was analyzed to extract the delay time, L, and the time constant, T, of the system (assuming a first-order plant). The values of L and T were used in the Ziegler-Nichols formulae to get estimates of the proportional constant and the integral time constant.

$$P = 0.9\frac{T}{L} \qquad T_i = \frac{L}{0.3}$$

These constants were then used as the basis for manually fine tuning the system, if the response failed to be satisfactory. The step response is shown in Figure 4.8, with the delay time and time constant measurements indicated.

4.3.3 'Gain scheduling' in furnace control

In the crystal growth configuration presently considered, the location of the control sensor pair relative to the actuators (the heaters) changes during the

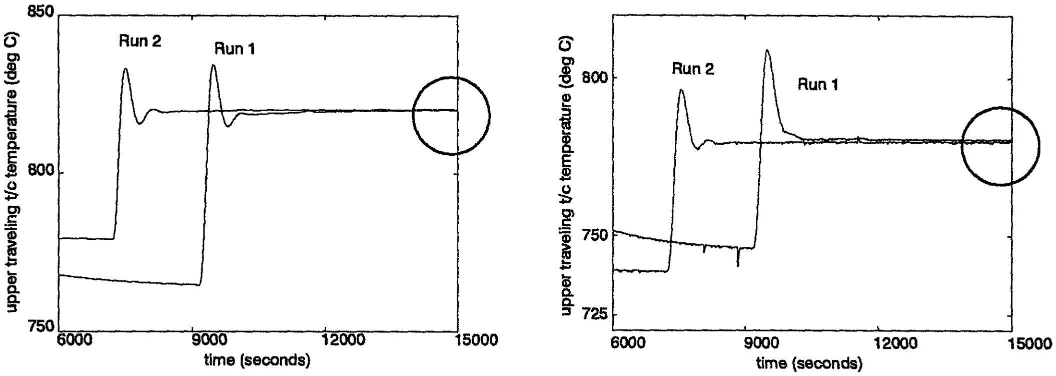

The two control thermocouples brought to the same setpoints, in runs 1 & 2.

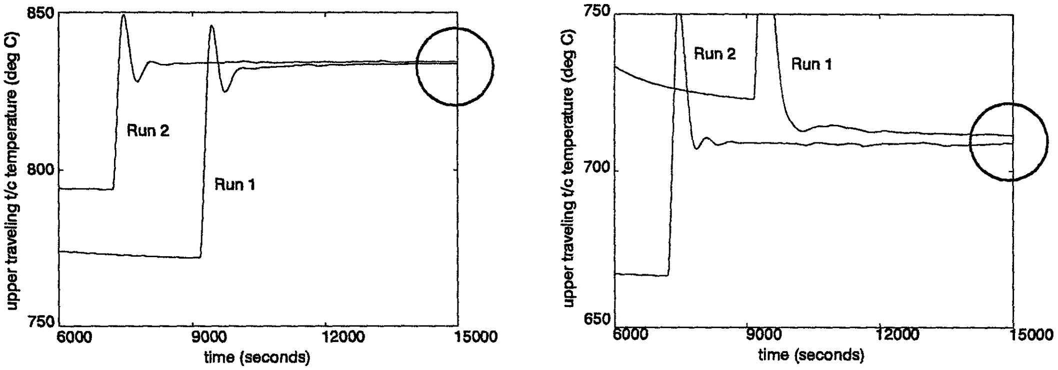

Records of the top and bottom heatpipe temperatures during runs 1 & 2.

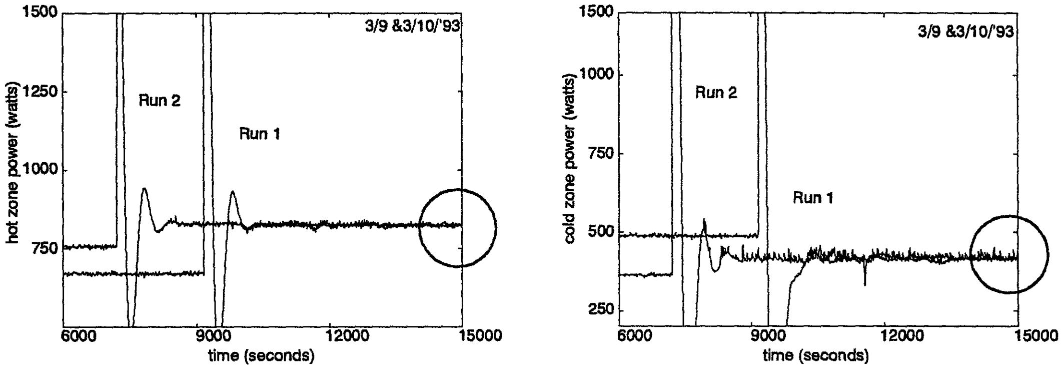

Demonstration of identical power draws at steady state, in runs 1 & 2.

Figure 4.7 : Reproducibility test results

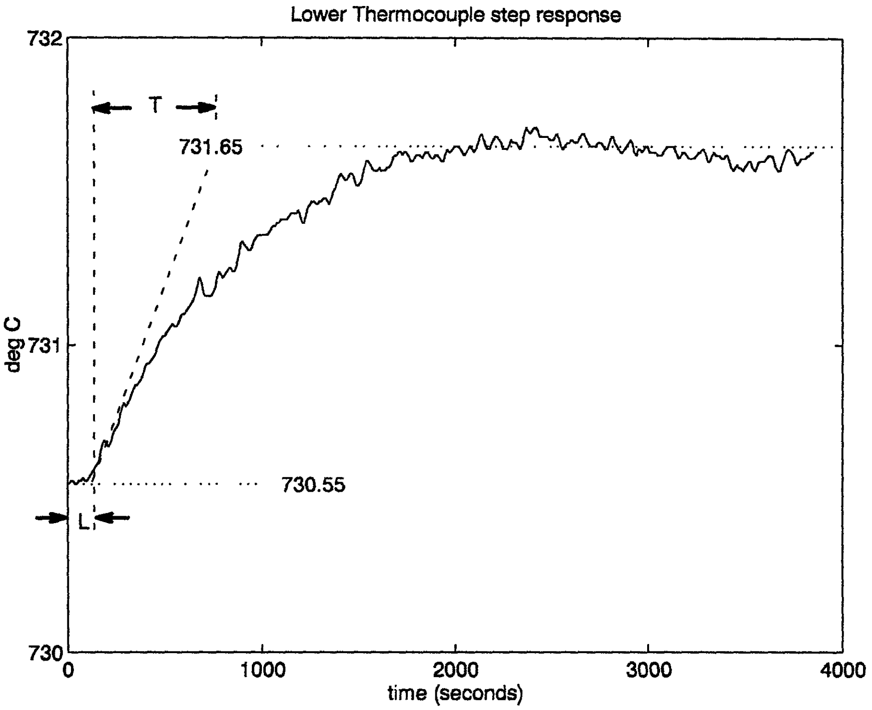

Figure **4.8** : Step response of the lower control thermocouple to a power step in the cold zone heater.

growth process, and thus results in a change of the thermal mass between the sensor and the actuator. Hence, the optimal values of the proportional and integral control constants change during the translation of the thermocouples through the charge. The process of varying the control constants in a predetermined manner, so as to track process changes, (rather than allowing the controller to adapt itself to process changes), is called gain scheduling, in control theory parlance.

In Figure 4.9, the change in furnace constants is illustrated. Curve (a) is the response of the lower thermocouple, under control, to a step change in the setpoint, when it has been tuned using the method described above. When Curve (a) was recorded, the thermocouple pair is located at the bottom at the gradient zone, as it would be at the beginning of growth. The overshoot is less than 25%, the response is only slightly underdamped, and the rise time and steady-state errors are acceptable.

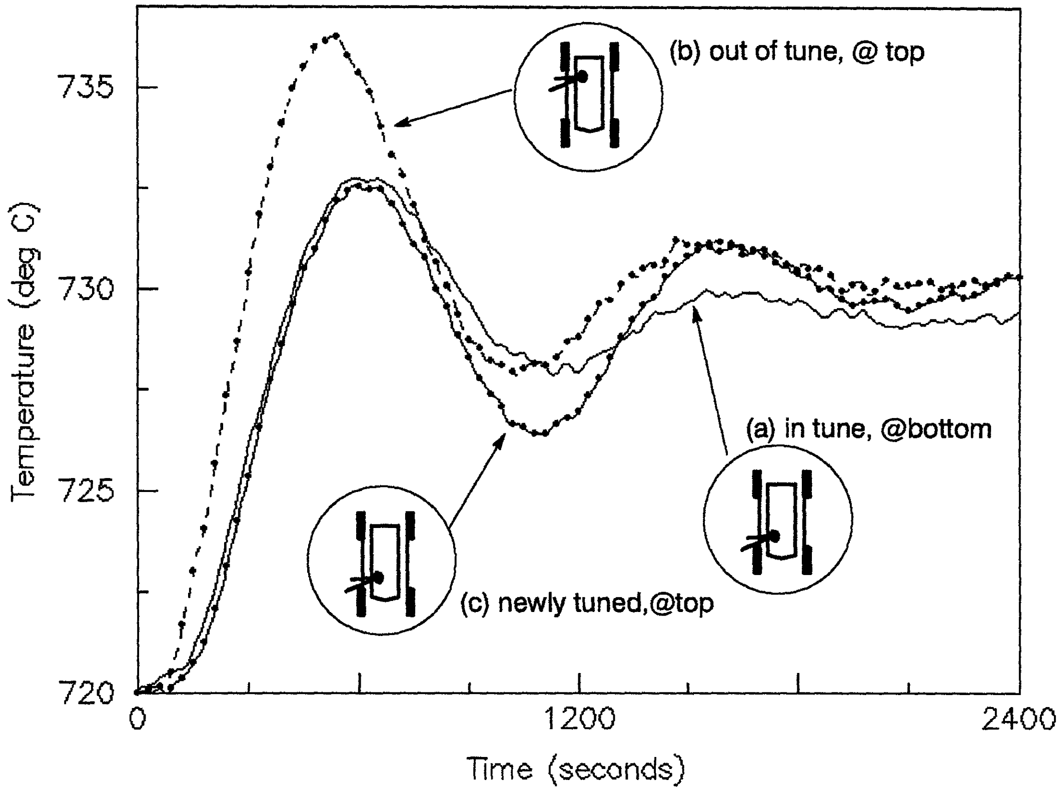

Figure **4.9** : Control parameters change due to thermocouple motion.

The thermocouple pair was then moved to the top of the gradient zone, which is where it would be towards the end of the growth process. The proportional and integral control constants were left unchanged from those used in the determination of Curve (a). The furnace was allowed to equilibrate, and the system was then subjected to the same change in setpoint. Curve (b) shows the resulting response of the control sensor to the change in setpoint. The overshoot is higher, at 65%, and the damping is lower. Finally, Curve (c) shows the result of the changing the control parameters by retuning the control loop with the thermocouples at the top of the gradient zone.

It should be noted that even an overshoot of only 25% is excessive for crystal growth applications. An overshoot and the subsequent drop in temperature could cause melt-back and uncontrolled regrowth. During crystal growth, it would be desirable to choose control constants that produce a slightly overdamped response, so that the temperature approaches the setpoint monotonically. Since thermal characteristics of the furnace, rather than growth itself, were being studied, efforts were made mainly to ensure that the responses were similar to each other at all locations of the control thermocouples, with an overshoot of less than 25% considered acceptable.

The variation of control parameters as a function of thermocouple position was established to first order from tuning experiments. The data acquisition program monitored the current location of the thermocouples, and scaled the proportional constant for the lower thermocouple from 100 (control sensors at the bottom of the gradient zone), to150 (control sensors at the top of the gradient zone). The integral constant was likewise scaled linearly from 170 to 200. For the control loop comprised of the upper thermocouple and the hot zone heater, the proportional constant was varied from 200 to 85, and the integral constant from 250 to 200, during sensor translation up the gradient zone.

4.3.4 Control of the furnace in the gradient freeze mode

The thermal performance of the furnace in the gradient freeze control configuration was studied as well, using a charge of graphite to mimic the presence of an ampoule[52]. The results are summarized in Figures 4.10 and 4.11.

In three experiments (Figure 4.10) the translation rate was maintained at 3 cm/hr (8.33 μm/s), typical for growth rates of GaAs in Czochralski furnaces. The control sensors were maintained at setpoints chosen to create a different gradient, in each test, about the putative interface (the 710 °C isotherm) in the graphite model charge. The tests show that, with the furnace configuration used, gradients as small as 4 °C/cm can be successfully maintained, and that the temperature excursions suffered under control are small. The initial transient upon start of translation shows a larger deviation from setpoint as the gradients are increased. This increase is anticipated, since the heat transferred into the region between the sensors from the hotter portions of the furnace due to motion of the charge

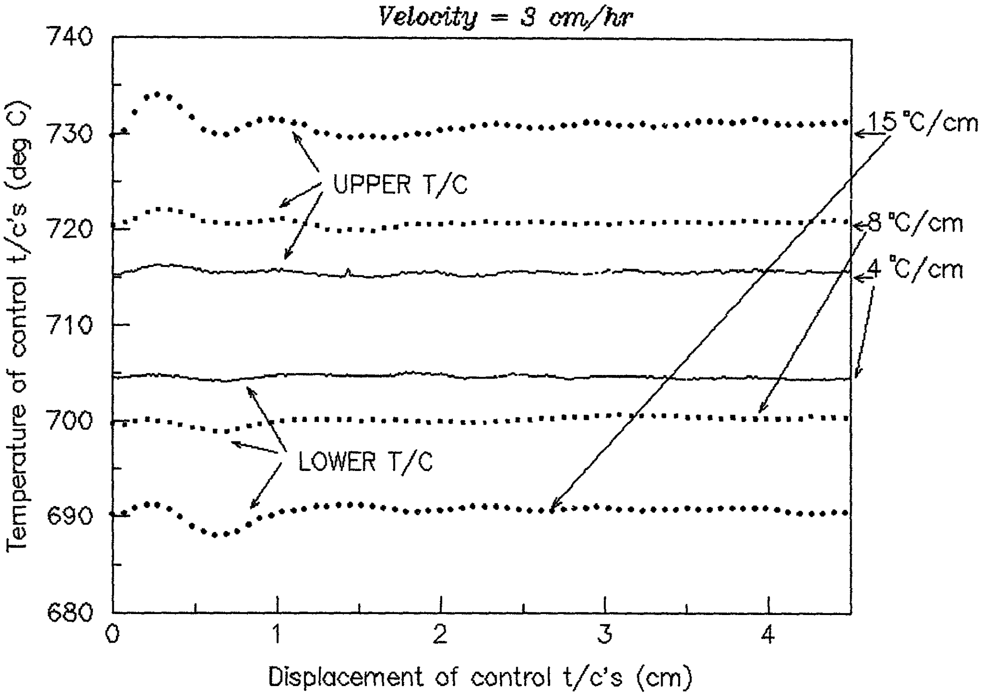

Figure **4.10** : Control of the furnace in the gradient freeze mode - influence of the gradient on control performance.

increases linearly as the gradient in the controlled region increases. To the extent that the controller has been designed to exhibit underdamped behavior, the observed excursion is as expected, increasing as the gradients increase. The advantage of smaller axial gradients is the realization of decreased thermal stress due to concomitantly lower radial gradients. Such lower thermal stresses are expected to result in crystals with lower dislocation densities. It should be kept in mind that, with lower gradients, more stringent requirements are placed on the accuracy of the control system and on the calibration of the thermocouples.

The performance of the control structure at different translation velocities, with the axial gradient held constant at 15°C/cm is shown in Figure 4.11. As the velocity is decreased, the influx of hotter charge material into the control volume takes place at a slower rate. This provides more time for the control loop to respond to the step change in velocity upon startup. At velocities of 15 cm/hr (41.67 μm/s), control effectively breaks down.

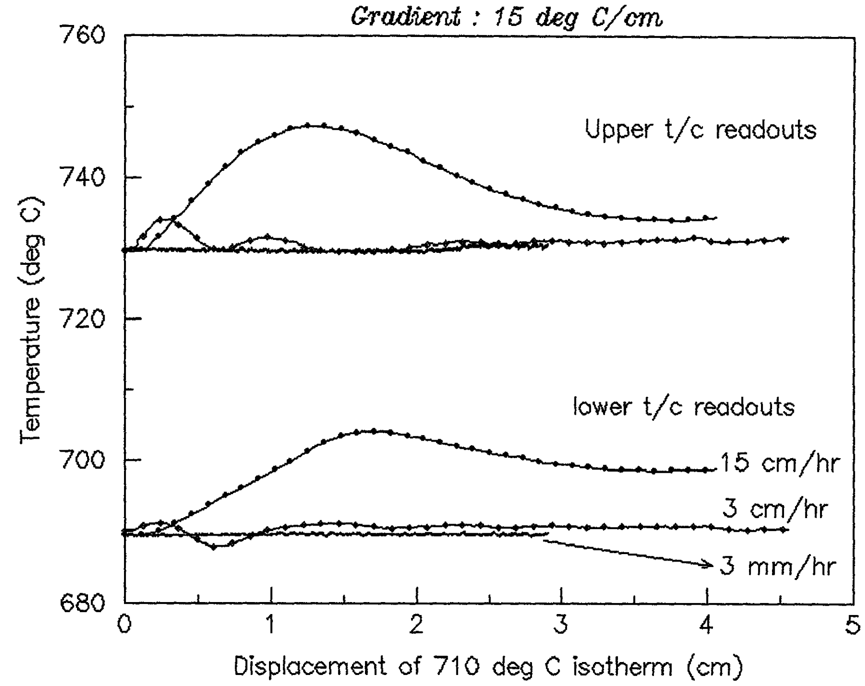

Figure **4.11** : Control of the furnace in the gradient freeze mode - influence of translation velocity on control performance.

4.4 Summary

A model charge of graphite was used to study the behavior of the furnace in the gradient freeze control configuration. This study established that :

- the relative proximity of the sensing points of two independent control loops was not found to be an issue affecting controllability,
- setpoint tracking during the process of translation could be achieved at translation rates typical of crystal growth
- Very low temperature gradients can be maintained between the control sensors.

The experiments also pointed to the importance, in a control configuration where the sensors are far removed from the actuators, of having a low noise data acquisition system, with adequate quantization of the output channels.

Chapter 5 Thermal characterization of the furnace in the Bridgman growth mode

In this chapter, the thermal characterization of the furnace in the Bridgman mode of operation is described. An introduction to this mode is first provided, and then, the hardware and software features of this version of the furnace are documented. The problems to be addressed before the desired objective, thermal field control in the gradient zone, could be reached are described.

In a conventional Bridgman-Stockbarger setup, the control systems of aligned tube furnaces are set to operate at different temperatures, generating an axial temperature gradient in the furnace cavity. An ampoule with a charge is withdrawn from the hot zone into the cold zone, leading to a controlled liquid-solid phase transformation (crystal growth), as illustrated in Figure 5.1.

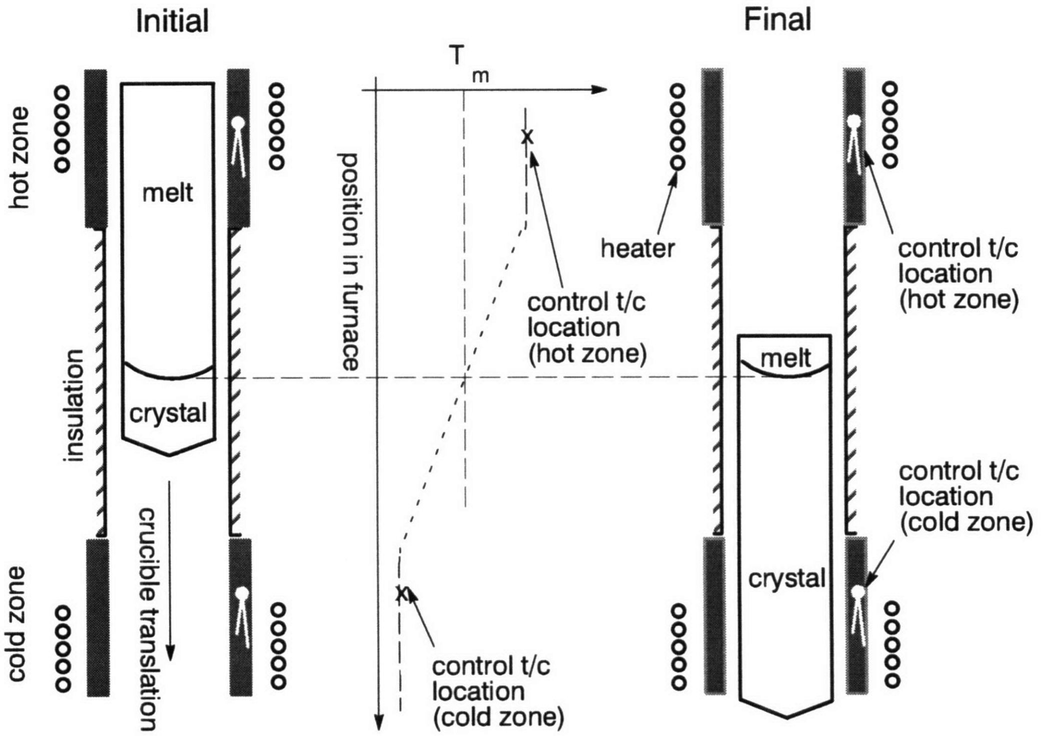

Figure **5.1** : Vertical Bridgman crystal growth with conventional temperature control

As discussed in Chapter 2, in conventional Bridgman growth, the thermal field in the gradient zone will not remain constant during growth, even if the temperatures at the conventional control locations are held constant (Figure 5.1). Hence, the growth rate will not, in general, match the ampoule translation rate ([20],[22]).

In the 'Bridgman mode' of operation of the modified furnace (Figure 5.2), the temperature control points of the furnace are moved into the gradient zone from their original locations near heaters or heat-pipes. This pinpoints the crystal-melt interface on either side of its desired location. The axial thermal gradient and temperatures (to within the limits of thermocouple accuracy) are thus fixed on the inner furnace wall above and below the desired interface location. This is indicated on Figure 5.2, through a solid line for the axial temperature profile near the interface and dashed lines elsewhere. The position of the freezing point isotherm being fixed within the furnace, the location of the crystal-melt interface is fixed.

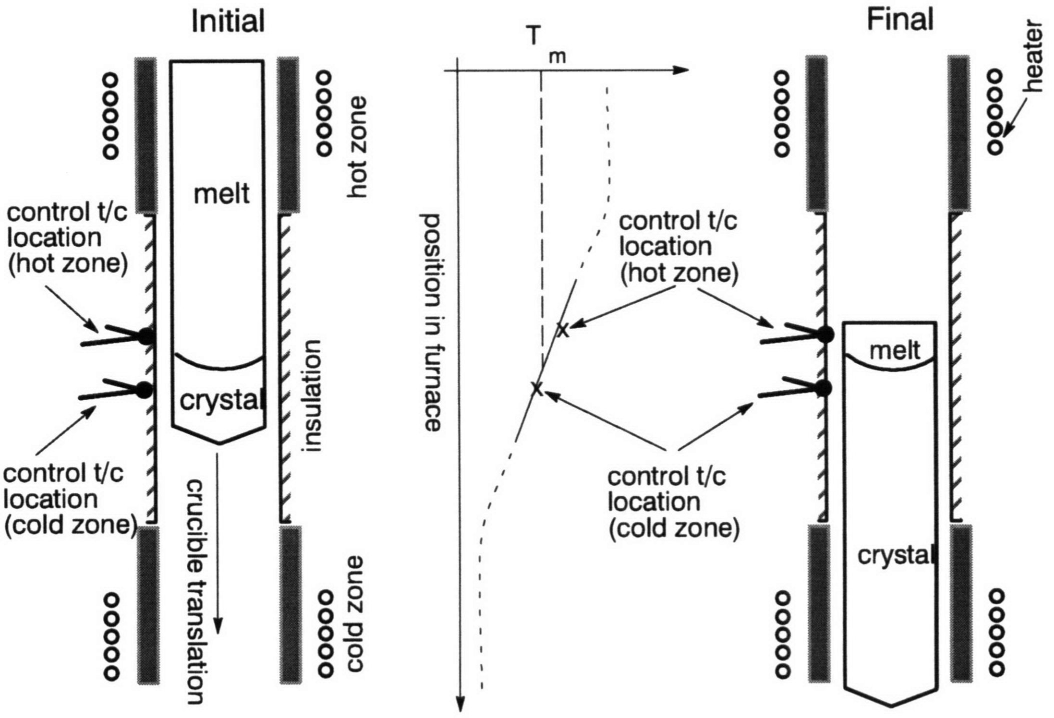

Figure **5.2** : Vertical Bridgman crystal growth with modified temperature control

As the ampoule is translated downward, the thermal coupling of the charge with the two actively heated zones of the furnace changes. Due to the control configuration of the growth system, the change in thermal coupling is absorbed by adjustments in the temperatures of the two end zones, *ie* by appropriate power changes. The microscopic rate of crystal growth can be expected to track the charge displacement rate over macroscopic distances, as will be shown in Chapter 6.

5.1 Furnace instrumentation and software features

A Pentium PC was chosen as the platform, with the data acquisition performed by a National Instruments AT-MIO-16X card housed on the PC motherboard. The card was driven by a control program in LabView, a graphical programming interface designed by National Instruments. The data acquisition card was supported by other printed circuit boards carrying out ancillary signal conditioning functions, described below.

5.1.1 Instrumentation

In the design of instrumentation, special attention was given to electrically isolating the computer-based data-acquisition subsystem from the furnace hardware, and the power supplies. To this end, an 5B01 backplane from Analog Devices was used, which was populated by isolation modules connecting the inputs of the data acquisition subsystem to the rest of the crystal growth system. The modules on the 5B01 board were: a 5B30 Millivolt Input Module for each thermocouple input, a 5B39 Current Output Module for each output, a 5B40 High Bandwidth (10 kHz) Millivolt Input Module for monitoring interface demarcation pulses. These modules use a transformer for electrical isolation, and an Analog Devices proprietary modulation-demodulation technique to assure high fidelity transfer of the dc signals across the transformer. Figures 5.3 and 5.4, printed circuit board PCB-1, show the op-amp based circuitry that dc-shifts and amplifies the computer signal outputs to match the requirements of the Current Output Modules on the 5B01 backplane. Two of the op-amps on PCB-1 are dedicated to the two

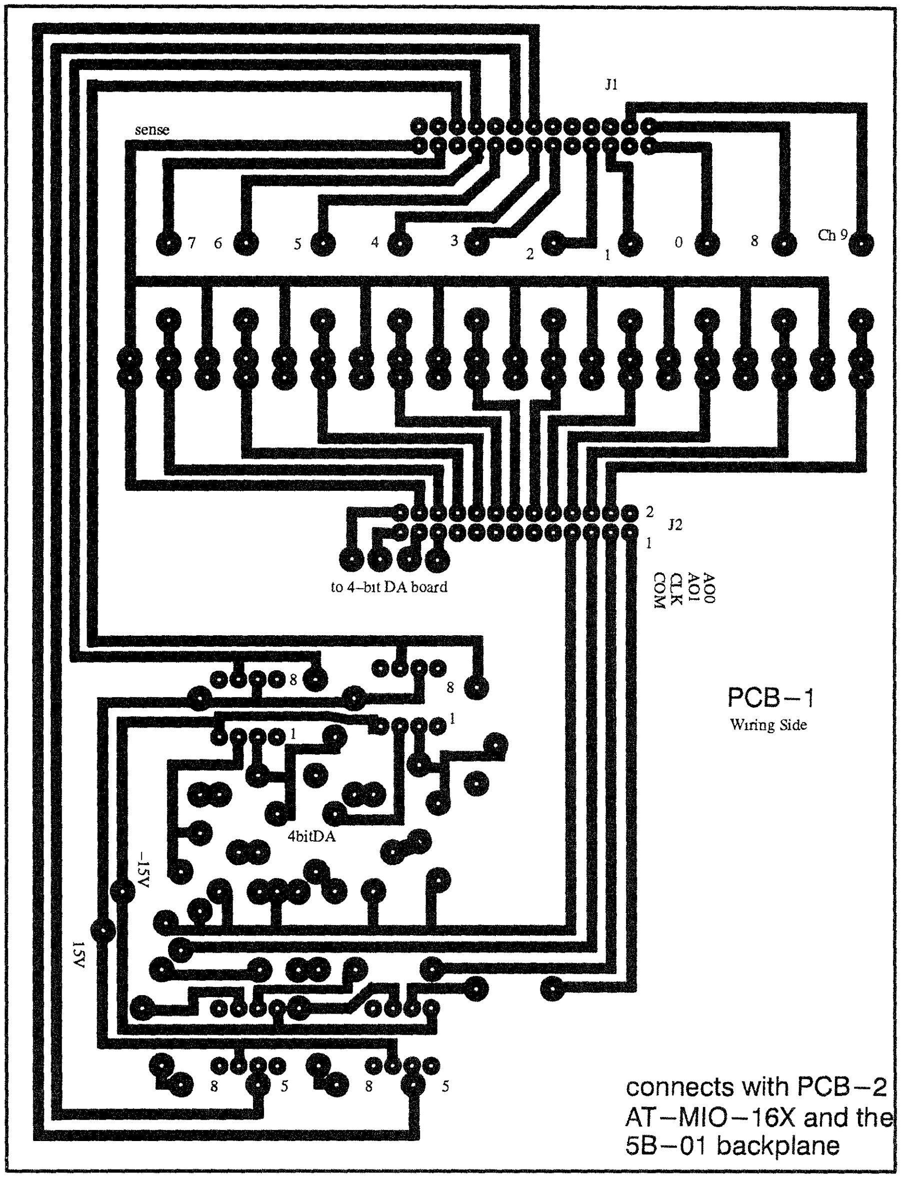

Figure 5.3 : Layout of PCB-1, a custom I/O board.

analog output channels (16-bit accuracy) provided by the AT-MIO-16X card, the third op-amp is dedicated to dc-shifting and amplifying an analog signal (of 4-bit accuracy) coming off PCB-2, while the last op-amp is used to condition the computer clock signal prior to sending it to the high bandwidth current output module.

The AT-MIO-16X card has 16 single-ended (or 8 differential) analog input channels, which are multiplexed into a 16-bit, 100 kHz, digital-to-analog converter.

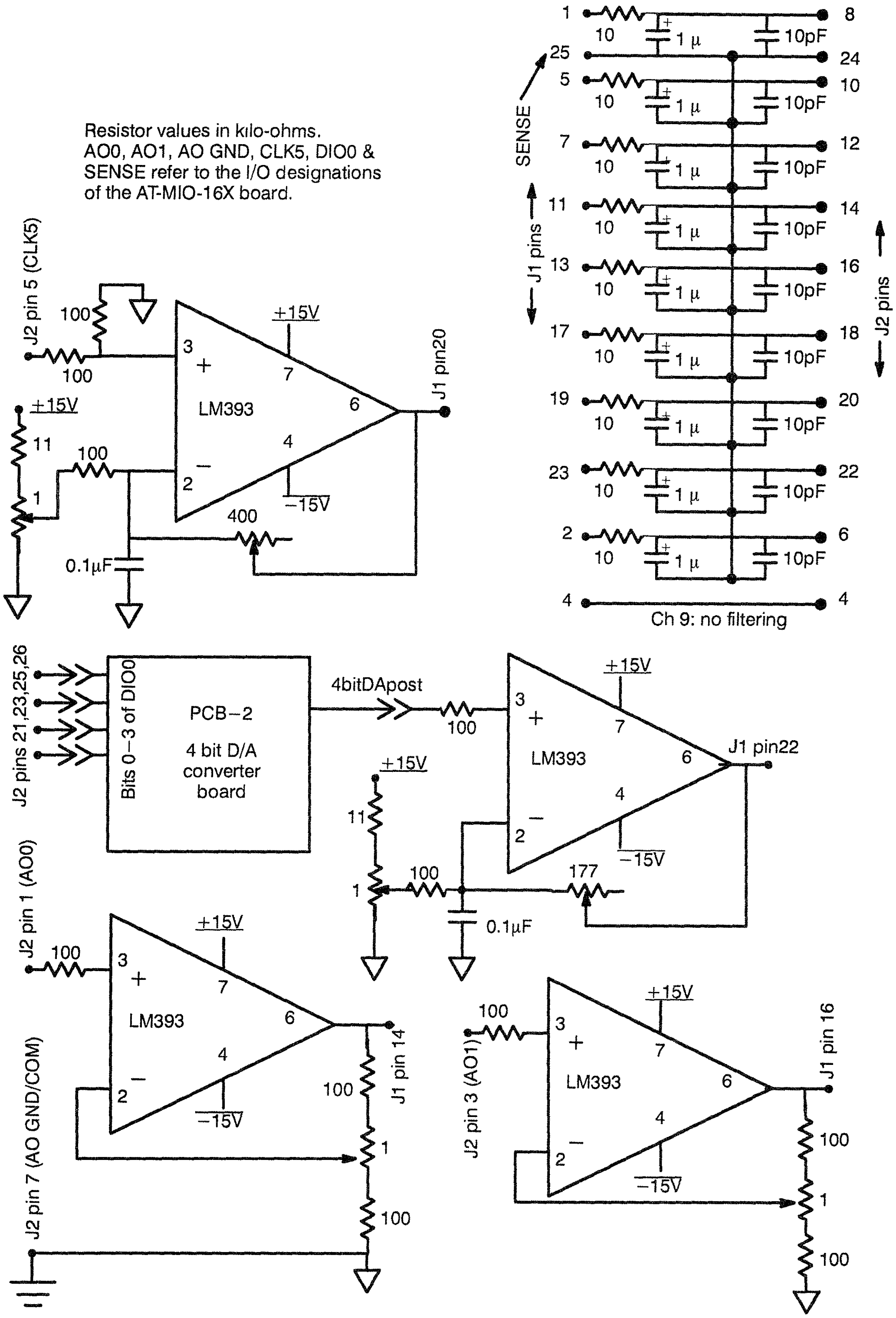
Resistor values in kilo-ohms.
AO0, AO1, AO GND, CLK5, DIO0 &
SENSE refer to the I/O designations
of the AT-MIO-16X board.

Figure **5.4** : Circuit diagram for PCB-1

The converter is exceptionally free of noise (< 0.6 LSB at the gain used, *ie* noise less than 0.01 °C), which is a highly desirable feature for the data acquisition system of the furnace. In the developed control mode, derivative control action is desired; however, the use of derivative control places more stringent constraints on the noise that can be tolerated in the system being controlled. Figure 5.5 shows a

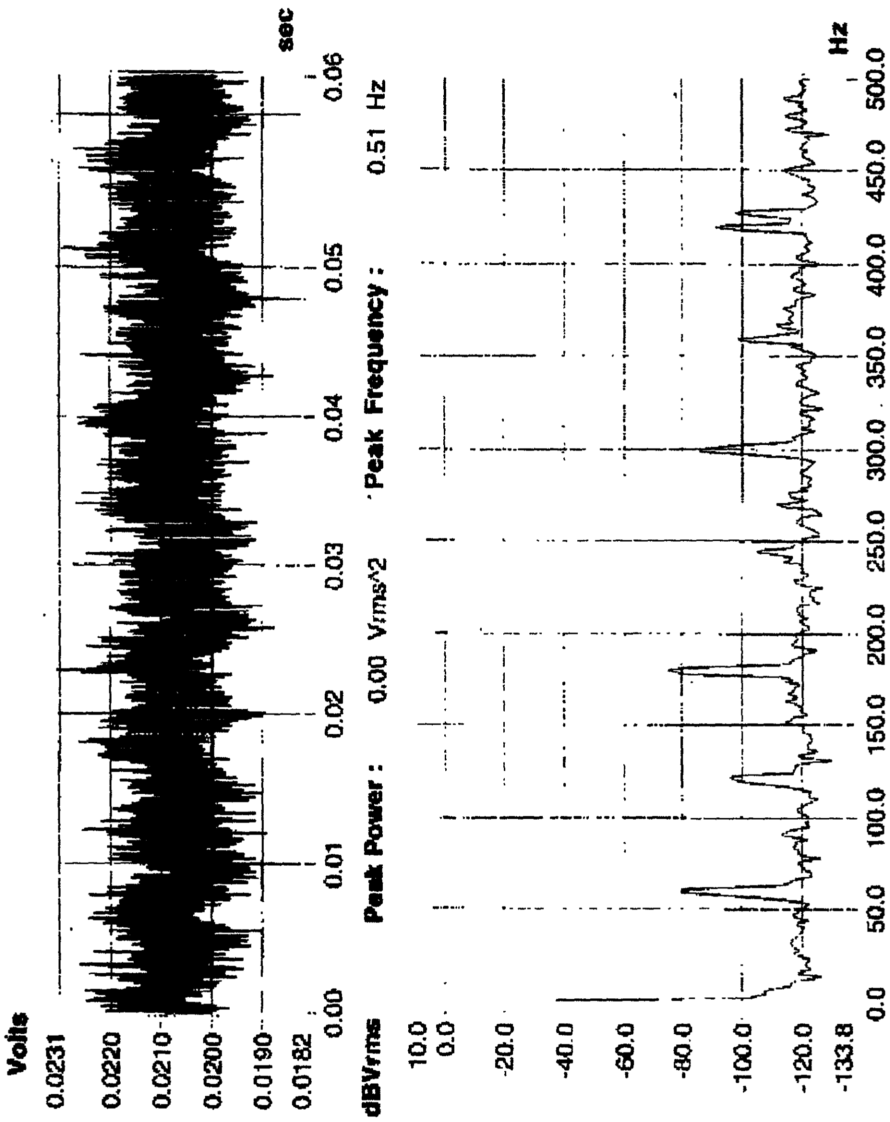

Figure 5.5 : (a) Thermocouple data channel sampled at 100 kHz (sensor at room temperature). (b) Fourier spectrum of unprocessed data, showing low noise characteristics.

Fourier transform of the data stream from a typical thermocouple channel, with sampling at 100 kHz. The largest sources of noise are power line frequency harmonics with intensities below -80 dB, with respect to the thermocouple signal at room temperature. It was also established that the characteristics of the noise remained at the same low levels when the thermocouple was measuring temperatures near 1000 °C inside the furnace.

8 thermocouple inputs could be monitored by the analog input channels during the experiments. An analog input channel was dedicated to recording the current interface demarcation pulse shapes. The remaining input channels were set aside for expansion. It was noticed that the switching power supply used by the 5B01 backplane and the modulation - demodulation process injects high frequency components into the thermocouple signal. Hence a bank of passive low-pass filters was included on PCB-1 (see Figures 5.3 and 5.4), to eliminate this source of noise, prior to sampling.

The AT-MIO-16X card has two 16-bit analog output (−5 to +5V) channels, which were used to control the two furnace power supplies. An additional analog output, needed for the translation motor control, was generated by taking the output of a digital I/O port (DIO0) to a home-built 4-bit digital to analog converter. The circuit and the PCB (PCB-2) designed for this purpose are shown in Figure 5.6.

In Figure 5.7, the transfer characteristic of PCB-2 is plotted. It shows that the nonlinearity is slight. The output of this 4-bit D/A converter (after being zeroed, amplified, and passed through an isolation module) is used as the control signal for the charge translation system. The translation system consists of a motor controller (Electro-Craft LA-5600 Linear Amplifier, Reliance Electric Company), and a motor (EG&G Torque Systems Permanent Magnet Field DC Servo model #MTE 3528-102 AJ) , equipped with a gear reducer (from 2:1 to 1000:1). A gear reduction ratio of 50 was commonly used in the experiments. The linearity of speed control was within 5%, a computer command value of 9 resulted in a translation speed of 3.05 cm/hr (8.5 μm/s), and a command value of 6 resulted in a translation speed of 1.97 cm/hr (5.5 μm/s).

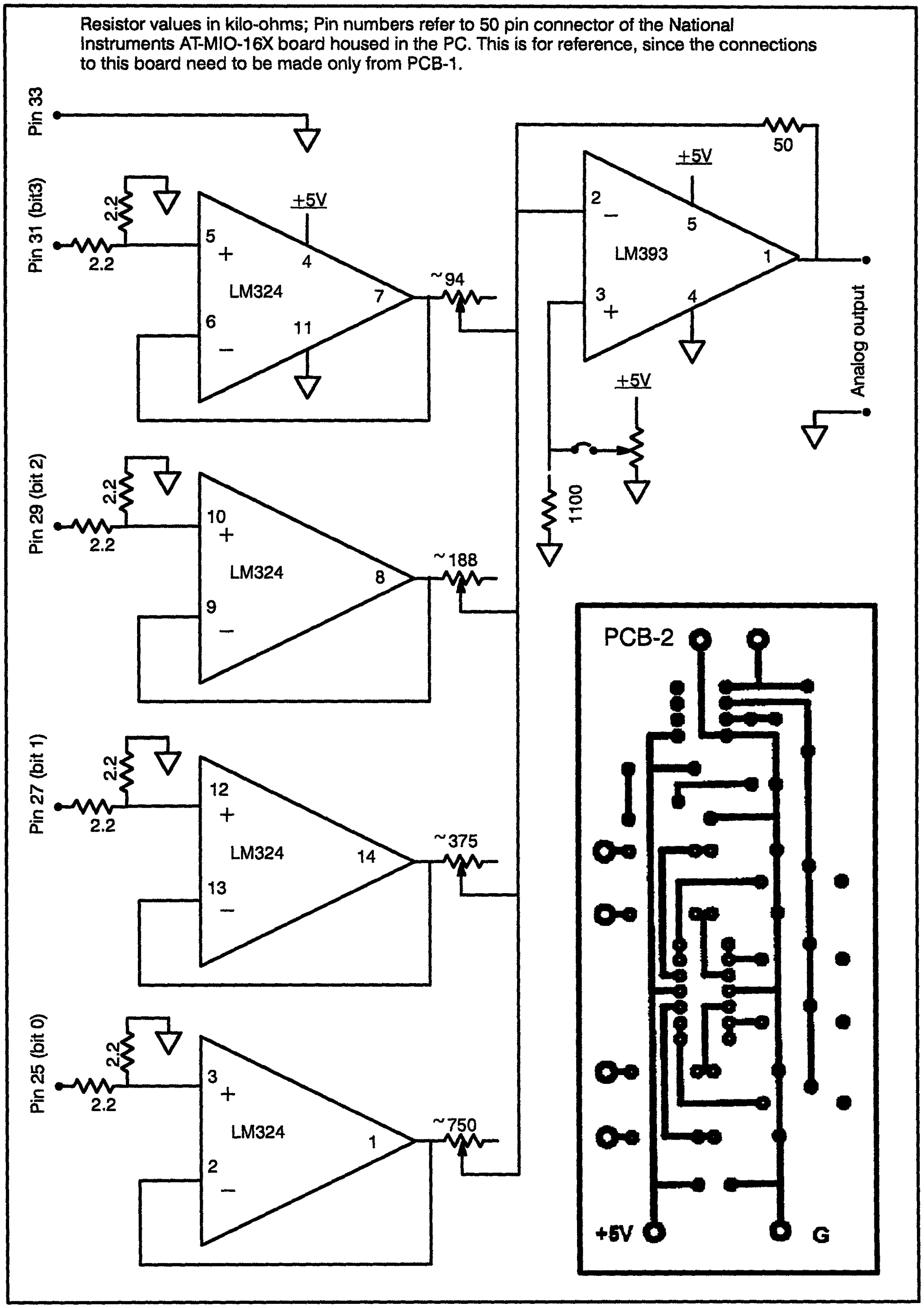

Resistor values in kilo-ohms; Pin numbers refer to 50 pin connector of the National Instruments AT-MIO-16X board housed in the PC. This is for reference, since the connections to this board need to be made only from PCB-1.

Figure 5.6 : Circuit diagram and layout for PCB-2

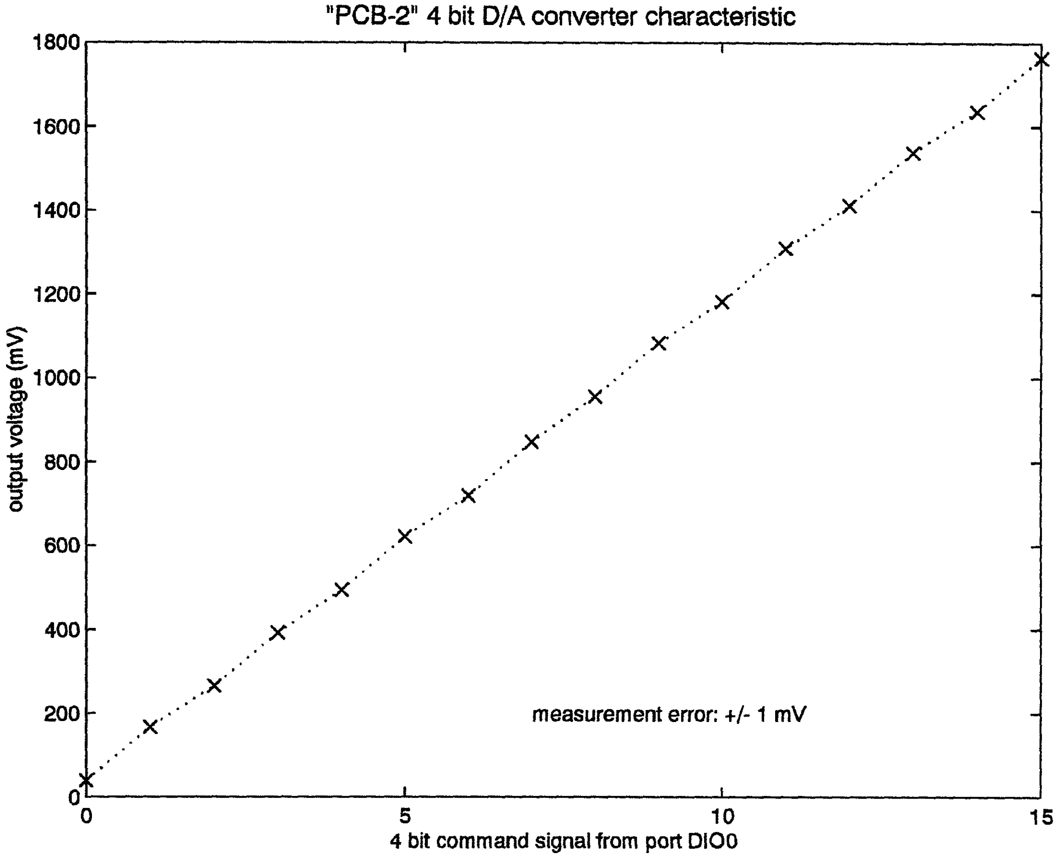

Figure 5.7 : PCB-2 transfer characteristic

signal value	output (mV)	signal value	output (mV)	signal value	output (mV)	signal value	output (mV)
0	39	4	494	8	956	12	1411
1	167	5	621	9	1083	13	1538
2	265	6	719	10	1181	14	1636
3	392	7	847	11	1309	15	1764

Another feature of the redesigned system is the capability of generating current pulses for interface demarcation, integrated into the LabView control program and the data acquisition and control hardware. One of the five timers on the AT-MIO-16X card is used to generate square pulses of pre-determined duration (between 25 ms and 75 ms), when triggered by the control program. This pulse signal ('CLK5' on Figure 5.4) goes from 0 to 5V; it is dc-shifted and amplified by an op-amp on PCB-1, so that it switches between −5 and 5V. The High Bandwidth 5B43 Current Output Module converts this −5 to 5V signal into a current pulse (electrically isolated from the computer side) going from 0 to 20mA. This current is passed through a potentiometer to create a voltage pulse of variable height, that serves as a command signal to a pair of bipolar Kepco power supplies (±20A, ±15V), operated in a master-slave configuration to generate a maximum current pulse of 40 A (36 A was generally used). This current pulse was sent across the crystal-melt interface in the growing crystal to cause interface demarcation through the Peltier effect (see Section 6.2). A sample recording of the pulse shapes used is shown in Figure 5.8. Different pulse trains are used to create an unmistakable

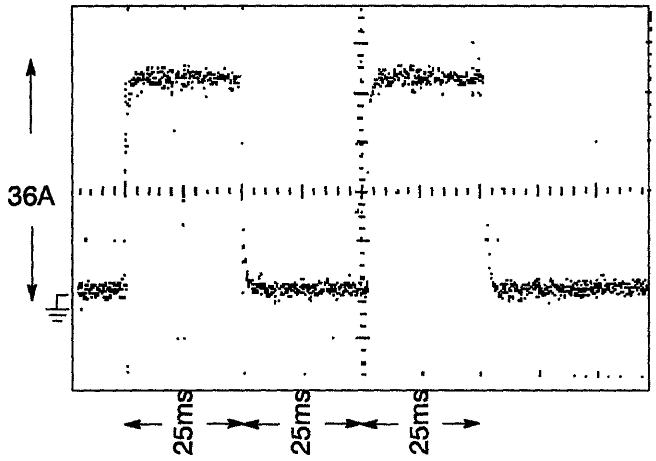

(a) Hourly ‘double pulse’

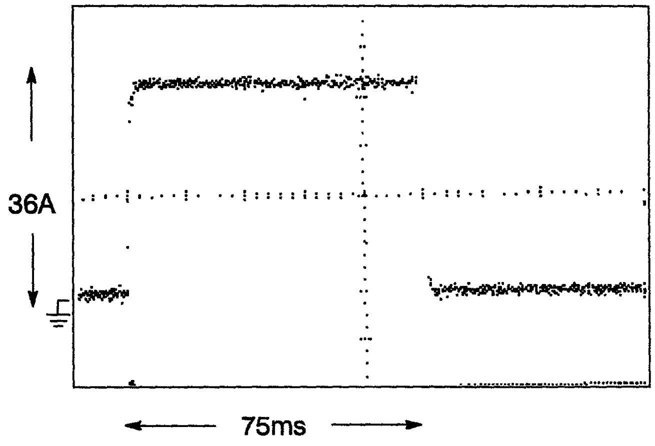

(b) ‘single pulse’ (once every 10 seconds)

Figure **5.8** : Oscilloscope traces of samples of the current pulses.

series of absolute time markers within the crystal. It should be noted, however, that some coupling between the interface demarcation channel and the thermocouple channels exists on PCB-1, possibly due to a design error that placed some wiring closer than desirable, resulting in noise.

5.1.2 Data acquisition and control software

The data acquisition and control program was designed within LabView for Windows (the Full Development version), an interface that makes program development a graphical process, and encourages top-down development of modules called 'virtual instruments', or VI's. In addition to built-in VI's available from a library, user-defined VI's with user-defined functions and iconographic representations were used in building a data acquisition and control program, which has a 'front panel' for the operator to interact with, and a 'block diagram' which represents C code that is automatically generated.

The 'Front Panel' of the Crystal Growth System.VI is shown in Figure 5.9 The top right section is visible upon startup, on the PC screen. It has controls for manually setting the furnace power (marked 'Inputs, top & bottom'), which vary the voltage of the two analog output channels of the AT-MIO-16X from −5V to 5V, thereby changing the applied voltage on the heaters from 0 to 80V. When the auto/manual switch is thrown, the setpoint controls are read, instead of the manual power controls. These setpoint controls can be seen in Figure 5.9, alongside the aforementioned manual power controls. In the automatic control mode, each zone of the furnace can be ramped up or down independently, by throwing the appropriate 'ramp switch' and then entering the ramp rate and other required information.

A schematic of the two-zone furnace (in the top right region of the box drawn on Figure 5.9) is automatically updated by the program to reflect the current control mode of the furnace (whether it is being controlled in the 'conventional' mode, or in the 'modified' mode depending on the use of a particular pair of

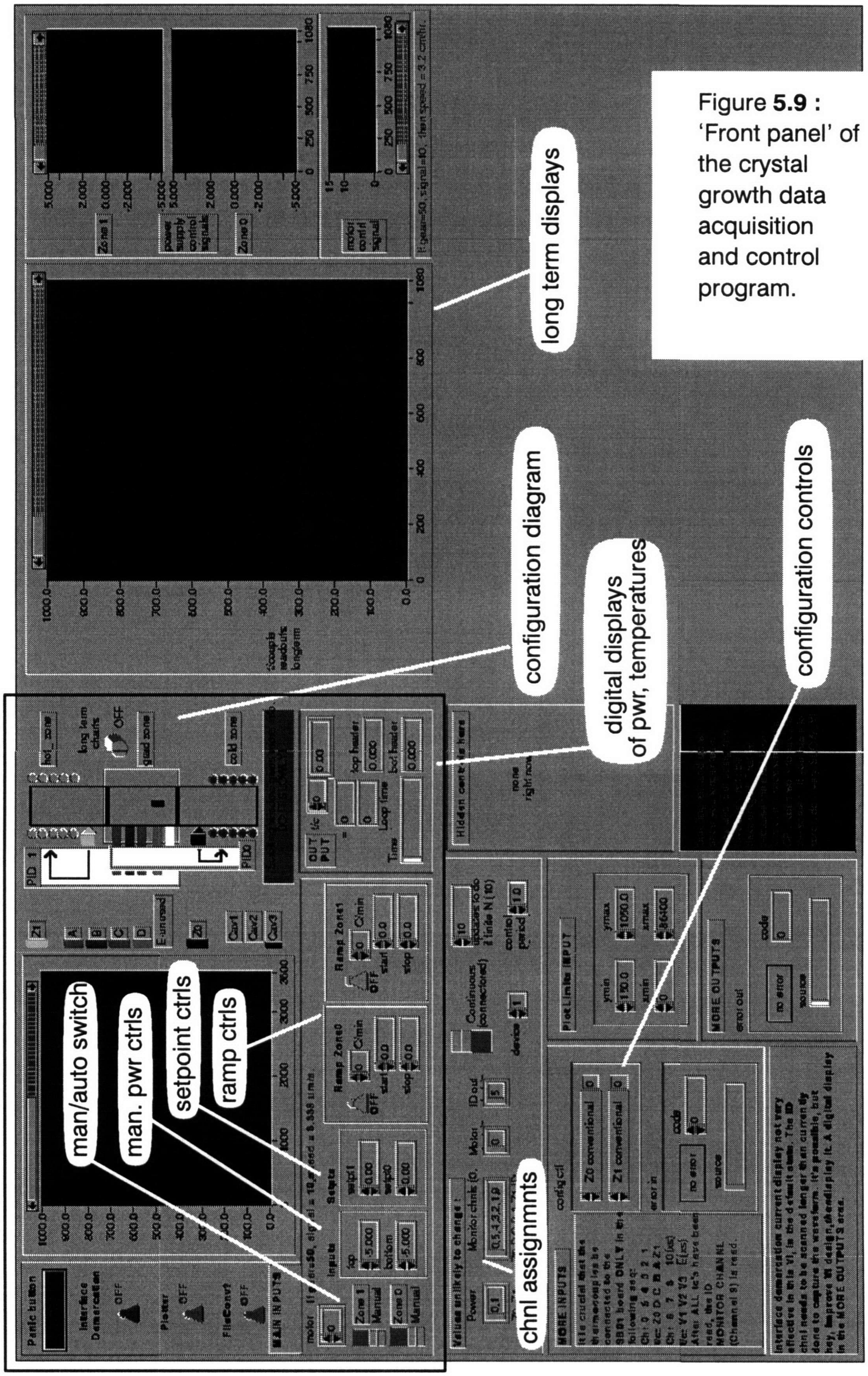

Figure **5.9** : 'Front panel' of the crystal growth data acquisition and control program.

gradient zone thermocouples). The control configuration is chosen by setting the switches (marked 'configuration controls') in the lower half of Figure 5.9. Beneath the box signifying the region visible on startup, the channel assignment and sampling time controls are located; these are to remain unchanged, unless modifications are made to the hardware, or a change is made in the number of thermocouples scanned. The measured temperatures and the instantaneous power supply control signals are displayed by the Front Panel, on oscilloscope-like displays, and on additional digital displays.

The 'Front Panel' of a virtual instrument in LabView is the user interface. The actual user program that accomplishes the task is 'written' by the user, by creating a 'Block Diagram'. This is done graphically - by drawing lines joining inputs and outputs of icons representing various functions, creating new icons for new functions, if necessary by writing fresh C code, and by grouping interconnected icons into suitable sub virtual instruments (subVI's), each with its own easily identifiable icon. The key section of the 'Block Diagram' of the *Crystal Growth System.VI* is shown in Figure 5.10, along with an easy-to-read flow chart. The control loops used in this program have proportional, derivative and integral terms. The integral term is also provided with 'antiwindup' protection, by ensuring that only the proportional and derivative terms are active in control (and the integral term frozen at its last value) unless the process variable is close enough to the setpoint. Typically, integral action was suppressed unless the temperature was within 5°C of the setpoint, *ie*, antiwindup = 5°C. The overall control law can be written as :

$$P[n] = P[n-1] + K_p\left(1 + \frac{T_d}{T} + \frac{T}{T_i}\right)E[n] - K_p\left(1 + \frac{2T_d}{T}\right)E[n-1] + K_p\left(\frac{T_d}{T}\right)E[n-2]$$

where P[n] is the power control command at time t_n, P[n -1] is the command at time t_{n-1}, E[n] is the error (setpoint minus current temperature) at time t_n, T is the sampling time (which was 1 second in this implementation). T_d is the derivative constant, while T_i is the integral control constant[53].

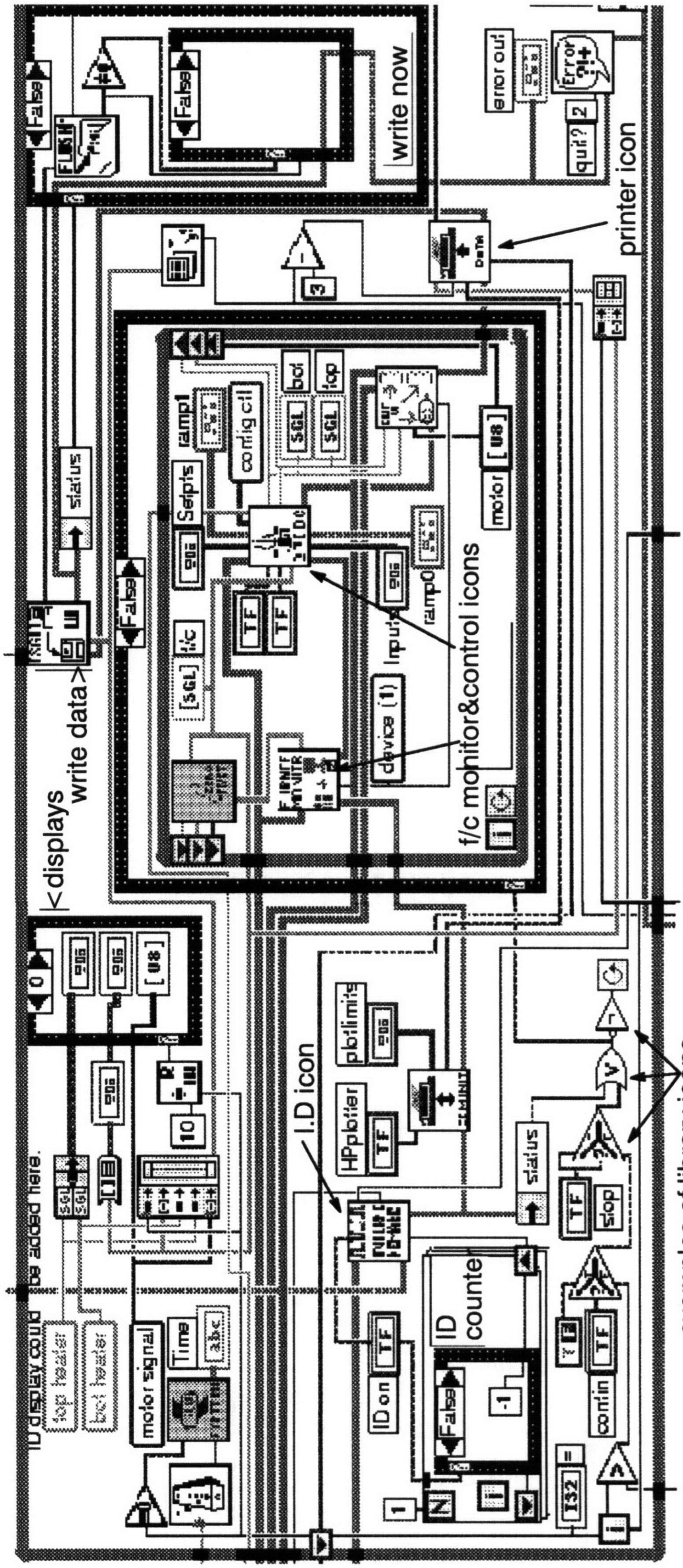

Figure **5.10** : Segment of 'Block Diagram' of Labview control program

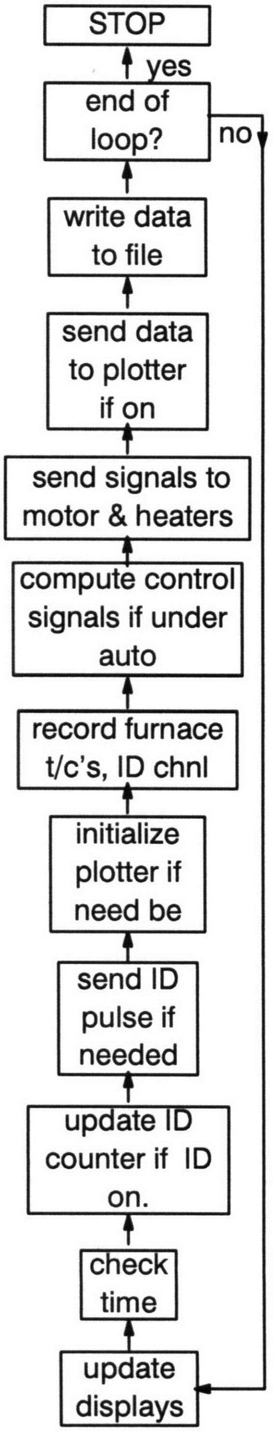

Taking the Z-transform of the above control law, and rearranging terms, the nature of the proportional, derivative and integral terms can be seen more readily:

$$P(z) = K_p\left[1 + \frac{T_d}{T}\frac{(z-1)}{z} + \frac{T}{T_i}\frac{z}{(z-1)}\right]E(z)$$

For convenience in implementation, however, the above equation was expressed in parts:

$$P(z) = K_p\left[E(z) + \frac{T_d}{T}\frac{(z-1)}{z}E(z) + \frac{T}{T_i}S(z)\right] \; ; \quad S(z) = \frac{z}{(z-1)}E(z)$$

S(z) is the Z-transform of S[n], which can be identified as the sum of E[n], in other words, S[n] is the integral of the error. Typical control behavior observed using this program is shown in Figure 5.11. Proportional control was adequate, using

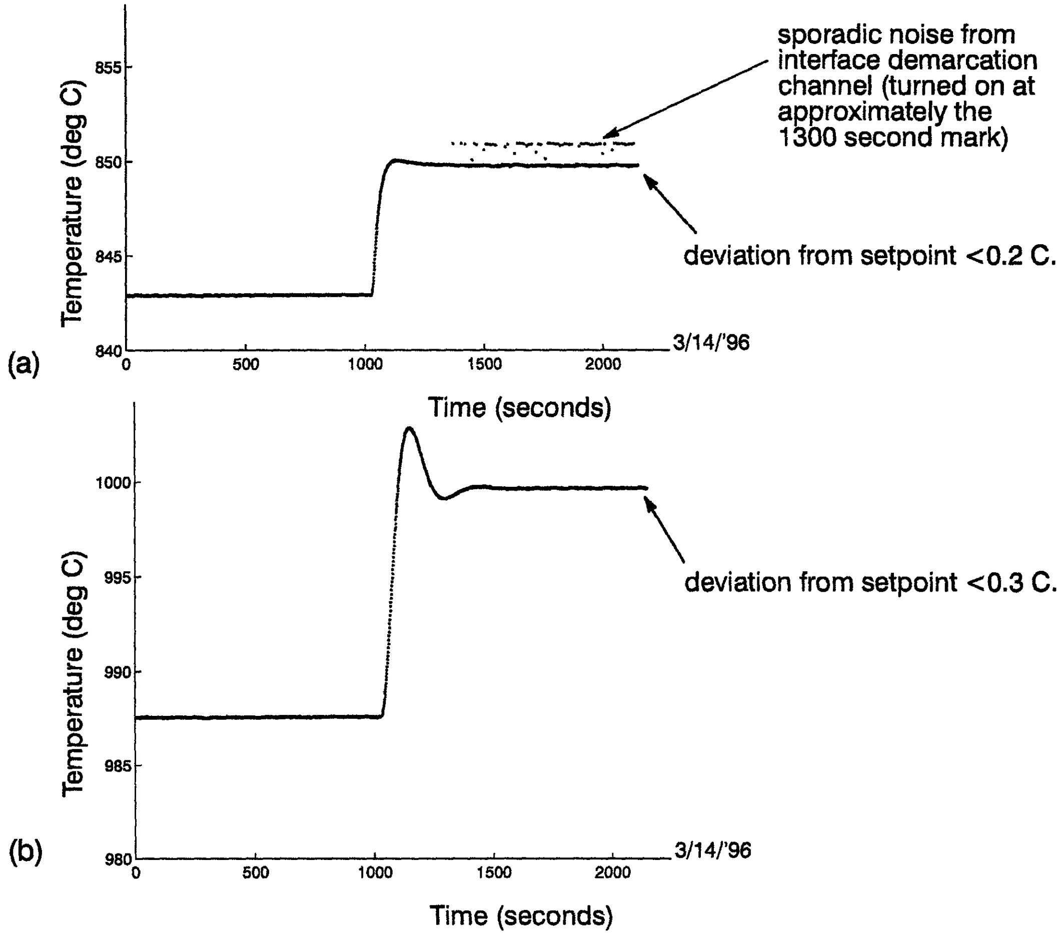

sporadic noise from interface demarcation channel (turned on at approximately the 1300 second mark)

deviation from setpoint <0.2 C.

3/14/'96

deviation from setpoint <0.3 C.

3/14/'96

Figure **5.11** : Setpoint step response of the temperatures of (a) bottom heat-pipe, and (b) top heat-pipe

$K_{p,zone0}$= 0.32, and $K_{p,zone1}$ = 0.25 . It shows, for the cold zone temperature data, an increase in noise when interface demarcation is turned on. This effect is attributed to the design flaw in PCB-1 mentioned before.

5.2 Thermal characterization experimental results

The thermal behavior of the furnace was characterized using a dummy charge of hot-pressed boron nitride (grade HBC, Union Carbide Advanced Ceramics, Inc.) to mimic the presence of a germanium crystal in the furnace cavity. The properties of 'HBC grade' boron nitride, obtained from the manufacturer's datasheet, are summarized in Table 5.1. Since the thermal conductivity of germanium liquid (at 1000°C) is 39 W/mK, and that of the solid (at 600°C) is 18 W/mK. and HBC BN has a conductivity of 29 W/mK, 'HBC grade' BN is an acceptable model for a germanium charge. with excellent machinability and adequate high temperature strength. HBC boron nitride has excellent machinability, adequate high temperature strength, and very good dimensional stability. The properties of this grade of boron nitride are well known and stable, since negligible amounts of binder (calcium borate) are present in the final product.

density (minimum)	1.90 x 10^3 kg/m^3	
chemical composition	43% B, 55%N, <1% O, <0.2% C, <0.01% metals	
specific heat, 700°C	1.844 kJ/kg-K	
maximum operating T	850°C (in oxidizing atmospheres)	
maximum operating T	2000°C (in inert atmospheres or vacuum)	
resistivity	1 x 10^{13} ohm-m	
Th. conduc(W/mK) 500°C	29.2(∥ pressing direction)	16.7 (⊥ pressing directn)
Th. conduc(W/mK) 800°C	29.2(∥ pressing direction)	16.7 (⊥ pressing directn)
coeff. th. exp(to 1200°C)	0.8 x 10^{-6} (∥)	0.4 x 10^{-6} (⊥)
compressive str (Pa)	4.2 x 10^6 (∥)	5.25 x 10^6 (⊥)
Flexural str. (Pa) ,25°C	1.75 x 10^6 (∥)	2.1 x 10^6 (⊥)
Flexural str. (Pa),1500°C	4.2 x 10^6 (∥)	7 x 10^6 (⊥)

Table **5.1** : Selected properties of hot-pressed boron nitride (grade HBC)

The boron nitride rod (Figure 5.12) had a central hole and a peripheral

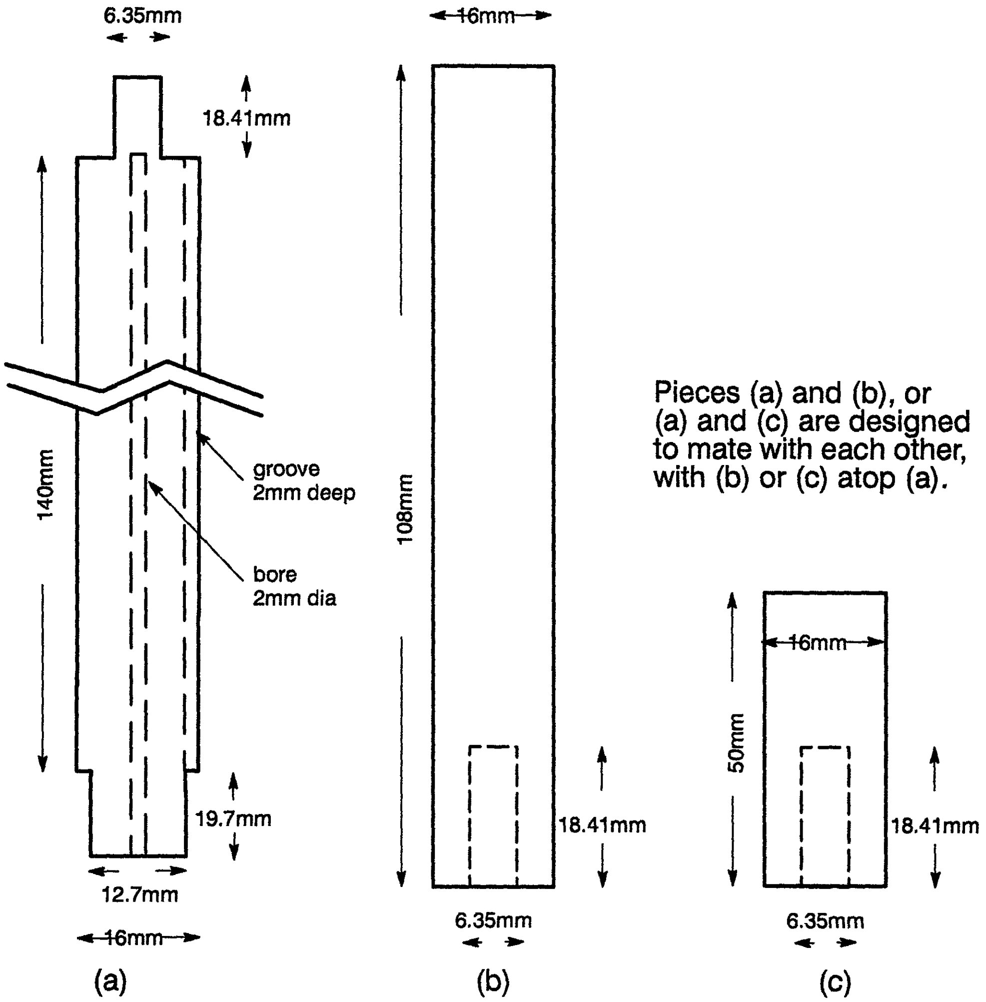

Pieces (a) and (b), or (a) and (c) are designed to mate with each other, with (b) or (c) atop (a).

Figure **5.12** : Boron nitride rod used for thermal characterization.

groove. Each hole carried an ungrounded, inconel-sheathed Type K thermocouple, 1.59mm in diameter. It was ensured that the thermocouple tips were at the same height within the boron nitride. With this arrangement the radial gradient within the boron nitride between the tips of the two thermocouples could be determined. The peripheral thermocouple was within 1mm of the quartz liner of the furnace cavity. The section (a) carrying the thermocouples was topped by another section, either (b) or (a), serving as a thermal extension. The different lengths of the extension changes the thermal coupling of the charge to the hot heat-pipe. This boron nitride assembly is supported within the furnace cavity by a stainless steel tube, of wall thickness 1.5 mm (Figure 5.13).

A series of experiments was conducted to study the effects of various furnace elements on the axial thermal profiles within the furnace cavity, using the boron nitride (BN) rod as the dummy charge translating through the cavity.

5.2.1 Influence of conductive elements in the gradient zone

Wang[27] had postulated the usefulness of a 'diabatic' gradient zone in influencing the thermal profile within a gradient zone. In contrast to a fully insulating adiabatic gradient zone, a 'diabatic' gradient zone (Figure 5.14) has a ring structure of insulators and conductors. The usefulness of such a structure stems from the fact that it offers an additional method to tailor the temperature profile in the gradient zone. (The usual method of changing gradients in the Bridgman-Stockbarger furnace is to change the temperatures of the end zones. However, with the high- and low-temperature limitations of heat pipes,a limit to the flexibility so offered is imposed). The gradient zone insulation system was bounded on top and bottom by inconel flanges of the two heat-pipes. A insulating plate was interposed between the 'diabatic' gradient zone and one of the flanges. It was shown[27] that using a 'diabatic' gradient zone changes the axial temperature profile noticeably, as does the location of the insulating plate, above or below the zone. Following this concept, the gradient zone design first used consisted of an inner ring of inconel (wall thickness 1mm), which was surrounded by fibrous Al_2O_3 (Zircar Products, Inc, 'wall' thickness 40 mm). This was surrounded by an outer ring of inconel, backed by further insulation (Figure 5.15).

The boron nitride profiling tool described above was used to measure the temperatures generated in the center and the periphery of the (dummy) charge (Figure 5.16). The temperature profile along the length of the furnace was generated, maintaining setpoints of 860 °C and 960°C for the lower and upper heatpipes. The boron nitride rod was moved manually in 1 cm decrements, and

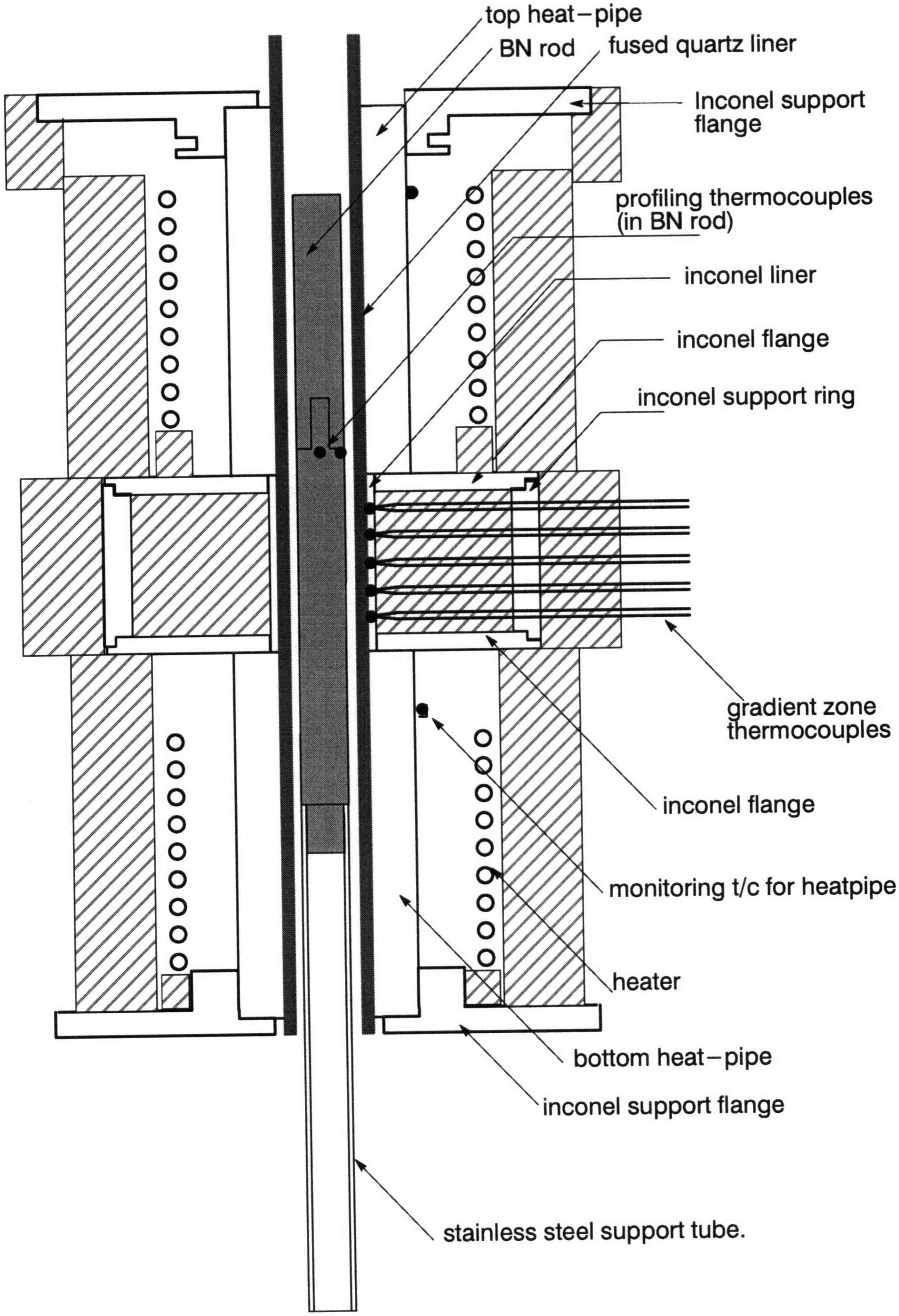

Figure **5.13 :** Schematic of the growth furnace in Bridgman mode of operation

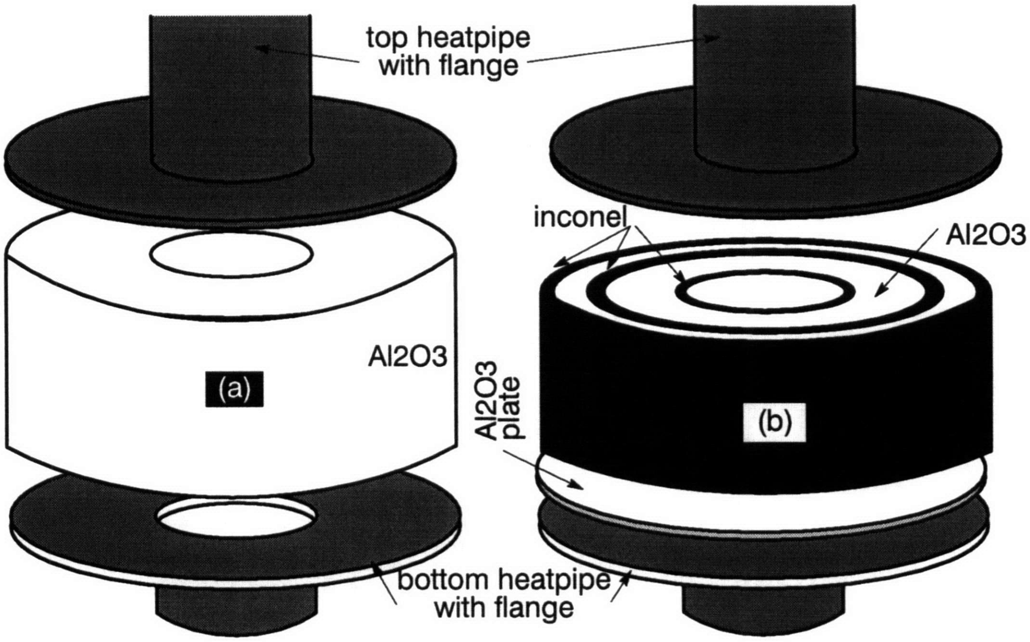

Figure **5.14 :** (a) adiabatic (fully insulating) gradient zone, and (b) 'diabatic' gradient zone (after [27])

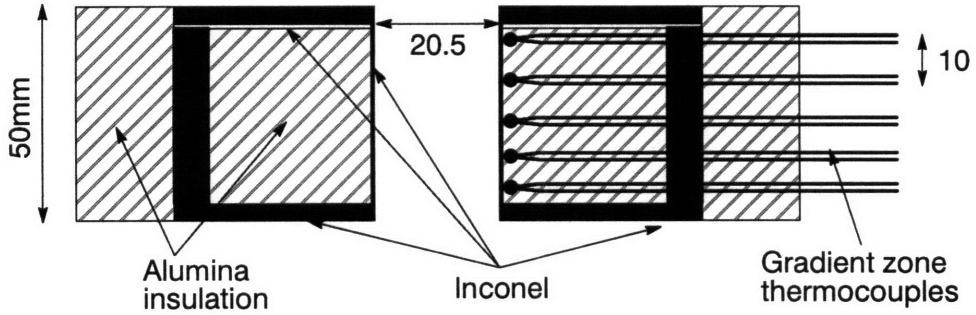

Figure **5.15 :** Gradient zone structure

thermal equilibrium ascertained prior to each measurement. The data so generated, in the hot and gradient zones, is shown by 'plus' signs in the figure. The remaining length of the furnace was profiled in a continuous fashion by moving the boron nitride rod at a steady rate of 1.03 cm/hr (2.86 μm/s), and continuously monitoring the temperatures of the two thermocouples embedded in the BN (pair of solid lines in Figure 5.16). Figure 5.16 provides evidence for the reproducibility of the furnace in the Bridgman mode. It includes data (dotted lines) from a run, separated by 4 days from the run described above (the furnace was *not*

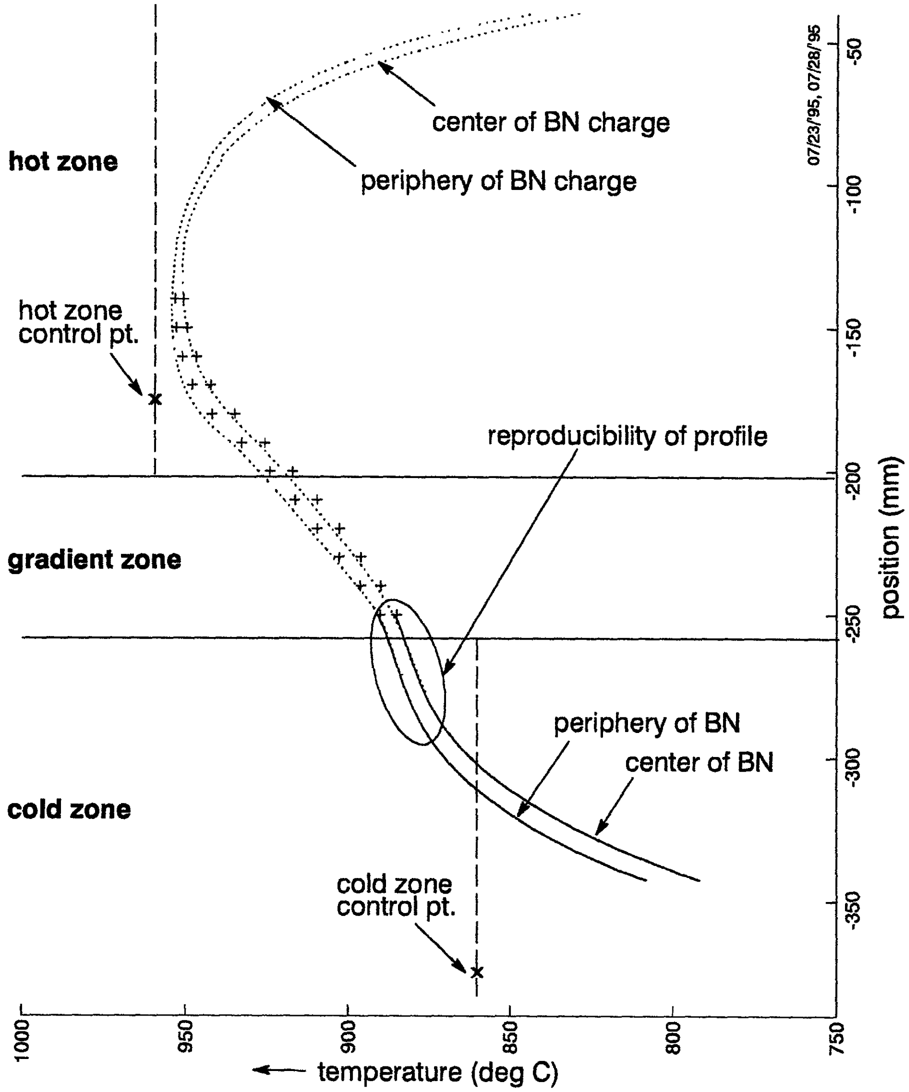

Figure **5.16** : Axial thermal profile , and radial temperature gradients, in the Bridgman furnace using an inconel-lined gradient zone.

disassembled between the two runs). With the same setpoints (indicated by dashed lines), it can be seen that the axial profile measurements in the gradient zone are identical, even at positions far removed from the control locations, and within the gradient zone. The difference between the steady-state measurements made on the second run (the 'plus' signs) and the measurements made during constant translation in the first run (the pair of dotted lines) is less than 3°C. The steady-state measurements are slightly lower in temperature than the translational measurements, and the difference is larger when the local gradient is higher. This is to be expected since the profiling run was conducted with the BN rod moving at a finite speed from the hotter to the colder regions of the furnace. (An infinitesmal displacement of the BN rod will result in a smaller amount of heat being transported into the adjacent, colder point of the furnace. This heat is transferred to the furnace wall radially, allowing the BN rod to try to reach equilibrium with the local wall temperature. A smaller amount of heat transported by the translation, into the colder point, will mean that shorter periods are necessary for 'equilibrium' to be reached. Hence a smaller local axial gradient means a smaller difference between a steady-state measurement and measurement during translation).

The difference between the temperatures recorded by the peripheral thermocouple and the central thermocouple (Figure 5.16) is a measure of the radial temperature gradient in the system. With the gradient zone configuration used, the radial gradient is, on average, observed to be about10°C/cm, and roughly constant along the gradient zone.

The gradient zone configuration was modified in the subsequent experiment by removing the inconel liner, the inconel support ring and the inconel support flanges of the heat-pipes (Figure 5.17). Fibrous alumina (Type ALC, Zircar Products, Inc.) was used as the gradient zone material, with the gradient zone thermocouples introduced along a radius through a straight, single-bore recrystallized-Al_2O_3 tube (as before). The thermal profile was measured by translation at 2 cm/hr (5.55 μm/s) of the BN rod with its two thermocouples. After

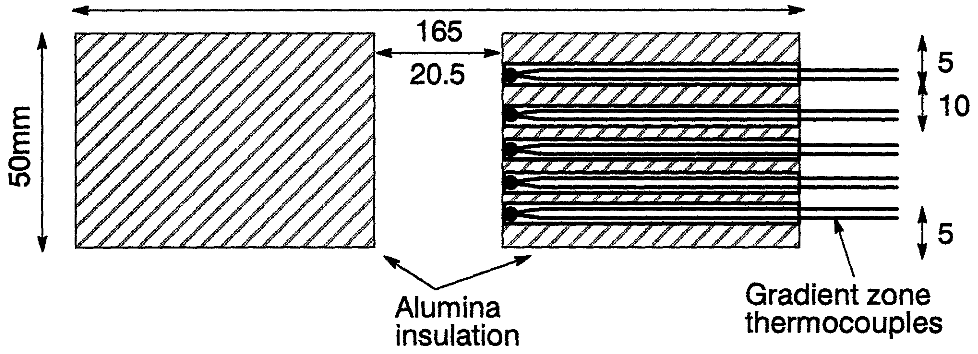

Figure **5.17** : Gradient zone fabricated only of insulating material.

the furnace was profiled in this manner, the BN rod was moved manually to four distinct locations within the gradient zone, allowed to equilibrate, and the steady-state temperatures were recorded. The results are shown in Figure 5.18,

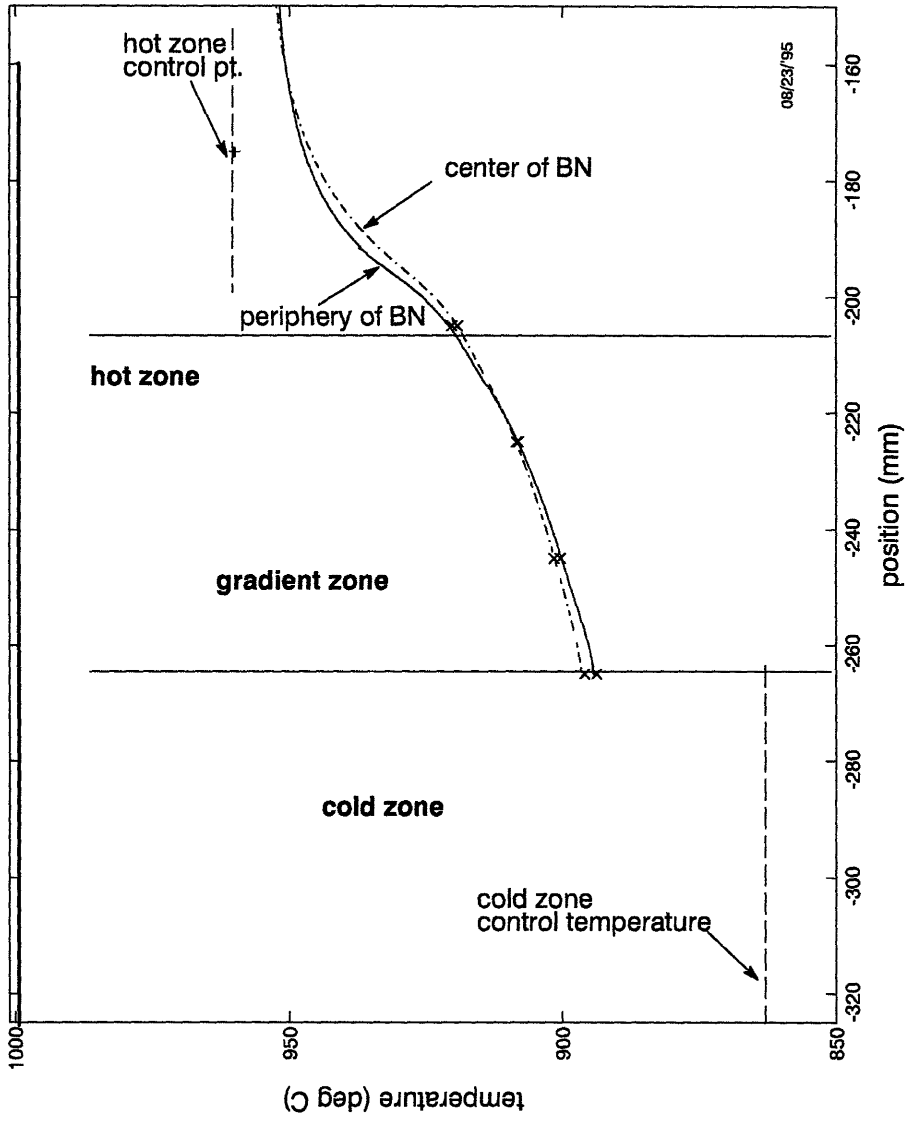

Figure **5.18** : Axial thermal profile , and radial temperature gradients, with a purely insulating gradient zone.

with the translation measurements shown by lines, and the steady-state measurements denoted by 'x' signs at the appropriate locations. It can be seen that translation at 2 cm/hr (5.55 μm/s) captures the steady-state behavior of the furnace adequately.

The radial gradients are much smaller with a fully insulating gradient zone, than with a gradient zone that has high conductivity elements. This conclusion is supported by the resistance network model that was developed (Section 5.2.2). In broad terms, the detrimental effects of inconel liners can be understood by considering that the inconel liner acts as a low resistance path for the axial flow of heat, and hence draws heat away from the charge (Figure 5.19). Such two-dimensional heat flow is the cause of increased radial gradients in the system when conductive elements are present in the gradient zone. In addition, using a lumped parameter approach, we can see that if the thermal conductivity of inconel is 100 times that of alumina, an inconel thickness of 0.4mm has roughly the same radial resistance as the 40mm radial extent of the gradient zone, and increases radial heat loss through the gradient zone.

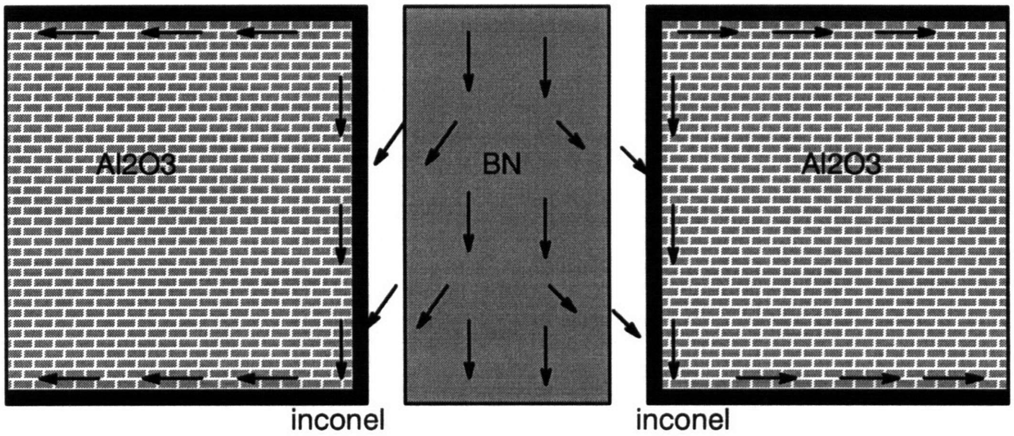

Figure **5.19** : Schematic of radial heat flows caused by inconel elements in the gradient zone.

Comparing the thermal profile in Figure 5.16 with that in Figure 5.18, we see that the flexibility in temperature profiles obtained with the use of a 'diabatic' zone (as discussed by Wang[27]) comes at the price of increased radial gradients in the gradient zone.

It must be noted that Figures 5.16 and 5.18 indicate deficiences in the operation of the lower heat-pipe. This malfunction, however, does not affect the conclusions to be reached about the detrimental influence of inconel liners surrounding the gradient zone. The defective heatpipe was replaced in later experiments.

Experiments were also conducted to verify that strong thermal coupling between the furnace and the charge was maintained even at translation rates of 3.06 cm/hr (8.5 μm/s). The thermal profiles(Figure 5.20) obtained at a translation rate of 3.06 cm/hr (8.5 μm/s) are essentially the same as those measured at a speed of 2.0 cm/hr (5.55 μm/s).

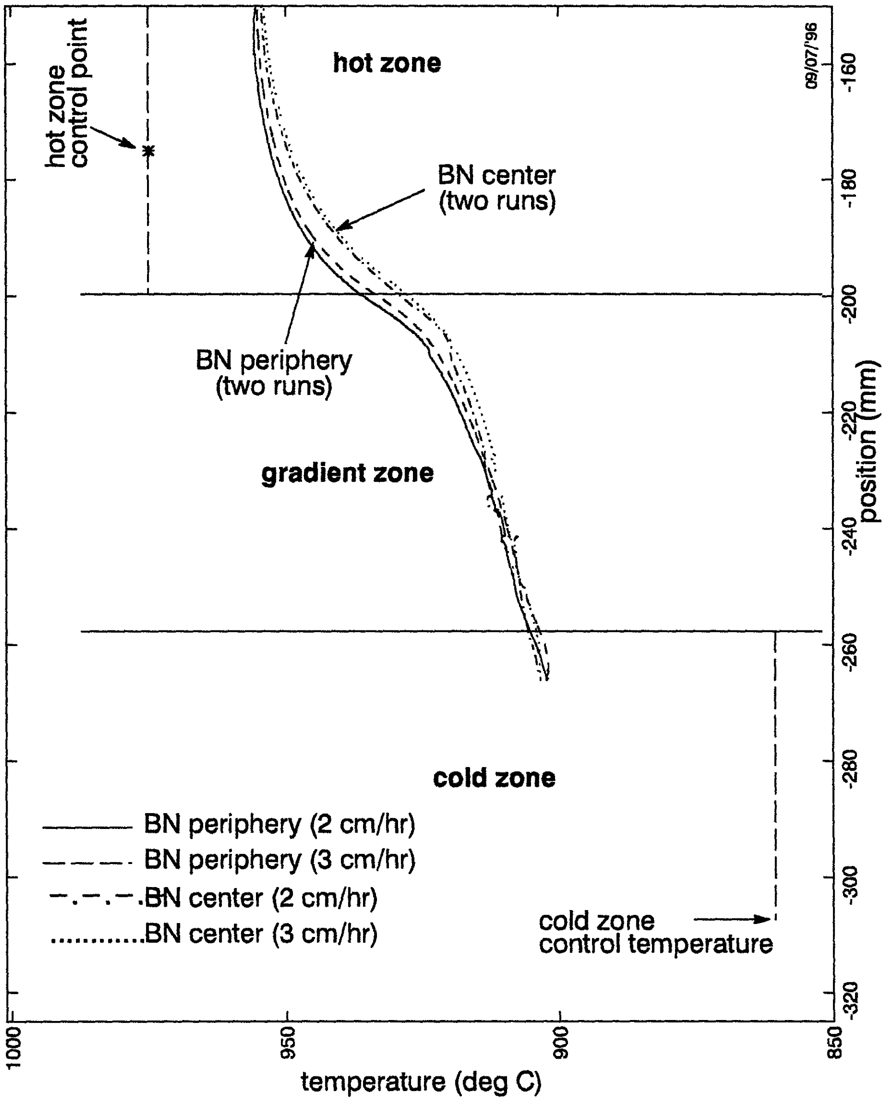

Figure **5.20** : Thermal profiles generated at different speeds of translation of BN rod.

5.2.2 Heat transfer characteristics of the system

To explain the radial gradient results obtained in the previous experiments, simplified modeling efforts were undertaken. In this context, it was necessary to measure the heat transfer coefficient between the furnace wall and the charge. An experiment was conducted where the boron nitride rod was placed such that the junctions of the thermocouples 'Cvc' and 'Cvp' were at the mid-point of the top heat-pipe. The furnace was placed under control and allowed to equilibrate at the chosen setpoint. After steady-state conditions had been achieved, the setpoint of the upper heatpipe was raised by in a step-function, and the temperature response of the charge measured.

The response of the heat-pipe and the surface of the charge to the setpoint changes are graphed in Figure 5.21(a). The heat-pipe response is found to be rapid, compared to that of the surface of the charge. In the analysis, it will therefore be assumed that the heat-pipe wall temperature (T_w) reaches steady-state instantaneously. The response of the surface of the BN rod is plotted along with the response of its center, in Figure 5.21(b), on an expanded scale. As anticipated, the periphery responds faster than the center, but the difference in rise times between the center and periphery is small enough that, to a first approximation, the region under analysis can be approximated as a body at a uniform temperature (T_c). Considering a volume of differential thickness, radius R, heat capacity C_p, and density ϱ, heat transfer out of the plane faces of this puck-shaped differential volume can be neglected, since axial gradients are low in the center of the heatpipe. Under the above assumptions, we can write:

$$\frac{d}{dt}(\pi R^2 \varrho C_p T_c) = h.2\pi R\ (T_w - T_c) \quad \textit{or:} \quad \frac{d(T_c - T_w)}{(T_c - T_w)} = \frac{2h}{R\varrho C_p} dt$$

$$\textit{integrating:} \quad (T_c - T_w)_t = (T_c - T_w)_i \exp\left(-\frac{2ht}{R\varrho C_p}\right)$$

Accordingly, at $t = \tau$, the charge temperature will have climbed to half the step and so, it appears permissible to use the measured value of τ to evaluate the heat transfer coefficient. Hence, we arrive at the following expression for the heat

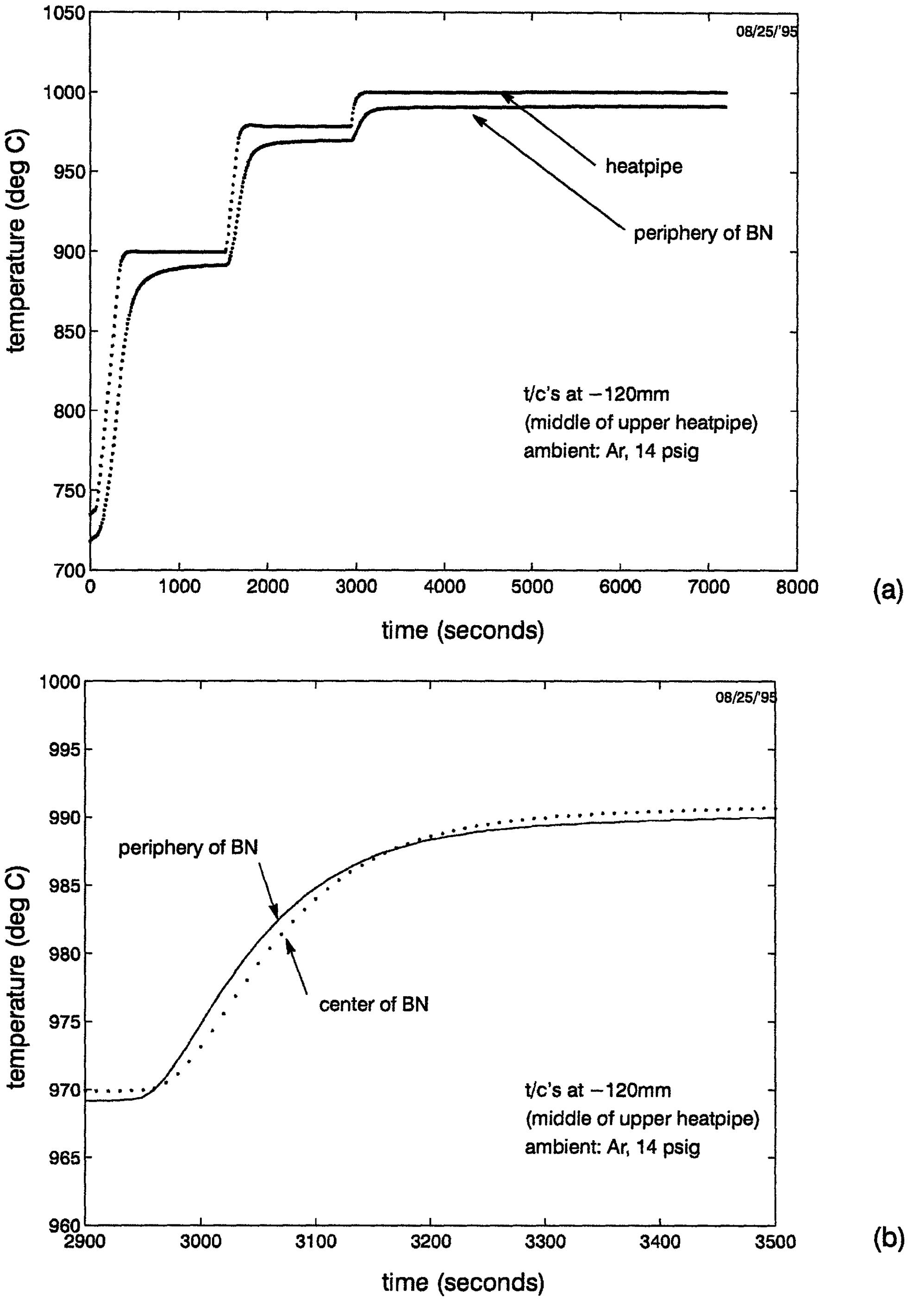

Figure **5.21** : Response of surface and center thermocouples in model (BN) charge to step changes in setpoint.

transfer coefficient between the furnace and the charge :

$$h = (R\varrho C_p)/(2\tau \ln 2) \, .$$

The data in Figure 5.21(b) gives a value of 95 seconds for τ. The value of the heat transfer coefficient, h, between the furnace wall and the charge at the operating temperature was hence estimated to be 430 W/m^{2}K. A theoretical estimate for h can be arrived at by considering radiant flux through a 1mm layer of transparent fused quartz (the furnace liner adjacent to the heat-pipe wall), followed by heat conduction and radiation through a 1mm layer of Argon gas, at 2 atmospheres pressure (thermal conductivity of the gas, K_g = 0.044 W/mK [56]). The radiative heat transfer coefficient (h_{rad}) and the conductive heat transfer coefficient (h_{cond}) are given by[57]

$$h_{rad} = 4F\sigma\left[\frac{T_f + T_c}{2}\right]^3 \qquad F = \left[\frac{1}{\varepsilon_c} + \frac{r_c^2}{r_f^2}\left(\frac{1}{\varepsilon_f} - 1\right)\right]^{-1}$$

$$h_{cond} = \frac{K_g}{r_f \ln(r_f/r_c)}$$

where σ is the Stefan-Boltzmann constant, r_c is the charge radius (8mm), r_f is the furnace radius (10 mm), T_c is the charge temperature, T_f is the furnace wall temperature ($\approx$1200 K), ε_f and ε_c are the emissivities of the furnace and the charge (black body behavior will be assumed). The theoretical estimate of the total heat-transfer coefficient is thus 400 W/m^{2}K, in good agreement with the measured value of 430 W/m^{2}K.

This data was used in developing a steady-state conduction model of heat fluxes through the charge and the gradient zone. The furnace was represented as a rectangular resistor network, with suitable voltage sources (*ie,* temperatures) applied at the nodes representing the heat-pipe walls and the outer surface of the gradient zone. HSPICE (a circuit simulator package) was used to solve for currents (*ie,* heat fluxes) and voltages (*ie,* temperatures) at various nodes. The network used is shown in Figure 5.22. Since the hot and cold zones are bounded by heat-pipes which attain isothermality within a short length (of the order of one diameter, under ideal conditions), the charge and the two heat-pipes are truncated, with no axial heat flow allowed at the top and bottom edges. Due to the assumption of axisymmetry, there is no radial heat flow across the centerline (the left edge of the

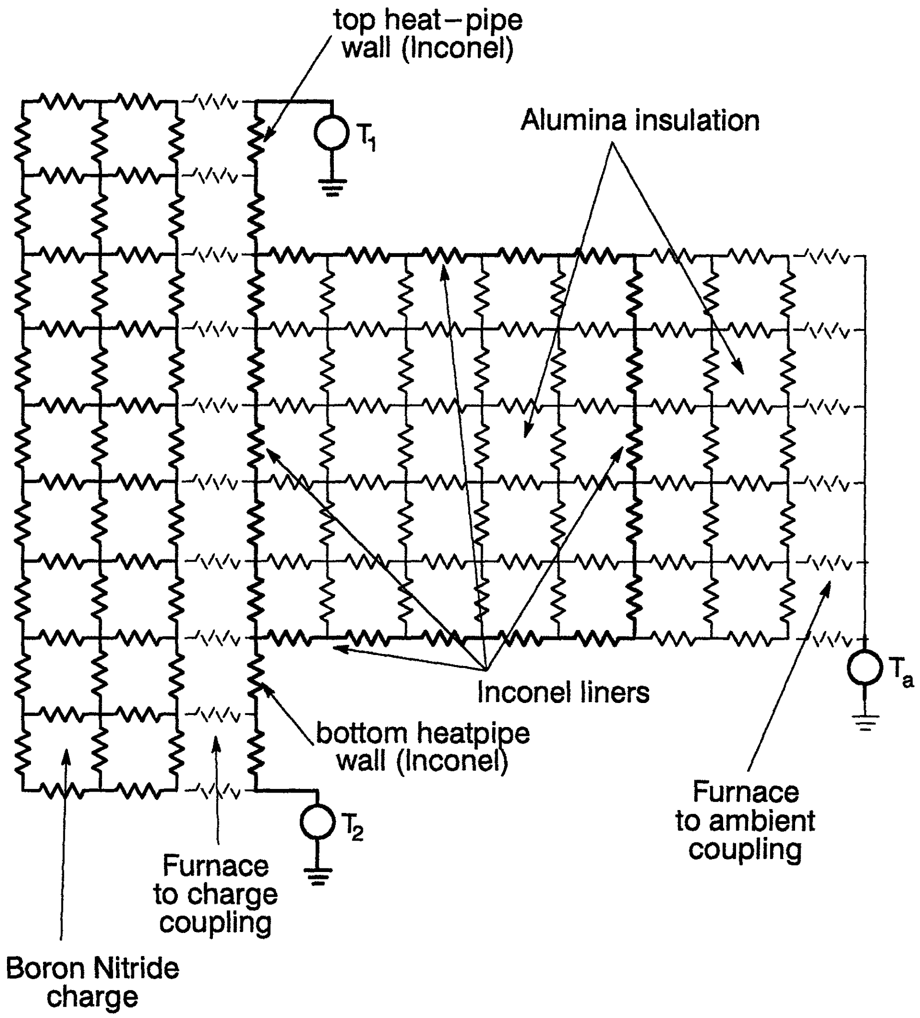

Figure 5.22 : Resistance network model of the charge, the heat-pipes and the gradient zone, and coupling through gas.

model). Finally, the inconel flanges of the heat-pipes are represented, but they are shown to allow heat transfer only along their length, and not to the ambient. This is definitely not true, since the flanges will pull some heat from the insulation at smaller radii, and thereby contribute to greater heat leakage than allowed by this model. However such an assumption simplifies the model considerably, and results in conservative estimates of radial heat loss.

The resistances (R) representing the coupling between the charge and the furnace were calculated from the heat transfer coefficient, h, using the relation, $R=1/(2\pi R_w h\Delta)$, where R_w is the radius of the furnace wall, and Δ is the length of furnace represented by the particular resistance element. The radial resistances in the conductive elements (the charge, the insulation of the gradient zone, and the inconel liners) were computed according to the relationship, $R=1/(2\pi rK\Delta / t_r)$, where r is the geometric mean radius of the annular conductive element being considered. t_r is the element thickness along the radius; and Δ is the element width along the length of the furnace. The discretization of the outer insulation, surrounding the outer inconel liner, is coarse in the radial direction, when compared to the discretization in the inner insulation. This simplifies the model, without compromising the heat flux computations in the charge and the core of the furnace. In the axial direction, the resistances were computed using $R = 1/((2\pi rt_rK/\Delta)$. The thermal conductivity of inconel changes from 24.4 W/mK at 800°C to 27.8 W/mK at 1000°C [58]. However, a constant value of 25 W/mK was used in this model. The thermal conductivity of BN is anisotropic (Table 5.1), with higher conductivity in the axial direction. In this simulation, an intermediate value of 23 W/mK was used. The thermal conductivity of the alumina insulation was 0.14 W/mK.

The results of the simulations confirm that the use of inconel liners causes non−zero temperature gradients to extend into the hot and cold zones. Axial temperature profiles (along the furnace wall) were calculated for three nominal gradient conditions : hot zone at 900°C, 950°C and 1000°C, with the cold zone held at 850°C. These three gradient conditions were tested using (a) a gradient zone configuration that had inconel liners aon all sides, and (b) a gradient zone fabricated entirely of fibrous alumina. When the gradient zone is fabricated entirely of alumina insulation, the isothermality of the hot and cold zone is noticeably improved (Figure 5.23). It can also be seen that the model captures the relatively higher sensitivity of axial temperature gradients the top zone to the gradient zone configuration, when compared with the bottom zone. Such a difference was also

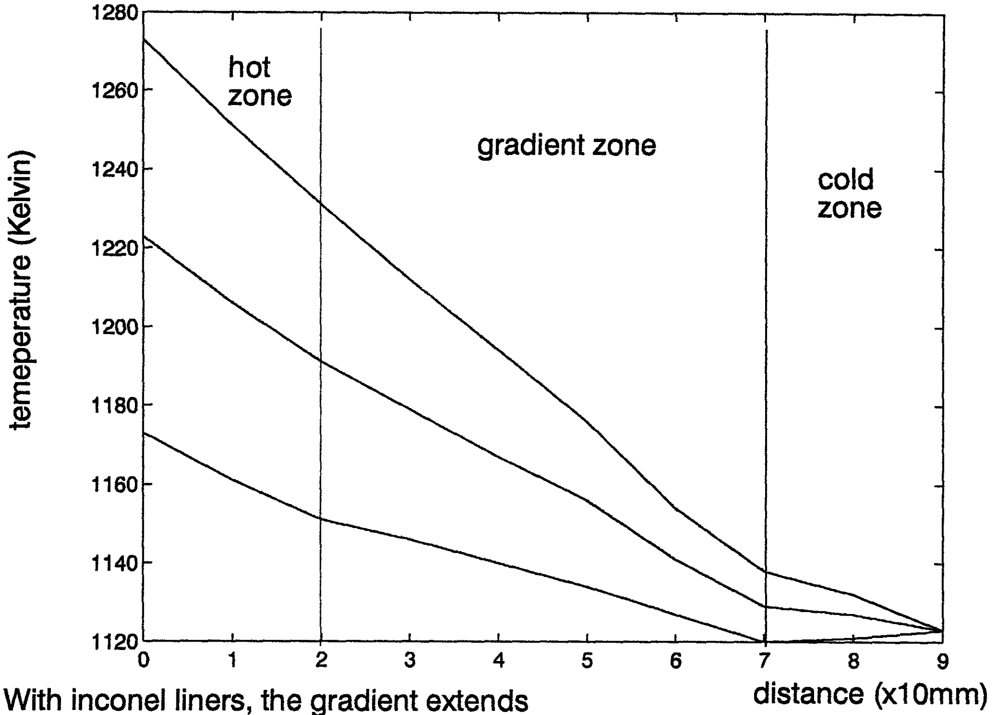

(a) With inconel liners, the gradient extends into the hot zone.

(b) Without inconel in the gradient zone, the profiles in the hot and the cold zones are flatter.

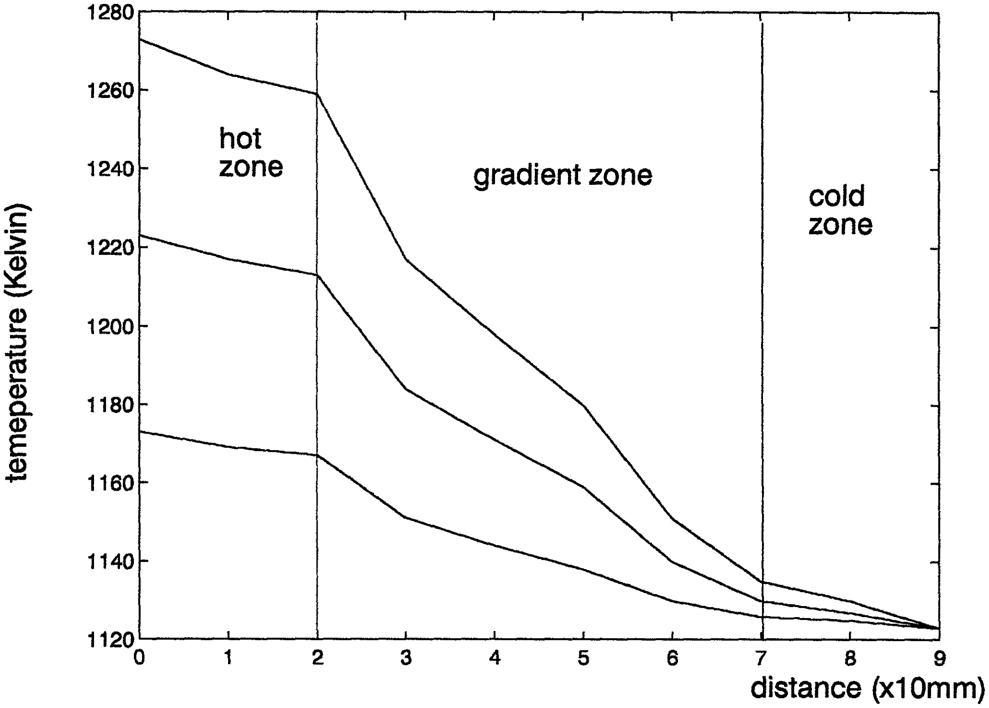

Figure **5.23** : Simulation results (with and without inconel liners).

seen in the experimental data. Aymmetry caused by the fact the hot zone is operating at a higher power rating (thereby being a bigger source of heat in the system) make the hot zone more sensitive to parasitic heat flows. The asymmetry introduced by the gravity vector would change the natural convection heat transfer on the outer wall of the gradient zone, as a function of axial position. In this model, however, such an effect is not modeled. So it should be expected that a real system would have an additional contribution from the variation of the Nusselt number along the outer wall of the gradient zone.

5.2.3 Axial temperature profile for a nominally low axial temperature gradient.

The experiments to be described below were the first indicator of the importance of further reducing the thermal conductivity of the gradient zone insulation. In conventional furnace configurations, axial temperature gradients are chosen to provide for high enough axial heat fluxes to allow the unavoidable radial heat 'leakage' through the gradient zone insulation to be neglected. Another technique used to counter the non-zero thermal conductivity of gradient zone material is to reduce its height. This approach has the disadvantage[13] that interface shape control is reduced. Sukanek[24] developed analytic expressions to show that, while interface planarity improves with a longer zone, growth rate control gets degraded, in a conventional vertical Bridgman-Stockbarger furnace. In this thesis work, a modification to the nature of interface velocity control is being introduced. The length of the gradient zone was therefore increased to the extent required, to maximize the interface shape control, without loss of control over the microscopic rate of growth.

For operation of a furnace with a gradient zone aspect ratio greater than 1, the thermal conductivity of insulation material employed in the gradient zone becomes a primary issue. This is particularly important at low axial gradients, since the radial heat losses in the gradient zone increase in relative importance. This is illustrated in Figure 5.24. The axial profile shown here was obtained with a gradient

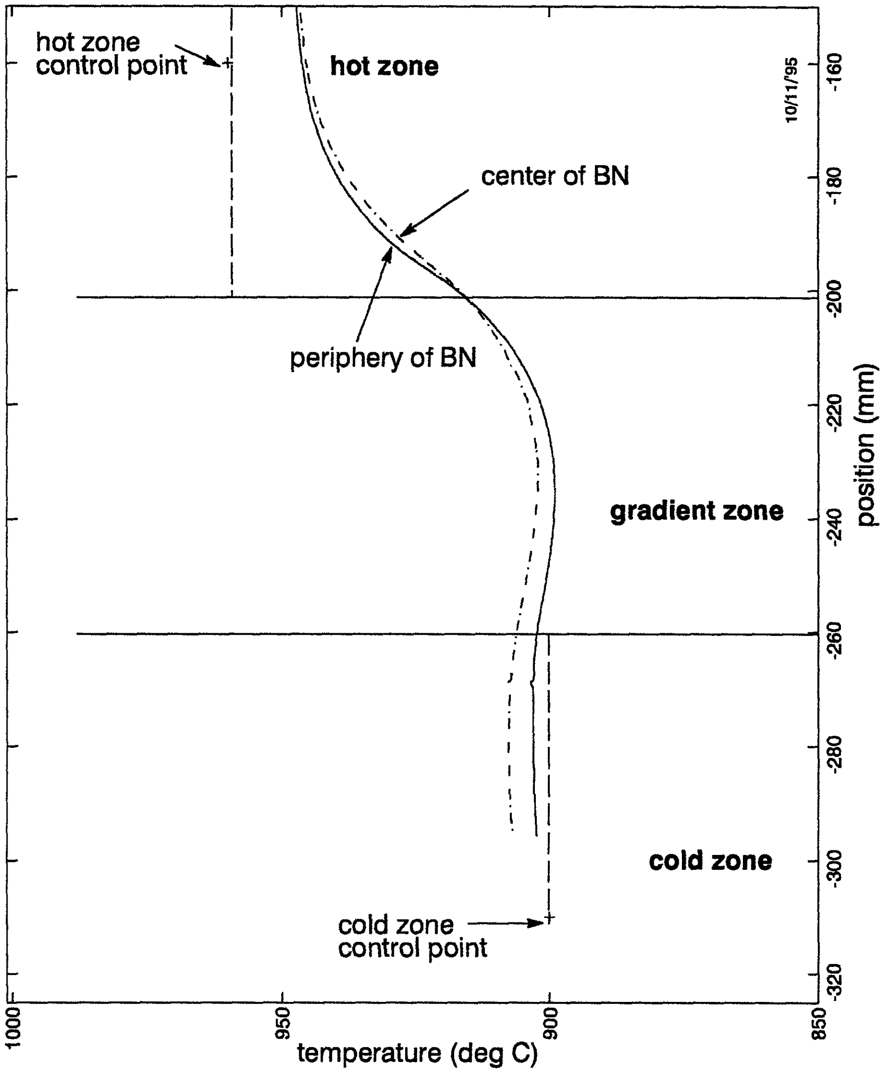

Figure 5.24 : Thermal profile with a low nominal axial temperature gradient

zone constructed of alumina (Types ALC and AL-30, Zircar Products, Inc.) of thermal conductivity 0.14 W/mK, around a 1.4mm thick fused quartz inner liner. The axial profile shows a 'dip' in the gradient zone due to heat losses through the gradient zone.

The radial temperature distribution in the gradient zone insulation package was measured, operating the furnace in air, the steel enclosure removed. This changed the magnitude of the heat transfer coefficient at the outer surface of the insulation package since the furnace was usually operated in inert gas at 2 atmospheres pressure. However, due to the large diameter (110mm) of the gradient insulation, it is thought that the temperature gradient at the center of the insulation would only be minimally affected by a change in the convective heat transfer on the outer surface. A inconel-sheathed, insulated type K thermocouple, of diameter 1.58mm was withdrawn through a recrystallized Alumina tube in steps of 10 mm to obtain the radial temperature gradients, at a height of 10 mm above the lower end of the 60mm-thick insulation package. (Figure 5.25). The radial temperature gradient across the gradient zone is about 50°C/cm. The data also shows the expected two-dimensional nature of heat flow in the gradient zone. If the heat flux were only in the radial direction, the temperature distribution would exhibit a concave profile, with the temperature decreasing as $1/r^2$. However, the measured profile shows an inflection point roughly halfway through the gradient zone. The convexity of the temperature profile closer to the furnace wall indicates that axial

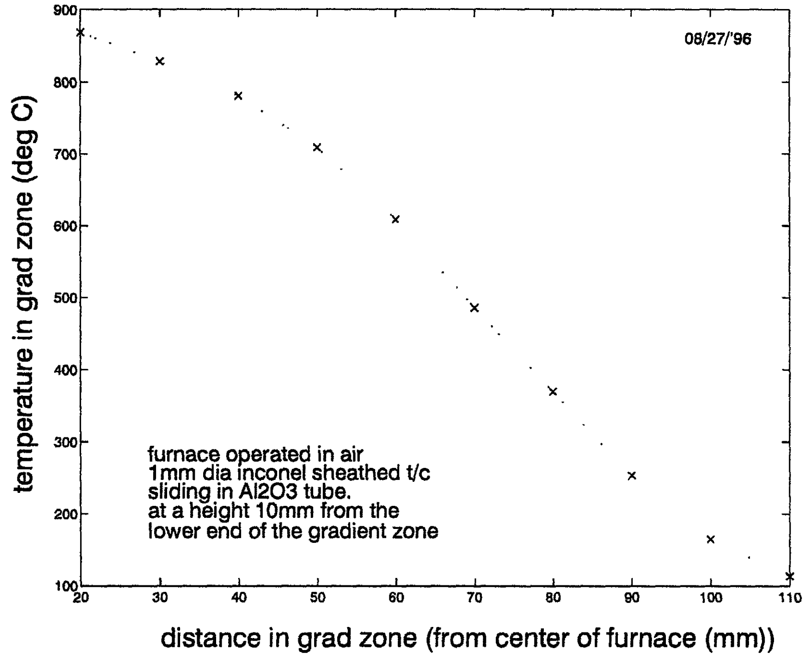

Figure **5.25** : Radial temperature gradient across the gradient zone heat flow through the gradient zone needs to be taken into account just as much as the radial heat flux out of the gradient zone.

The axial heat flow through the boron nitride charge at the boundary between the hot zone and the gradient zone is given by $K.\pi r^2(dT/dx)$, where dT/dx is the axial temperature gradient, K is the thermal conductivity of BN (39 W/mK). For an axial temperature gradient of 10°C/cm, the flux is $39.\pi.\ 0.016^2.\ (1000) = 31$ watts. Data from Figure 5.25 can be used to *estimate* radial temperature gradients at the inner wall of the insulation package. The radial heat loss through a 5mm thickness of insulation is $K.2\pi.r_w.h.(dT/dr) \approx 0.14 \times 2\pi \times 0.2 \times 0.005 \times 5000 = 4.3$ watts. The radial heat loss is thus likely as much as 15% of axial heat flow, even with the lowest conductivity insulation that could be used in the gradient zone.

The experimental results provide strong arguments for designing a gradient zone with the lowest possible thermal conductivity. A possible approach[54] to this end would be to use vacuum. This is further discussed in the concluding chapter, under 'Suggestions For Future Work'.

5.2.4 Influence of heater location on axial thermal profiles

When the heat-pipe was first incorporated into this Bridgman-Stockbarger furnace, it was felt that the location of the heater ought not to matter. This idea arises from the thought that : the high thermal conductivity of the heat-pipe would 'isothermalize' the hot and the cold zones no matter where the heater was placed. However, as is discussed by Mills[46] and Bienert[47], there are (i) limits to the heat flux that can be supported by a heat-pipe; (ii) it is only the inner wall of the heat-pipe that is truly isothermal, and if there are excessive heat losses in any portion of the heat-pipe, larger temperature gradients will be needed across the wall of the heat-pipe, thereby destroying the isothermality of the cavity wall; and (iii) these effects are naturally accentuated at the ends of the annular heat-pipe. Due to these constraints, it is clear that more attention has to be paid not only to the total heat flux throught the heat pipe, but also to the flux distribution over the heat-pipe surface. In Figure 5.26, the top heater is held away from the gradient zone by a 25mm-thick alumina support block. The resulting thermal profile (Figure 5.27) shows that significant radial and axial temperature gradients are present at the charge periphery at the bottom of the upper heat-pipe. (The large difference between the charge periphery temperature and the lower heat-pipe temperature is due to the fact that the thermocouple passed very close to the heater, and hence read an erroneously high temperature - this failing was fixed in the subsequent experiment). In the next experiment, the heater support block was removed, and the heater allowed to rest on the gradient zone. With the heater directly on top of gradient zone, the measured thermal profile (Figure 5.28) was better, in that the temperature was more uniform in the heat-pipes, and in that the gradients were primarily localized to the gradient zone.

The results of this pair of experiments confirm that heat loss into the gradient zone cannot be neglected even with low thermal conductivity alumina insulation. Secondly, this set of experiments points out the fact that the incorporation of heat-pipes in vertical Bridgman furnaces has to be done with care. Care should be taken to minimize heat losses from the heat-pipe, particularly at the ends, since it degrades the isothermality of the heat-pipe (and even possibly the axisymmetry). The attainment of isothermality and axisymmetry is the *raison d'etre* for the use of heat-pipes in Bridgman furnaces.

5.2.5 Temperature excursions within the gradient zone

Six thermocouples (X, A,B,C,D, and E) were positioned to measure the temperature along the inner wall of the gradient zone (Figure 5.26). During profiling runs the BN charge was translated down through the furnace cavity, and any four of the six gradient zone thermocouples could be monitored.

During thermal profiling experiments, the temperature of the hot zone (as measured by thermocouple Z1) and of the cold zone (measured by thermocouple Z0) were maintained within 0.25°C of their respective setpoints by the control

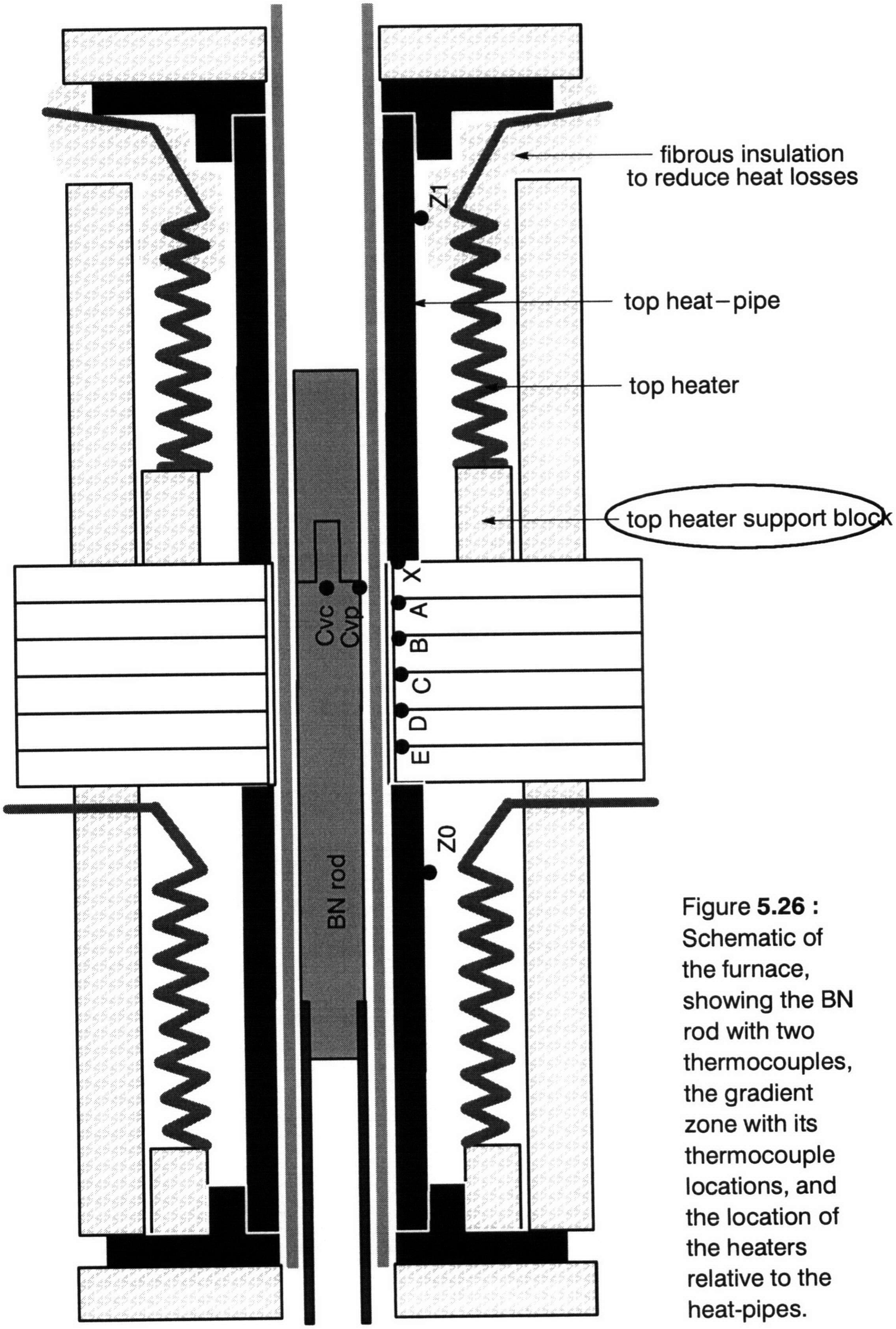

Figure **5.26 :** Schematic of the furnace, showing the BN rod with two thermocouples, the gradient zone with its thermocouple locations, and the location of the heaters relative to the heat-pipes.

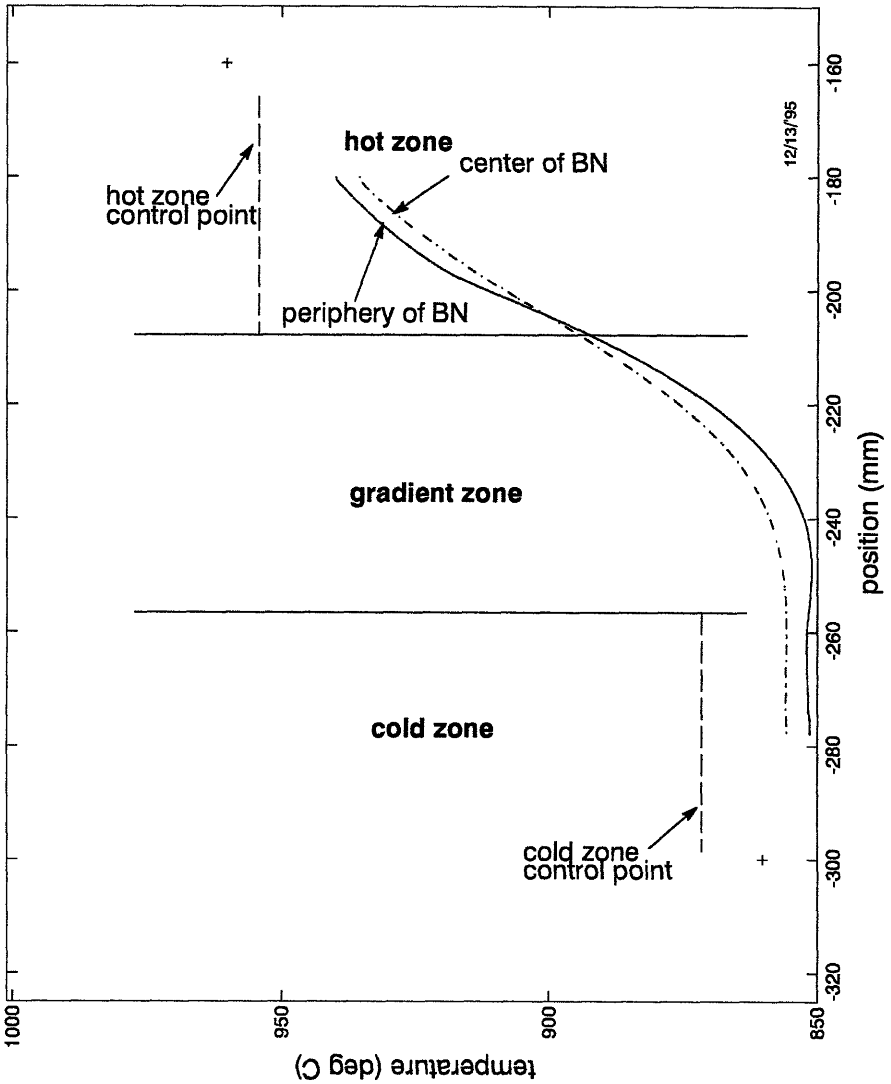

Figure **5.27** : Axial profile with the top zone heater located 25mm above the top of the gradient zone. (cf: Figure 5.28)

program. It was noticed that, during translation of the BN dummy charge (Figure 5.12(a,b)), the gradient zone thermocouples exhibited reproducible temperature excursions (Figure 5.29). A similar effect, with even more pronounced excursions was observed when a shorter BN rod was used as the translating charge (Figure 5.30). It should be noted that the first dip in each thermocouple record correlates with the motion of the (a)-(b) junction in the BN rod across the location of the respective thermocouple. The second observed dip coincides with

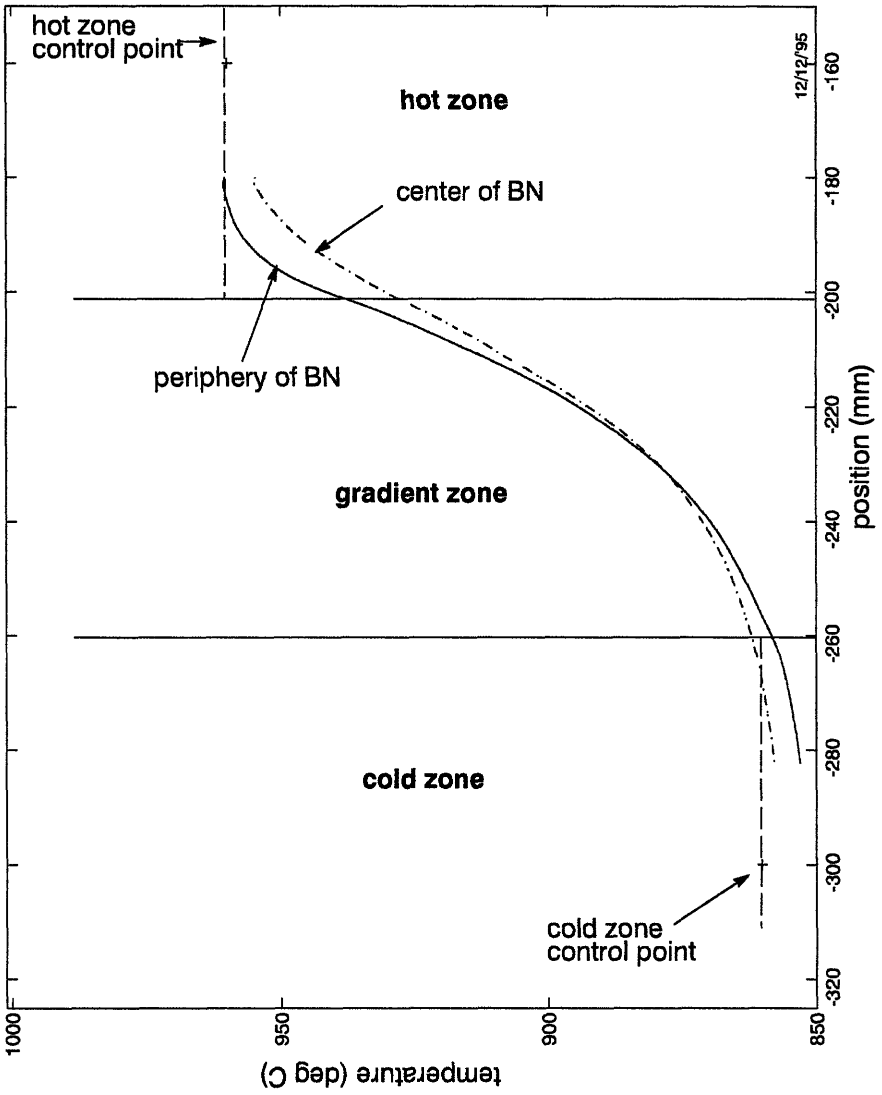

Figure **5.28** : Axial profile with the top zone heater located directly on top of the gradient zone. (cf: Figure 5.27)

the motion of the end of the BN rod across the same location in the gradient zone. (It should be mentioned that in the second experiment (with a shorter BN rod), a displacement rate of 3 cm/hr rather than 2 cm/hr used, and helium rather than argon was used.

These results although unexplained in detail suggest transient effects related to short charge lengths. Though the hot and cold zones track the setpoint accurately, the local thermal field in the gradient zone (where the crystal-melt

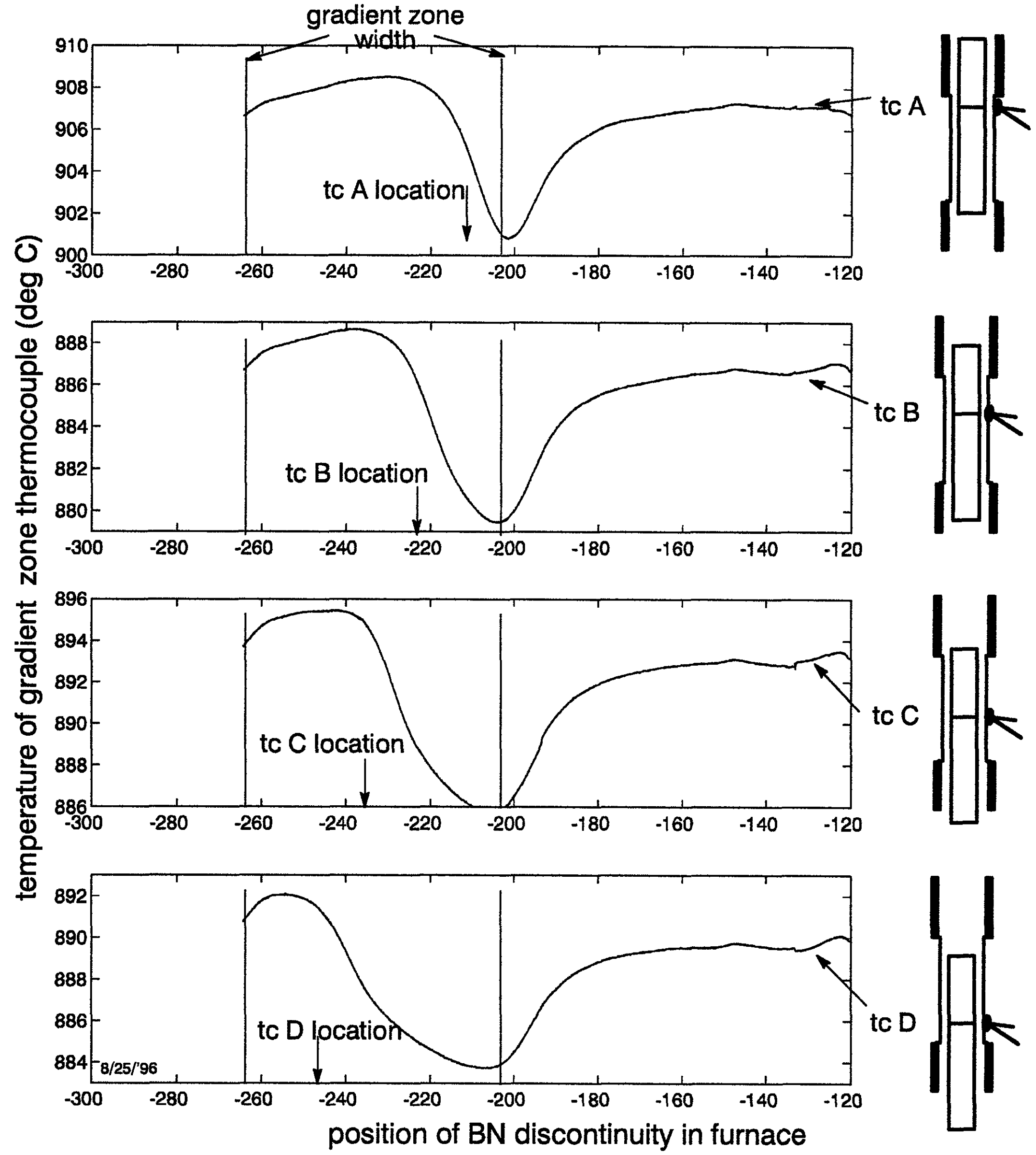

Figure **5.29** : Records of the gradient zone thermocouples during translation of the longer BN charge.

interface would be located) undergoes considerable changes during crystal growth.

5.2.6 Temperature measurement within the gradient zone

In the Bridgman mode of operation of the growth system, the control sensors for the hot and cold zones are moved into the gradient zone from their

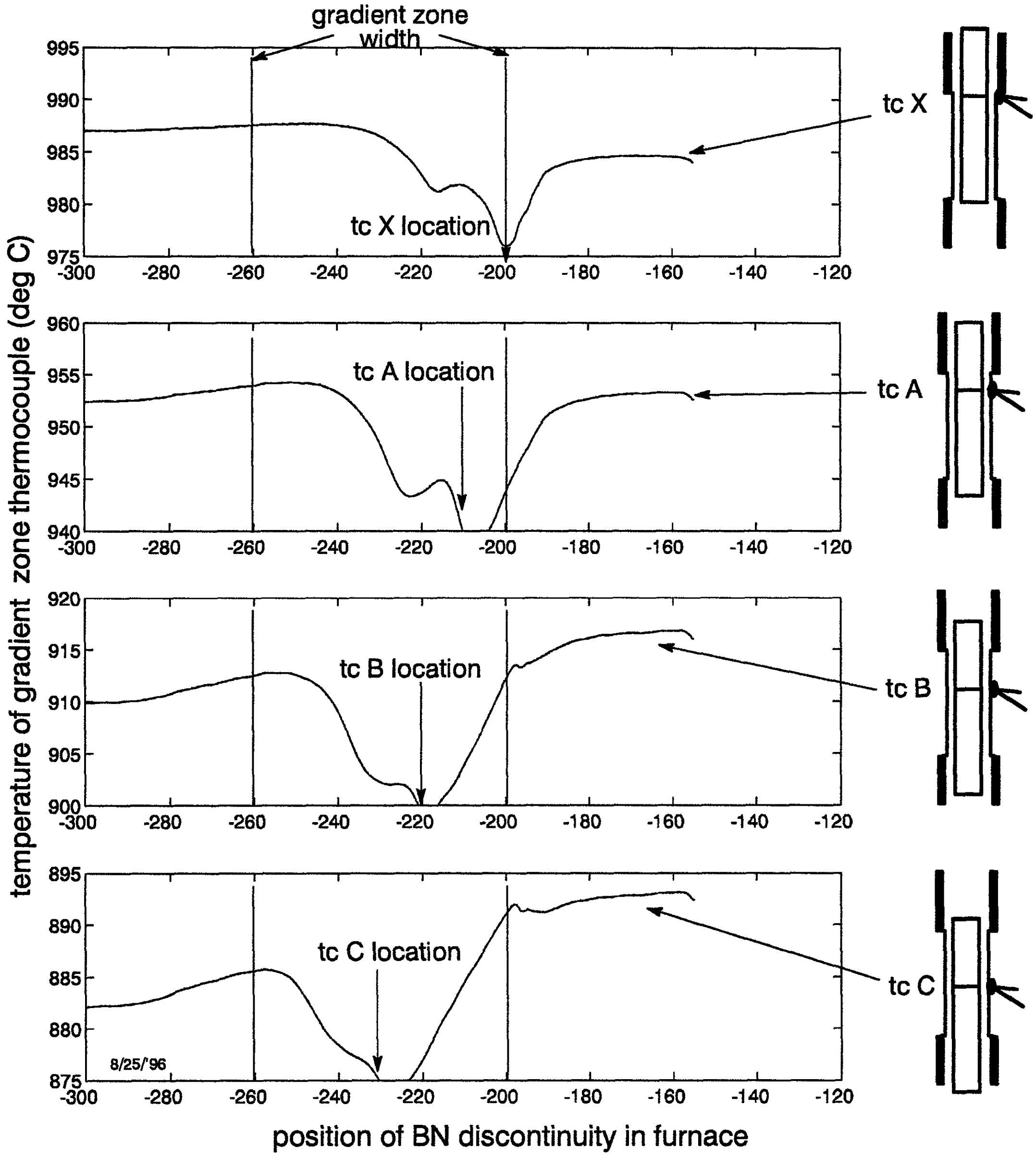

Figure **5.30** : Records of the gradient zone thermocouples during translation of the shorter BN charge.

conventional positions in the hot and cold zones (Figure 5.2). In order to control the interface location in the charge to the desired accuracy, it is necessary that these sensors measure the charge temperature at their location as accurately as possible.

The BN rod used as a dummy charge and profiling tool has a thermocouple 'Cvc' located at its axis, and thermocouple 'Cvp' at its periphery

(Figure 5.26). The experiments are designed to establish the relationship between the temperature recorded by the peripheral thermocouple (Cvp) of the BN rod and that recorded by the gradient zone thermocouple, when translation of the BN rod brings thermocouple 'Cvp' to the location corresponding to one of the gradient zone thermocouples (X,A,B,C,D, or E). A small difference between the readings of the two sensors is expected to exist reflecting the radial gradients across the helium gap (1mm) and the quartz liner (1mm) that separate the two sensors. Hence, for the control configuration under consideration (the 'Bridgman mode of operation'), it is expected that the charge surface temperature is accurately measured, and the interface location thereby fixed, *a priori.*

In preliminary experiments, it was found that the temperatures recorded by the gradient zone thermocouples (D,C,B, and A) were tens of degrees below those measured by the peripheral thermocouple in the BN rod, even though the thermocouples were sensing the temperature at points only 2mm apart. In this experiment, the gradient zone thermocouples extended radially out from the furnace liner, as shown in Figure 5.26, and Figure 5.31(a).

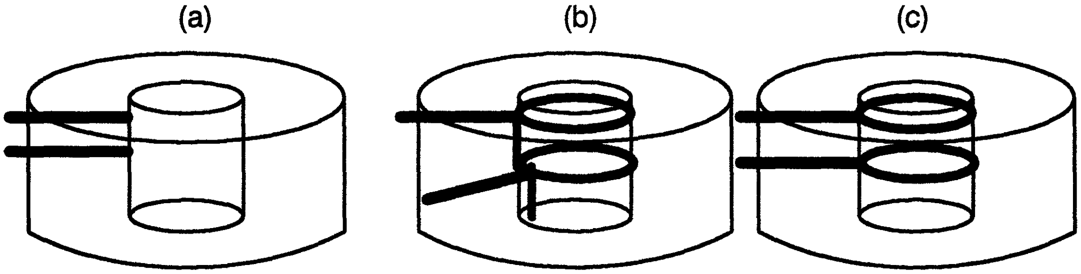

Figure **5.31** : Geometric configuration of gradient zone thermocouples

The apparent discrepancy in measured temperatures was tentatively attributed to heat loss along the thermocouples, since the temperature gradient in the radial direction of the gradient zone is, by design, quite large (Figure 5.25). Considering that the sheathed thermocouples used were only1.58mm in diameter, a further reduction in thermocouple size was not considered a viable solution. Hence, the way in which the gradient zone thermocouples were introduced into the gradient zone was changed. Rather than being introduced along a radial line, they were introduced from the top of the zone (Figure 5.31(b)). A loop was used to reduce the impact, on the junction temperature, of the parasitic heat flow along the thermocouple length in the gradient zone. With the hot zone at 1000°C and the cold zone at 860°C, the temperatures measured by the gradient zone sensors matched the temperature measured by the peripheral thermocouple in the BN rod to within 10°C (all but one were in fact within 2°C) . The range of temperatures recorded by the thermocouples is indicated by a vertical line, with an 'x' marking the temperature recorded at the instant the profiling thermocouple, 'Cvp' was closest (Figure 5.32). When the axial gradient was increased, however, with the hot zone at 1000°C, cold zone at 750°C, *ceteris paribus*, the gradient zone sensors consistently reported a higher temperatures (Figure 5.33).

Hubert *et al*[55] analyzed a similar thermal situation, though not one as severe with respect to the magnitude of the thermal gradients involved. They used finite element simulations to pin down the source of the discrepancy between the measured and actual temperatures as being heat conduction along the body of the thermocouple. It is hence considered necessary, for accurate measurement of the temperature at the wall of the gradient zone, to ensure that the temperature gradient along the thermocouple near its junction is negligible. This was accomplished by using a design where each thermocouple was looped several times, at the same height and radial position as its junction (Figure 5.31(c)). As a result, charge surface temperatures as recorded by sensor 'Cvp' were matched by the gradient zone sensors (to within 5°C, which is well within the accuracy of Type K thermocouples at the high temperatures involved).

5.3 Control of the furnace with gradient zone thermocouples

Tests were conducted to demonstrate the controllability of the process in the 'Bridgman mode of operation' using control sensors located in the gradient zone, and a boron nitride dummy charge.

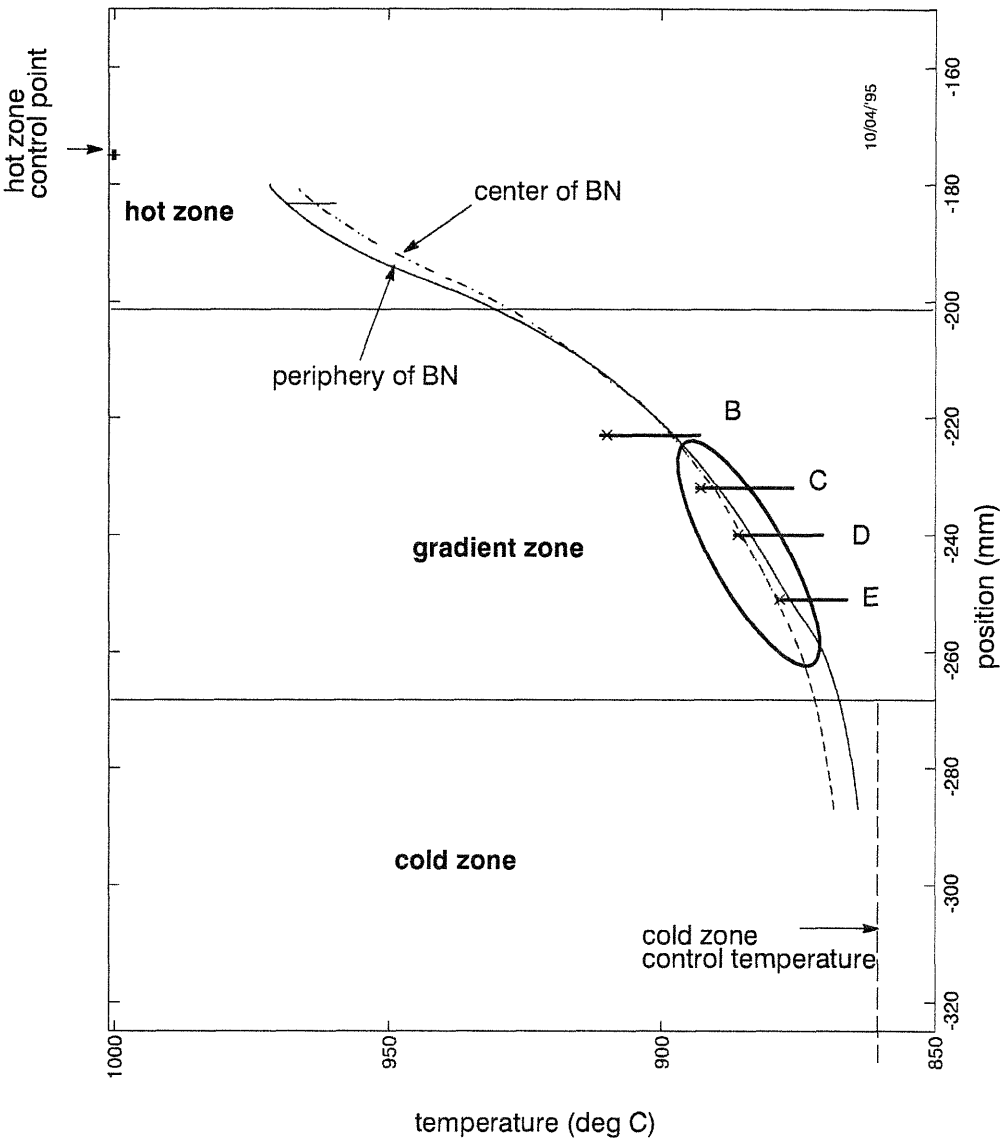

Figure **5.32** : Fortuitous temperature agreement, with insertion of gradient zone sensors as in Figure 5.31(b).

5.3.1 Control using one gradient zone thermocouple

In this experiment, the cold (lower) zone of the furnace was controlled using gradient zone sensor B, while the hot zone was controlled using sensor Z1 in the heat-pipe (Figure 5.26). With the furnace being controlled in this manner, the interface location is fixed, since the power input to the lower heater is adjusted to maintain the melting point isotherm at the sensor location. The axial temperature

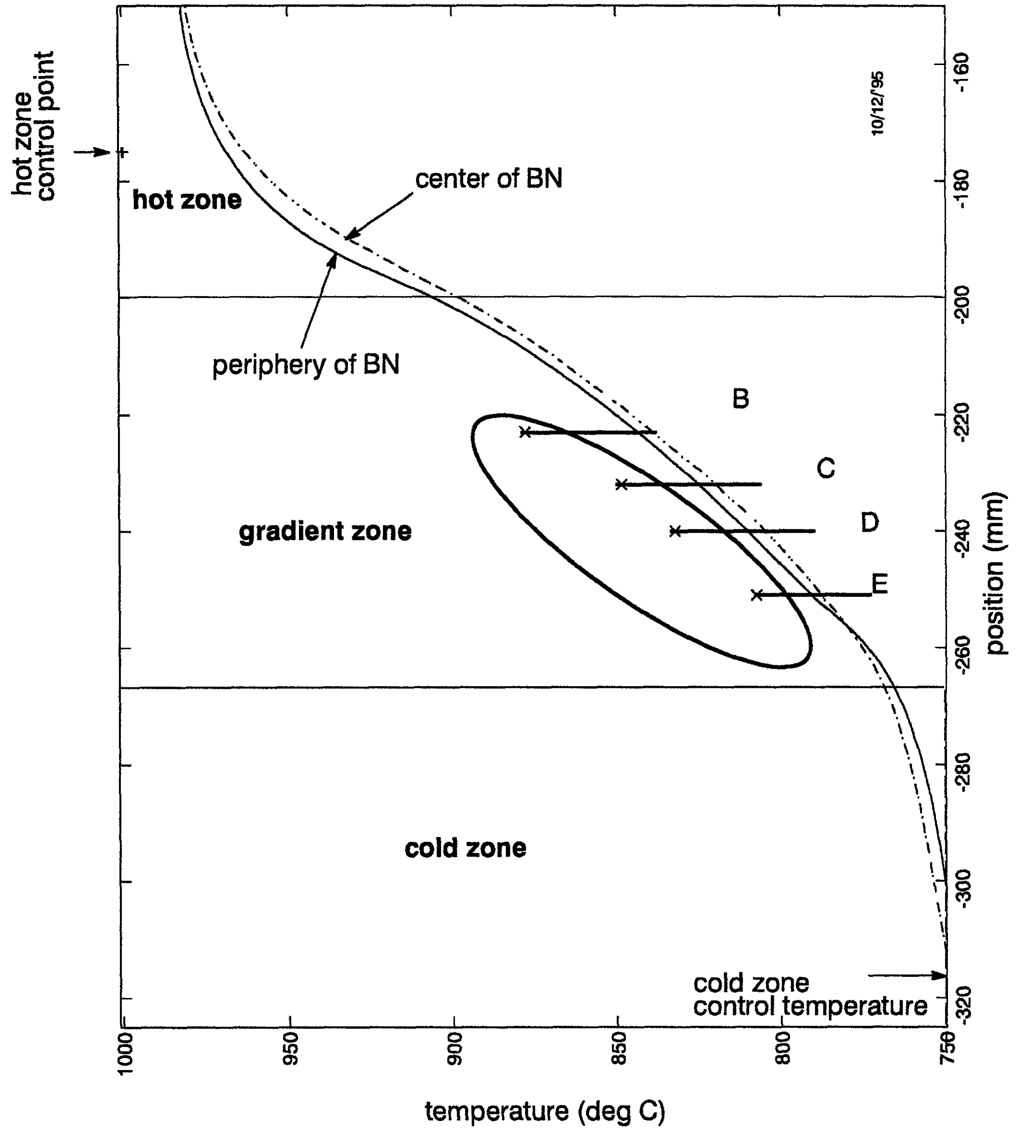

Figure 5.33 : Temperature discrepancy with insertion of gradient zone sensors as in Figure 5.31(b), at higher axial temperature gradients

gradient at the interface can vary, however, due to the decreasing length of charge in the hot zone (decreasing thermal coupling).

The control parameters were established through a tuning procedure. The values utilized were : (a) for control of the bottom zone, using sensor B : $K_p = 0.06$, $T_i/T_s = 400$, $T_d/T_s = 100$, and antiwindup = 5 °C ; (b) for control of the top zone using sensor Z1 : $K_p = 0.25$, $T_i/T_s = 100000.0$, and $T_d/T_s = 0$. The equations on page 77 describe how these parameters are utilized by the program to effect control. The rod was translated downwards at a constant rate of 3.06 cm/hr (8.5 μm/s), with the furnace backfilled with Helium at 14 psig. Sensor B was controlled at 900°C, while sensor Z1 (in the top heat pipe) was maintained at 1000°C. The temperatures recorded by the thermocouples in the BN rod (Cvc and Cvp) as they were translated down the furnace cavity are shown by thin lines (Figure 5.34). The

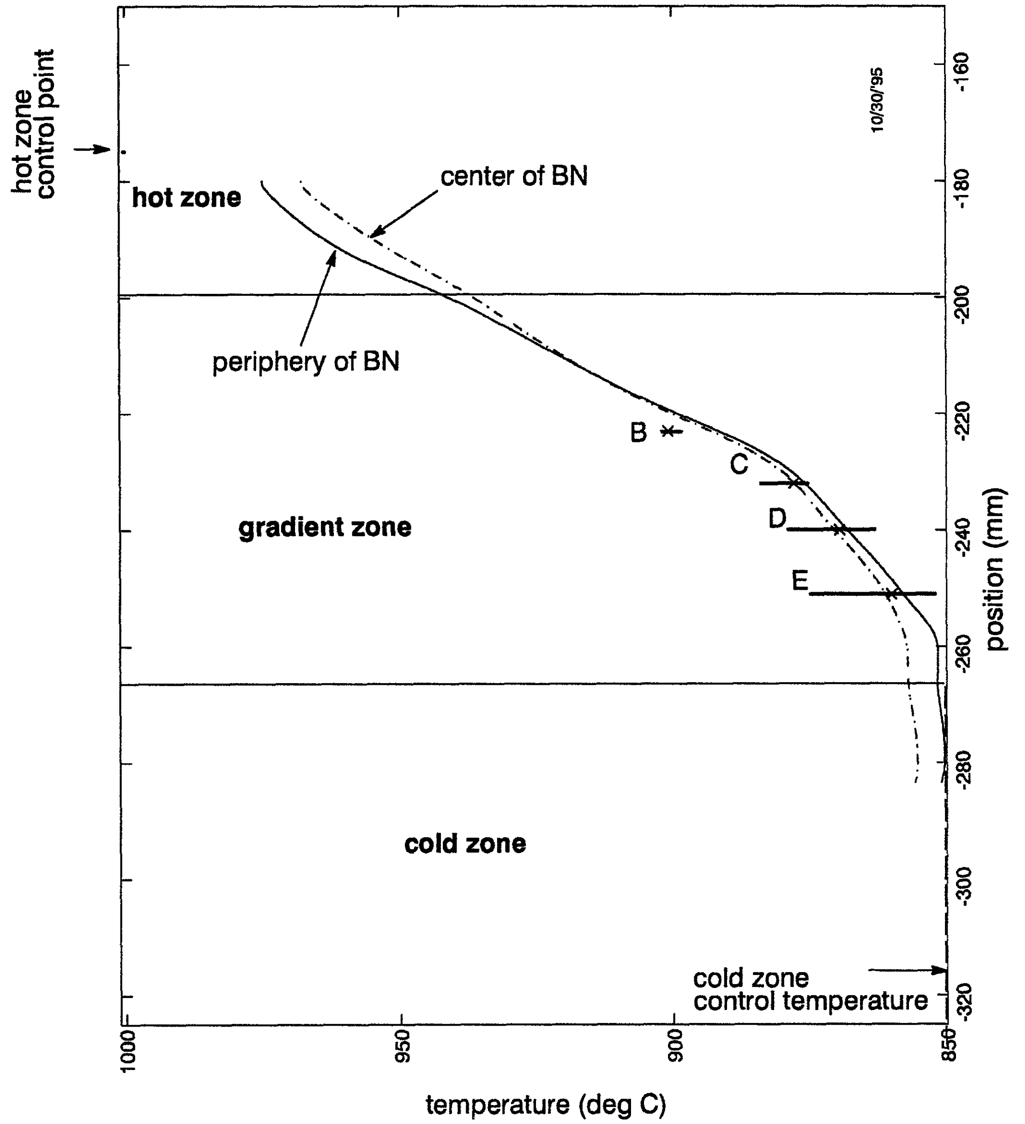

Figure 5.34 : Control using one gradient zone sensor and a sensor in the heat-pipe.

variation of the gradient zone thermocouples at their specific location is represented by a thick vertical line. The 'x' marks the temperature recorded by the sensor at the instant when thermocouples Cvc and Cvp cross the location of that sensor. Running averages of power drawn by the two heaters show that the lower heater, which is controlled by gradient zone sensor B, makes compensatory power changes. The upper heater is not driven to make such power changes since it is controlled by the sensor Z1 located in the heat-pipe. (Figure 5.35).

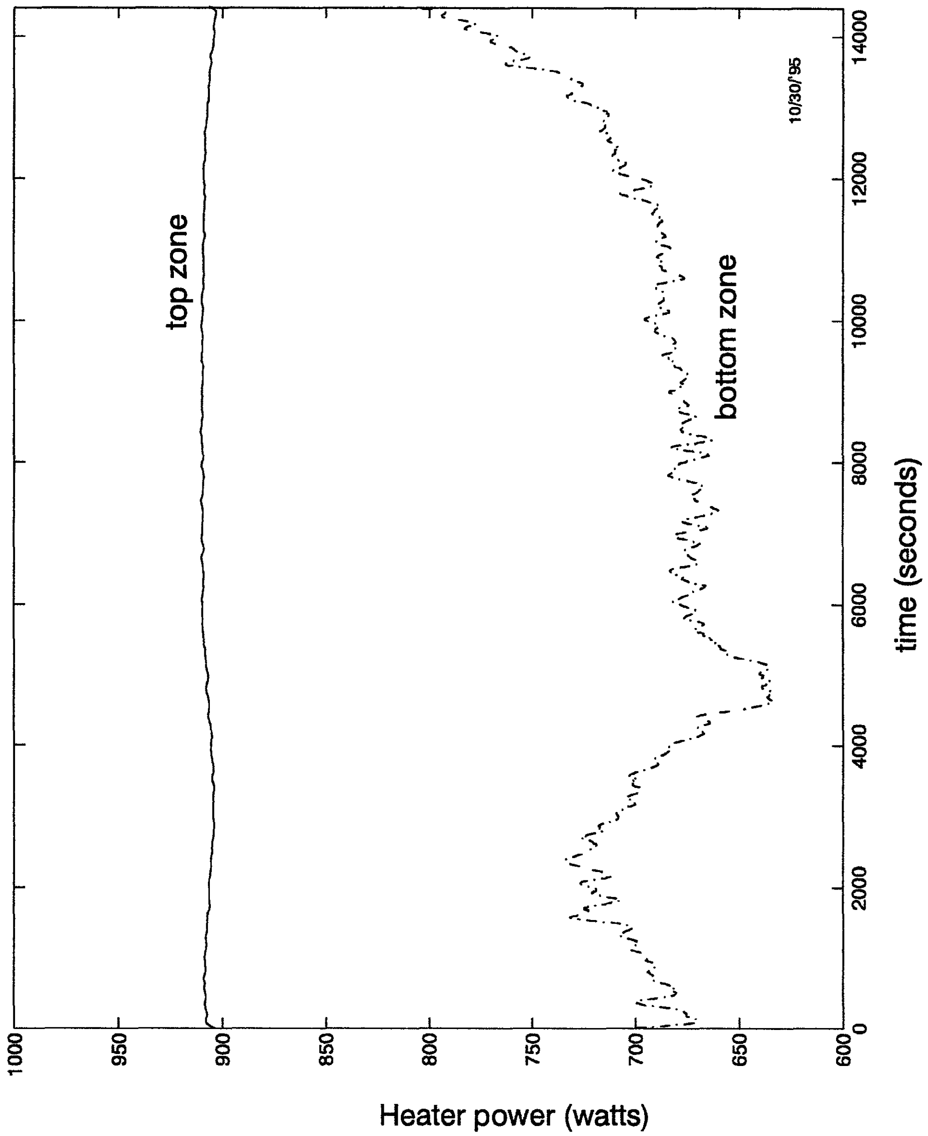

Figure **5.35** : Power requirements of the two zones, for control using one gradient zone sensor, in Bridgman mode

5.3.2 Control with two widely spaced sensors

The furnace was controlled using sensors B and E (Figure 5.26), both of which are in the gradient zone, separated by 2 cm. The PID parameters used were (a) for control of the top heater using sensor B : $K_p = 0.08$, $T_i/T_s = 500$, $T_d/T_s = 80$, and antiwindup = 5°C; (b) for control of the bottom heater using sensor E : $K_p = 0.05$, $T_i/T_s = 500$, and antiwindup = 5°C. The dummy charge of boron nitride was translated downwards at 1.98 cm/hr (5.5 μm/s). The furnace ambient was helium at 14 psig pressure, with a small flow rate maintained through a bubbler.

The control sensors B and E were maintained at temperatures within 0.25°C of their respective setpoints. The power drawn by the two heaters varies to compensate for the changes in thermal coupling caused by charge translation (Figure 5.36). This results is considerable variation in the heat-pipe temperatures, shown by the thick vertical lines marked Z0 and Z1 in Figure 5.37. It can also be seen in Figure 5.37 that though sensors B and E are held at the setpoints, the thermocouples D and C (located between B and E) still show temperature variations of about 2 deg C. Such variation in the gradient zone temperature is at least five times smaller than the variation seen when the furnace was controlled in the conventional manner (Figure 5.29). The data point out the fact that the control over temperature in the gradient zone should be exerted over the smallest distance feasible.

5.3.3 Control with two closely spaced sensors

An experiment was conducted (with a model charge) where the two control points (sensors A and B) in the gradient zone were spaced by 1 cm. This experiment was designed to demonstrate that (i) the interface location can be accurately controlled, (ii) the axial gradient at the interface can be controlled during 'growth', and (iii) the proximity of the sensing points of the two control loops does not cause instability due to unwanted coupling between the two control loops. The PID parameters used were (a) for the loop comprised of the top heater and sensor A : $K_p = 0.08$, $T_i/T_s = 500$, $T_d/T_s = 80$, and antiwindup = 5°C; (b) for

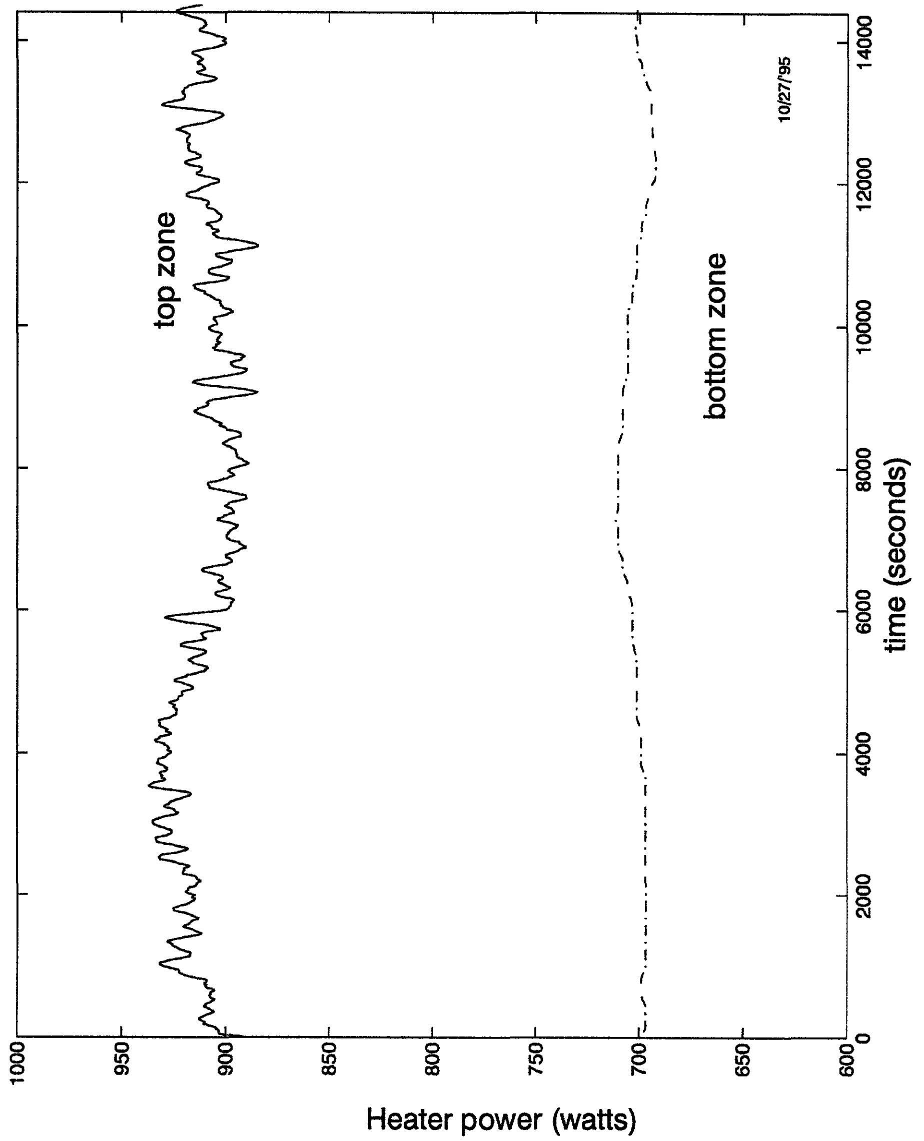

Figure **5.36** : Power requirements for control using two widely spaced gradient zone sensors

control of the bottom heater using sensor E : $K_p = 0.05$, $T_i/T_s = 500$, and antiwindup = 5°C. The dummy charge of boron nitride was translated downwards at 19.8 cm/hr (5.5 μm/s), in flowing helium at 14 psig pressure.

The control sensors A and B were maintained within 0.5°C of their respective setpoints. As in the previous experiments, the power drawn by the two heaters varied to compensate for the changes in thermal coupling caused by charge translation (Figure 5.38). This results in the heat-pipe temperatures

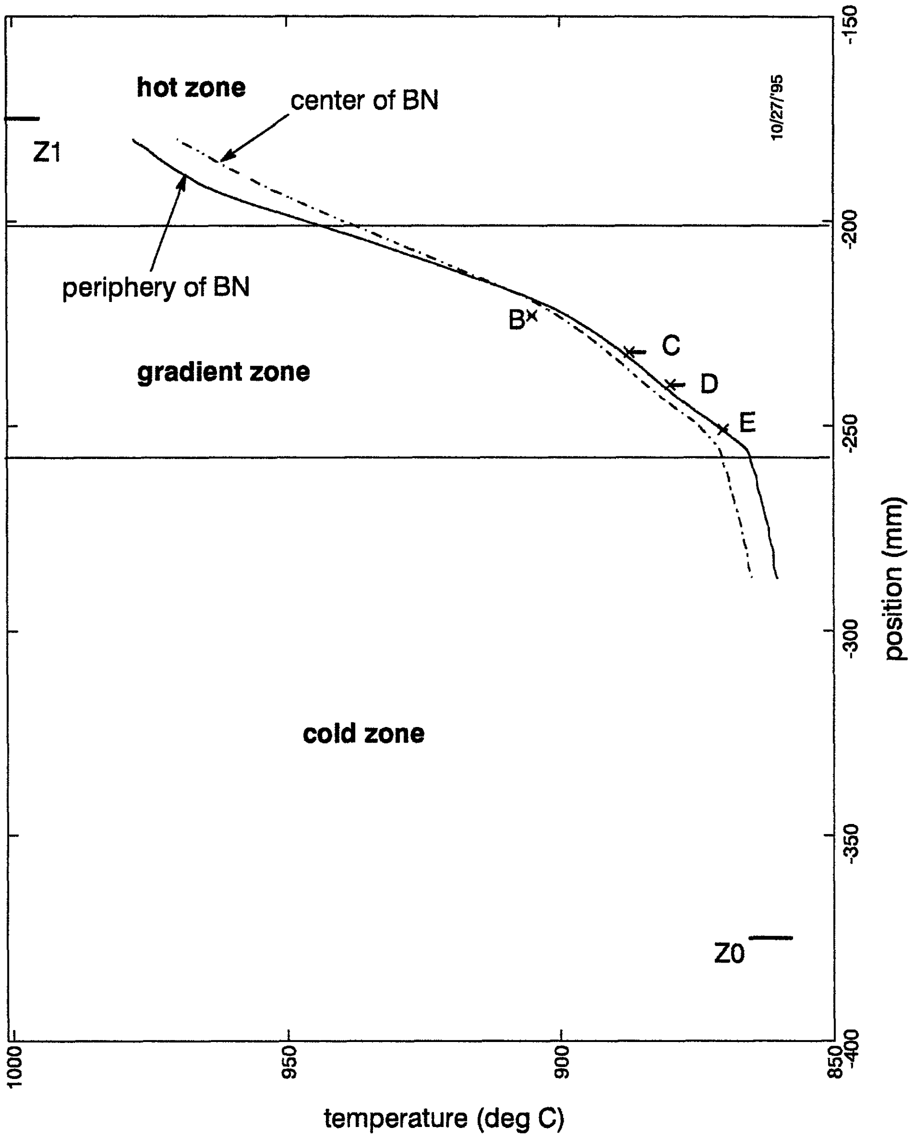

Figure 5.37 : Control in the Bridgman mode, using two widely spaced gradient zone sensors

changing during the 'growth run', but with the result that the temperatures in the region of interest are controlled (Figure 5.39).

5.4 Summary

An improved, PC-based, data acquisition and control system was designed and established for crystal growth in a Bridgman mode, with axial temperature gradient control in the gradient zone. The thermal behavior of the furnace was characterized using a model charge of boron nitride. The results were used to

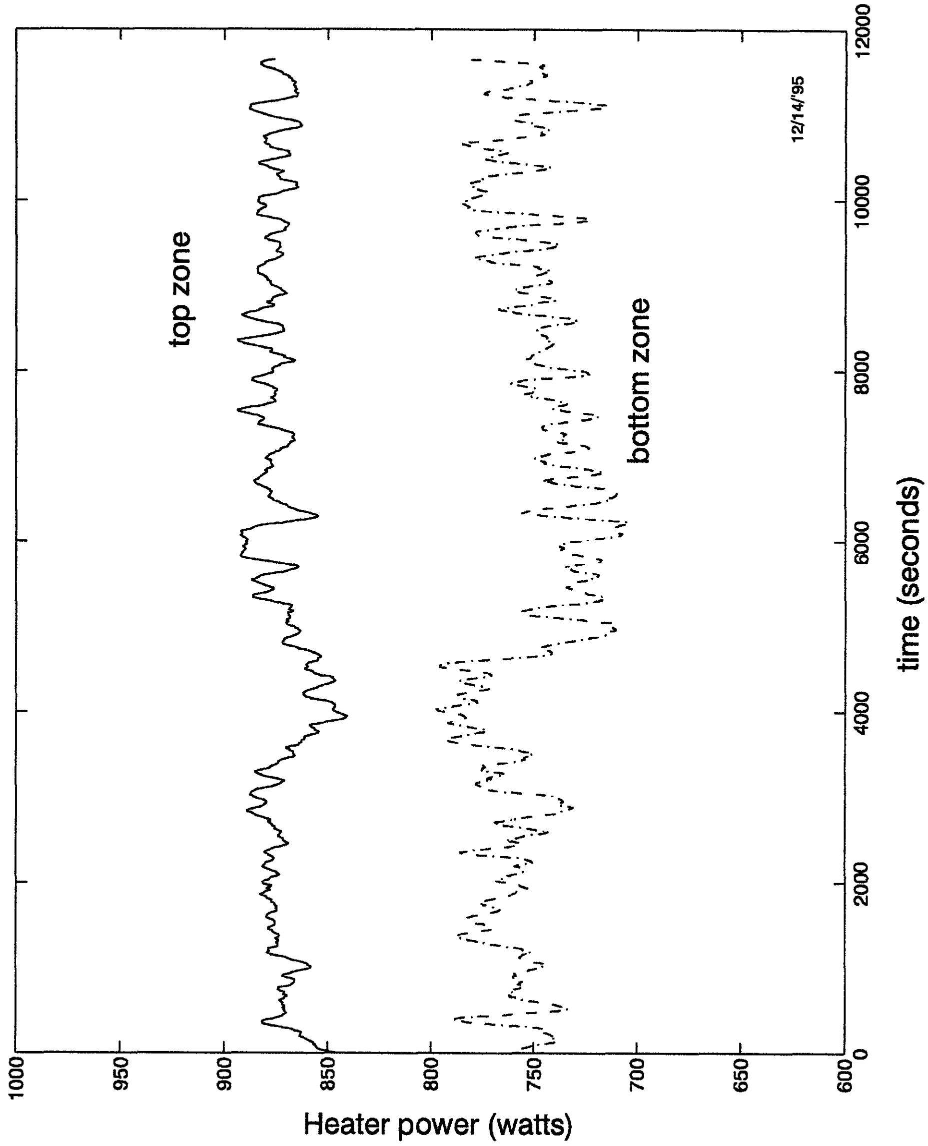

Figure **5.38** : Power requirements of the two zones, for control in the Bridgman mode with two closely spaced sensors

improve the gradient zone design, and to improve the accuracy of measurement of furnace wall temperatures in the gradient zone. It was established that :

- A low thermal conductivity gradient zone results in smaller radial temperature gradients.
- Heat loss along the length of the thermocouple can affect measurements of furnace wall temperatures in the gradient zone, but that this effect can be minimized by appropriate emplacement of the sensors.

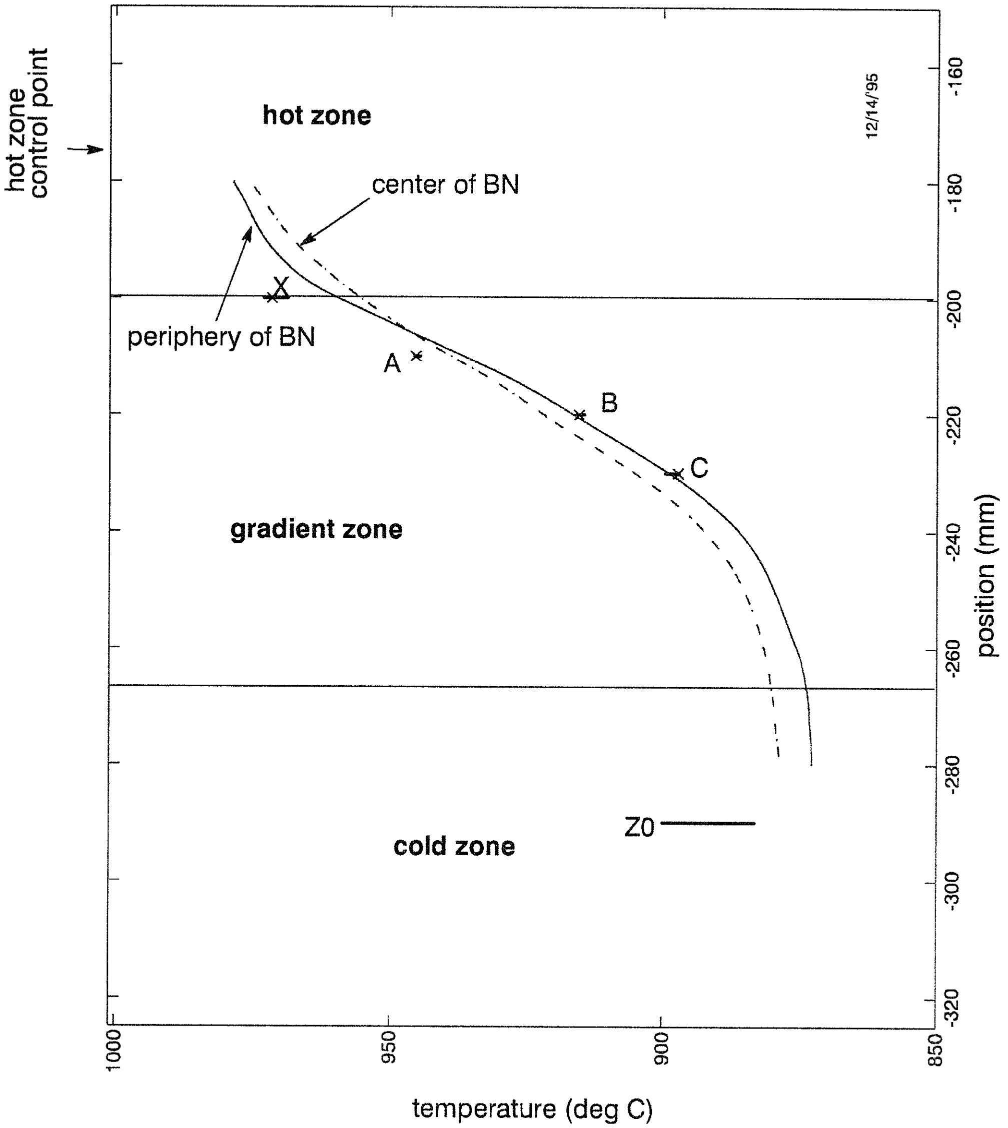

Figure **5.39** : Control with two closely spaced sensors.

- Control of the interface location and of the axial temperature gradient around the interface can be achieved, at growth rates of upto 3 cm/hr (8.5 μm/s).

Chapter 6 Growth of gallium doped germanium in the Bridgman mode of operation

Gallium doped germanium was grown in the Bridgman-Stockbarger furnace arrangement using the 'Bridgman mode of operation'. In this system, the thermal field is controlled by sensors located in the gradient zone. The ampoule design, the growth procedure, and post-growth analysis are described. The resultant stabilization of the interface location is discussed. Segregation results are presented, in the context of the measured interface shapes.

6.1 General features of growth experiments

Seeded growth (<111> orientation) of gallium doped germanium crystals was carried out in the modified vertical Bridgman-Stockbarger furnace. The photograph of the overall system is given in Figure 1.1, the active region of the furnace is shown in Figure 6.1. A scaled drawing of the furnace is given in Figure 6.2, for reference.

All growth experiments were conducted in a dynamic atmosphere of helium at 14 psig. The furnace was baked out overnight, at temperatures between 250°C and 300°C. Prior to growth, the furnace was ramped up to temperature at a rate of 5°C/minute, using the sensors in the heat-pipes for control. The hot zone was taken to temperatures of around 1000°C, while the cold zone was taken to temperatures around 840°C. The control structure of the furnace was then switched to use the gradient zone sensors as the control points. Thermocouples A and B (Figure 5.26) were used to control the power inputs to the top and bottom heaters, respectively, to maintain the thermal field in the charge around the chosen interface location. A temperature gradient of 30 - 35°C/cm was typically maintained across the interface location, by choosing the setpoint of thermocouple A to be around 950°C, and the setpoint of thermocouple B to be around 915°C. The furnace was allowed to equilibrate for 2 to 3 hours before the start of ampoule translation.

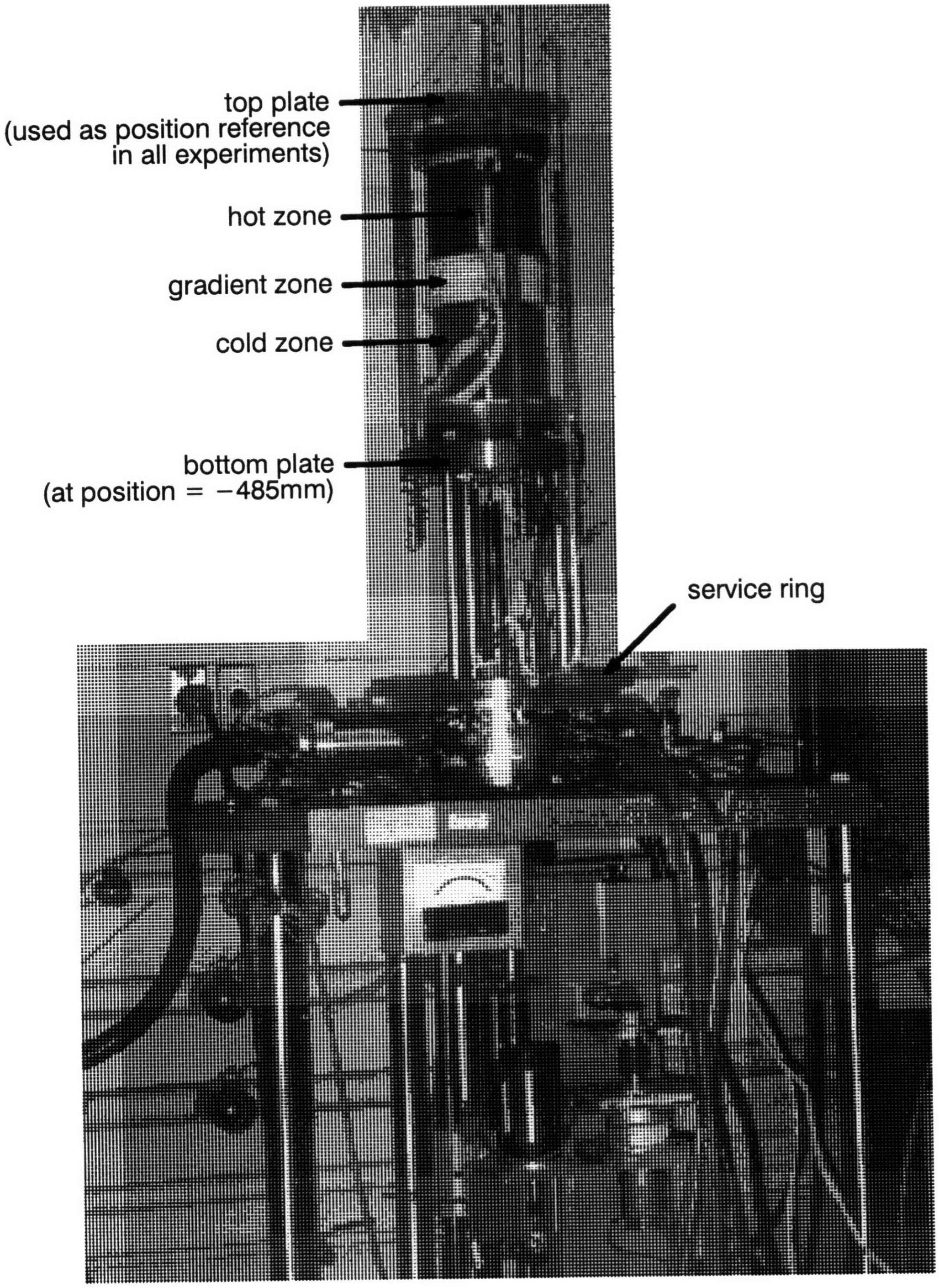

Figure **6.1 :** Picture of the active regions of the furnace, with surrounding support structure.

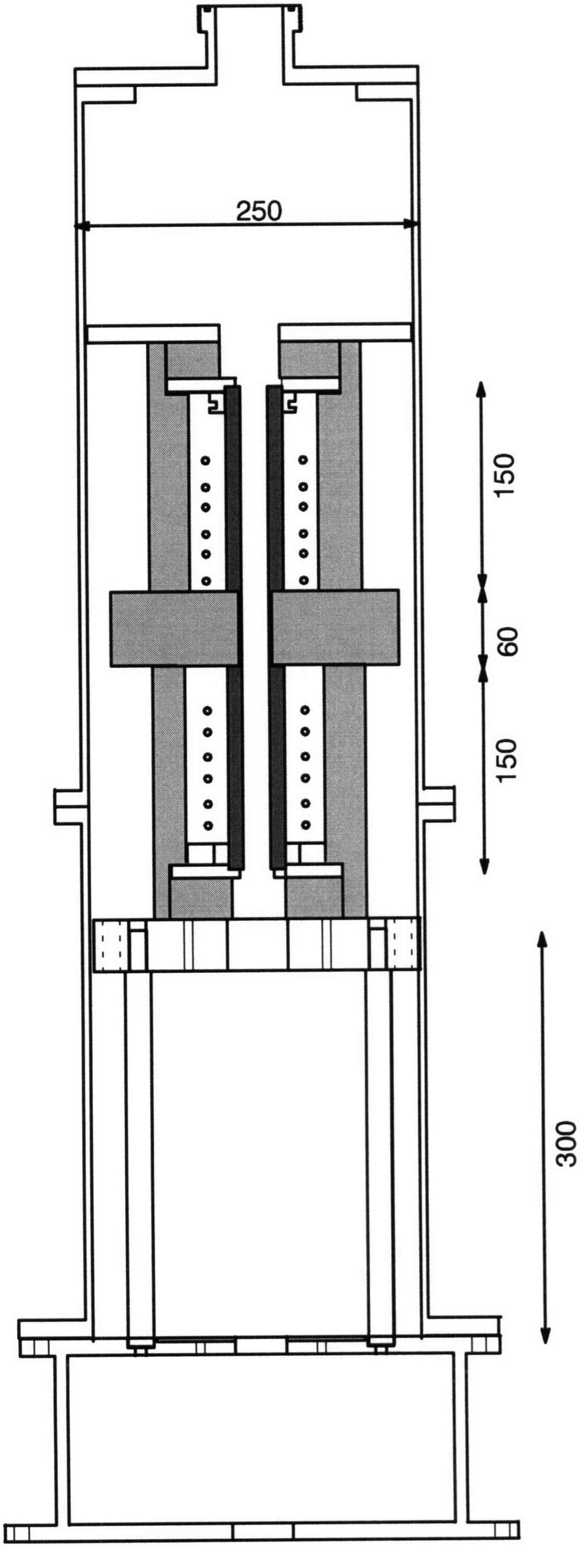

Figure **6.2 :** Scale drawing of the furnace (dimensions in mm).

6.1.1 The crystal growth ampoule

The ampoule for the charge was composite. It had a wall of transparent fused quartz, 1mm thick, outer diameter 16mm, with a 1mm clearance between it and the quartz tube (1mm thick) lining the furnace cavity. To the ends of the quartz tube graphite (POCO) electrodes were attached (Figure 6.3). The top electrode served as contact to the melt. It had a recessed structure that allowed a maximized melt volume to be contained within it, and to create an adequate contact area. The bottom graphite electrode served as the seed holder and electrical contact. Both electrodes had multiple holes to allow the lead wires(Pt or Ag) to be snaked through, for low resistance contacts. A <111> Ge seed of 8mm diameter was used in the growth experiments. The diameter of the charge increased to 14mm in a gradual manner at the top end of the seed electrode.

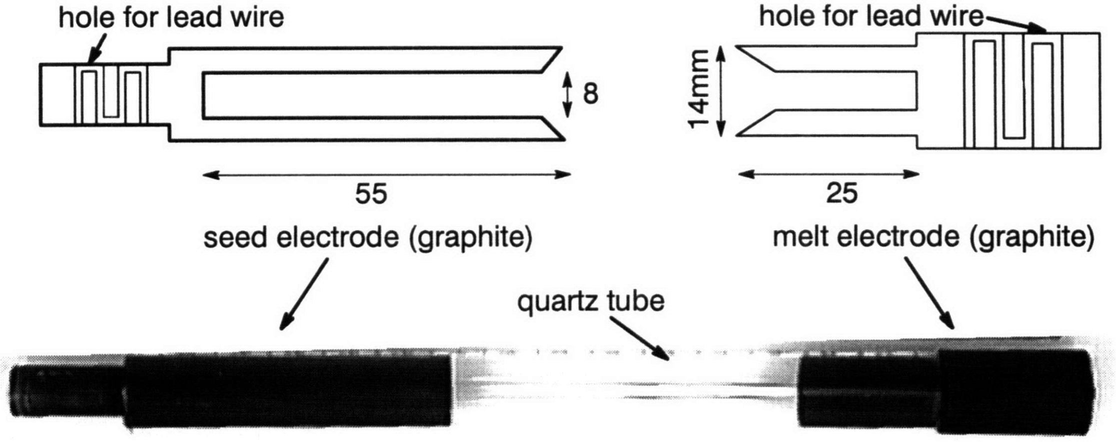

Figure **6.3** : Growth ampoule design

The above features were common to all the growth ampoules used. But the method by which the lead wires for the electrodes were brought to the ampoule was changed. In the first design, both the seed and the melt contact lead wires (Pt, 750um dia) were introduced through the BN support rod. This design suffered from the following : (a) the strength of the BN rod was compromised by the machining needed to take both leads up the BN rod, and it failed prematurely (Figure 6.4). (b) the melt lead wire had to be passed through the 1mm wide annular

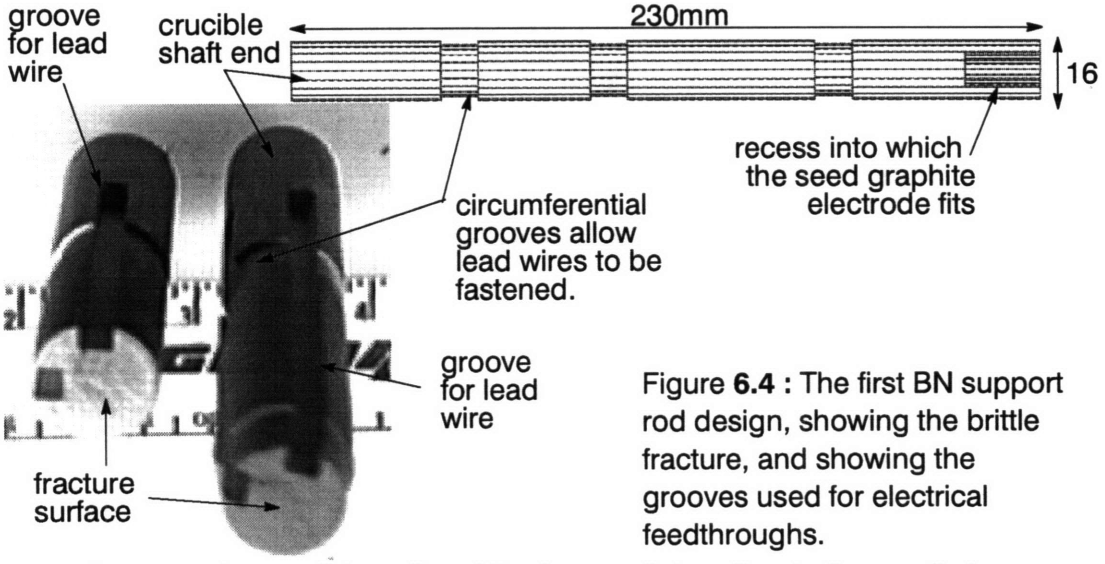

Figure **6.4 :** The first BN support rod design, showing the brittle fracture, and showing the grooves used for electrical feedthroughs.

space between the crucible wall and the furnace lining. Due to the small clearances involved, it was difficult to adequately protect the Pt from alloying with the germanium vapor (Figure 6.5).

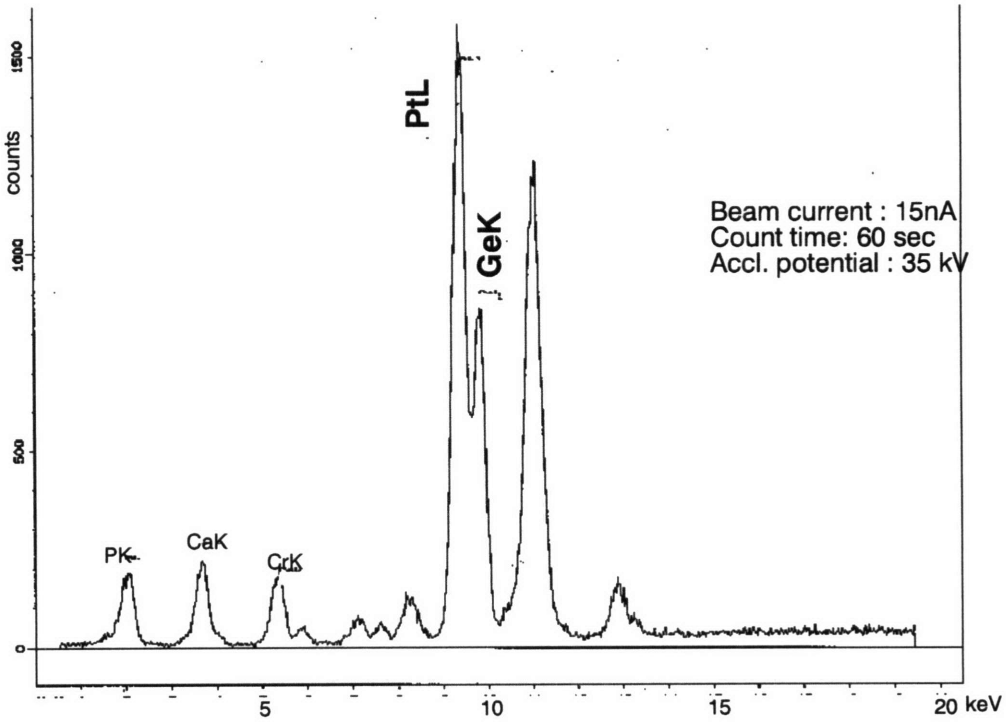

Figure **6.5 :** X-ray fluorescence spectrum of Pt lead wire used in ampoule.

In the second design, the boron nitride rod carried a silver wire, 1mm in dia, as the lead to the seed electrode. The other lead wire (Pt) was connected to the melt electrode from the top of the furnace. This design (Figure 6.6) gave ample

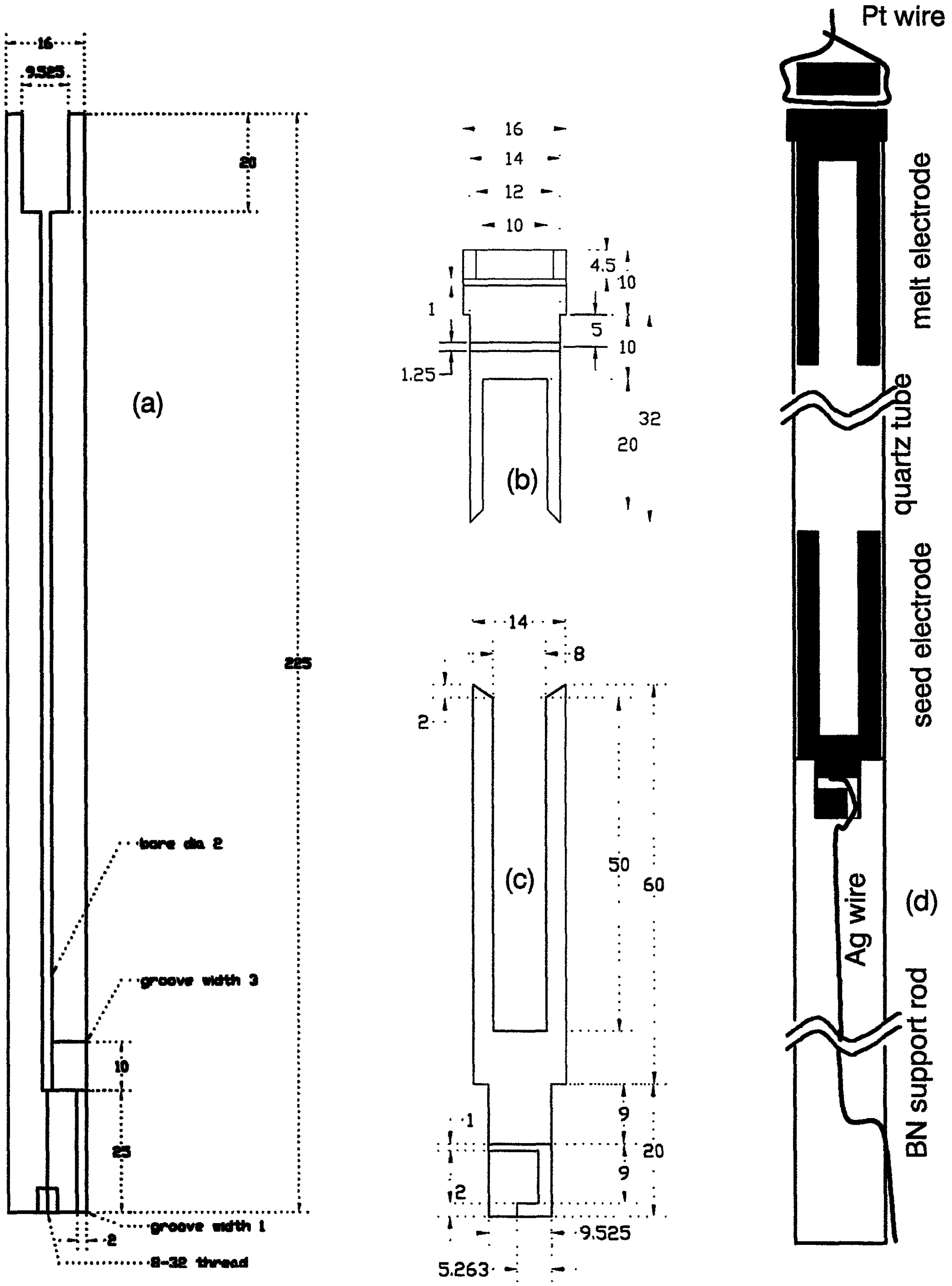

Figure **6.6** : The second design of (a) BN support rod (b) graphite melt electrode, and (c) graphite seed electrode, and (d) assembly

clearance for the Pt wire to be covered with a thick sprayed-on coat of BN powder, and to be enclosed in a recrystallized alumina tube. There was no evidence of alloying on repeated use. To allow for the downward motion of the ampoule, a section of the (pre-annealed) Pt wire was fashioned into a low force constant spring. This was done in the colder section of the wire, well above its entry into the furnace, and therefore, with no need for protection against alloying.

6.1.2 Charge preparation

Polycrystalline chunks of Germanium, doped with Ga at levels less than 1 x10^{17} cm^{-3} were used as the starting material. This was etched in 3:5:3 :: 49%HF: 70% HNO3: glacial CH3COOH for 5 minutes (followed by a 30 second dip in a freshly prepared volume of the same etchant, to remove contamination introduced from the beaker in the previous step). The etched charge was washed in DI water and dried under a stream of pre-purified nitrogen gas, and optionally also heating it gently on low-residue absorbent paper. It was then weighed, and 6-nines purity Ga (etched in 3:1 HCl:HNO3) was added in quantities appropriate to dope the charge to about 9 x 10^{19} cm^{-3}, in the melt. The polycrystalline chunks and the dopant, were placed in a graphite crucible, machined to create a casting volume of the appropriate shape (Figure 6.7). The graphite crucible was placed in a quartz tube, and sealed under a vacuum better than 1 x 10^{-4} torr. This sealed crucible was used to cast a polycrystalline charge of the shape and volume needed to fill the growth ampoule.

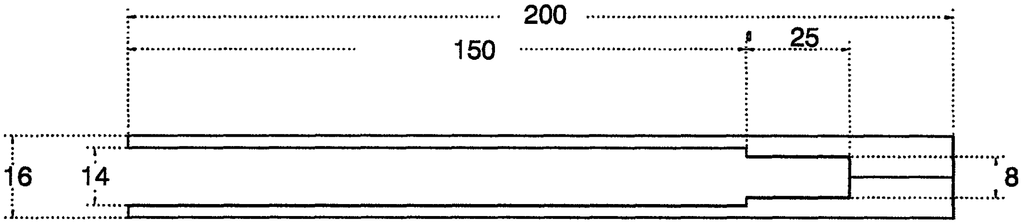

Figure **6.7** : Graphite mold used for casting the (polycrystalline) germanium charge.

The cast charge was extracted by cutting away the graphite, since the polycrystalline germanium charge was invariably keyed into machining grooves and other surface features of the graphite. The seeds were obtained from Czochralski crystals grown in the lab, centerless-ground (by Ceramics Grinding Co, Waltham) to a 8mm diameter, and cut to a length of about 55mm, so as to fit into the seed well of the lower graphite electrode. The cast charge and the seed were etched (in the fashion described above, for the starting material), before final assembly of the growth ampoule. Prior to assembly, the quartz tube was etched for 5 minutes in 49% HF. The lead wires were cleaned in semiconductor grade acetone and methanol. The assembly, with the lead wires threaded into place was introduced from the bottom of the furnace, secured to the charge translation mechanism, and the electrical contacts attached.

6.2 Interface demarcation by current pulses

Current pulses transmitted across the crystal-melt interface during growth were used for interface demarcation[63]. Current pulses sent across the crystal-melt interface, were of a polarity such that the electrons cause heat absorption at the interface for the duration of the pulse, *ie* Peltier cooling[64]. The increased loss of heat from the interface causes the microscopic growth rate to increase momentarily, leading to increased dopant incorporation ($k_{eff} = 1$). There is hence a thin layer of increased dopant concentration formed, at every instance of current pulsing. This layer of higher dopant concentration accurately delineates the interface shape at that instant. The increased doping is a feature that can be seen in post-growth etching analysis of the crystal, thereby permitting interface shape and location measurements. The current density used in generating these interface demarcation lines was 24 A/cm^2.The current pulses (between 25 and 75ms long) are coded to represent specific points of time, as explained on page 73. Every hour of growth is marked by a doublet (caused by a 'double' pulse - see Figure 5.8). At 10 minute intervals, a pulse is skipped. Both of these codes make it possible, during post-growth analysis, to know precisely the time at which any particular portion of the crystal was grown, and the rate at which it was grown.

6.3 Post-growth analysis procedures

6.3.1 Sample preparation

The grown crystals were extracted from the ampoule, and cut with a wire-saw (South Bay Tech, Inc, Model 850), using a 250 µm thick wire, coated with a glycerol-based slurry of 600 µm SiC. The crystal was cut into segments that were 25mm long, and a1.5mm thick slice was cut longitudinally, so as to have the axis of the ampoule on one surface (Figure 6.8). The slices were mounted on brass discs, either with In-Sn (ultrasonically soldered) or with CrystalBond (a polymeric resin). The sample surface was lapped on an optically flat glass plate, with 17 µm garnet, and cleaned thoroughly with soap and DI water. The sample was then chemo-mechanically polished (CMP) for 30 minutes on a Rodel 204 pad. The CMP was done with a solution of Syton (colloidal silica), DI water, and 5.25% NaOCl (Clorox) in the volume ratio 600:400:60. This solution, and a separate DI water feed, were dripped onto the pad at the rate of 2 to 3 drops per second, with a pad speed of 100-150 rpm. It was found to be essential that that the last two minutes of the polishing be done with a copious flow of DI water, to wash off the colloidal silica entirely. If this last step was not carried out, severe scratches became visible on the sample surface upon etching, even if the as-polished surface was smooth (Figure 6.9). When the polishing action was tapered off in the aforementioned manner, smooth surfaces could be retained - it was felt that this was due to the removal of any retained agglomerated silica clumps by the last step. After

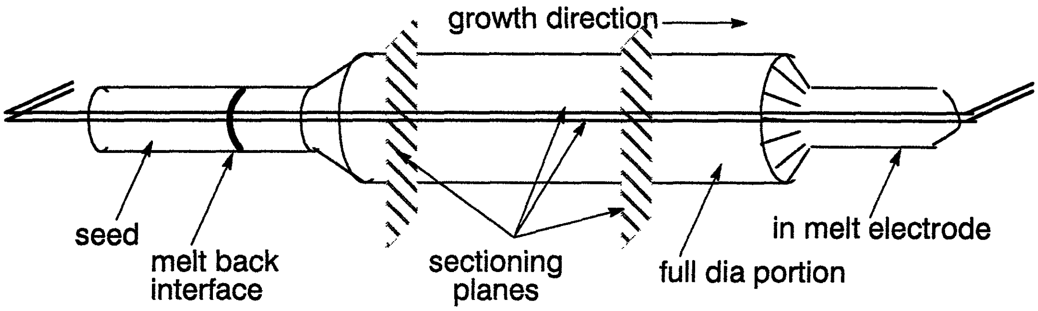

Figure 6.8 : Sectioning of the grown crystal.

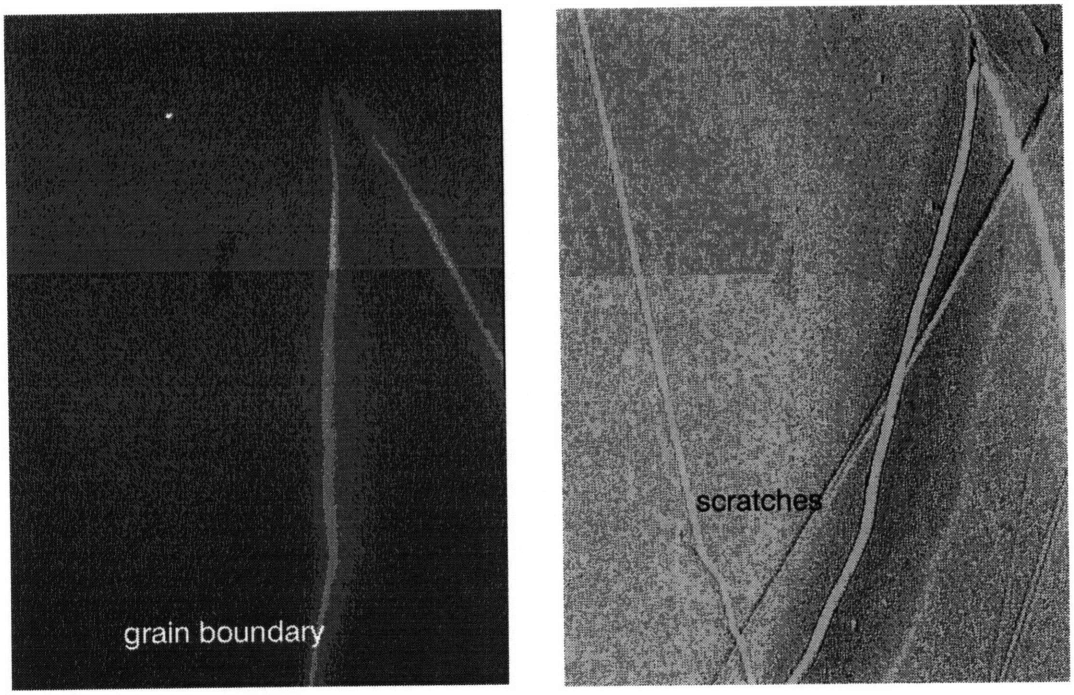

(a) (b)

Figure **6.9 :** (a) As polished surface and (b) etched surface, when the polishing action is not 'tapered off'.

polishing, and prior to etching, the samples were placed under DI water, to prevent encrustation of the surface by any remaining colloidal silica.

The etching procedure consisted of a 6 - 10s dip (with agitation) in 1:1:1 :: 49% HF: glacial CH_3COOH : 30% H_2O_2. The samples were then transferred to a bath of sodium bicarbonate solution to neutralize any acid remaining on the sample. The sample was washed with soap, then with DI water, and dried under a slow stream of pre-purified nitrogen gas. Absorbent paper was used to wick up remaining traces of liquid in crevices near the sample edges - this ensured that the surface remained pristine over time. With this precaution not taken, traces of acid remaining in the sample edge invariably caused undesirable etching of the peripheral areas of the sample, over time.

After etching, interface demarcation lines can be observed under Nomarski contrast, or 'differential interference contrast', microscopy (Figure 6.10). The lines seen in the figure were generated by 75ms-long pulses that were 10 seconds apart.

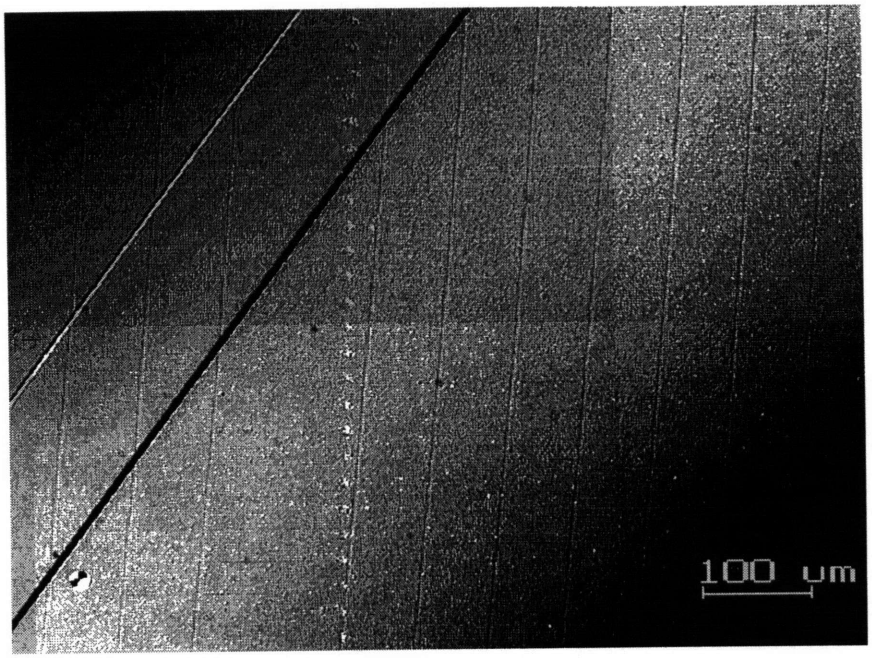

Figure **6.10 :** Interface demarcation lines, along with impact trace of a spreading resistance analysis.

It should be noted that the apparent width of the line is dictated by the etch time, and more so by the details of image formation in the optical train that gives Nomarski contrast. That is, the 'metallurgical' width of the region of increased doping is significantly smaller than linewidths seen in Figure 6.10 might lead one to believe.

6.3.2 Growth rate measurement procedure

Interface demarcation by current pulses confers the benefit that the actual growth rate of the crystal can be measured at a microscopic level, anywhere in the crystal. If the spacing between the interface demarcation lines is measured at 85 μm, and it is known that the current pulses were sent at 10s intervals, the microscopic growth rate is known (as a 10-second average value) to be 8.5 μm/s.

The spacing of interface demarcation lines was measured on a Carl Zeiss microscope fitted with a CCD camera (COHU, Inc), connected to a TV monitor (Sony Trinitron). A reticle was used to calibrate the magnification of the image as seen on the monitor. It was found to be 245x, when using a 4x (Nomarski) objective, with the ring magnifier of the microscope set at 1.25x. The sample was placed on the microscope stage, and its orientation adjusted manually to align the sample edges with the x- and the y- translation directions of the microscope stage. The image of a section of the crystal was captured on screen, and the measurements made off the screen, care being taken to eliminate parallax error. The error in measurement, on screen, was +/− 0.5 mm. At typical growth rates, the on-screen spacing of the interface demarcation lines was about 20mm. Hence the error in measurement of the growth rate is less than 3%, at typical growth rates. During initial transients, when the growth rate is lower (but increasing), the spacing between the lines is smaller. The smaller spacing results in a larger percentage error, since the same magnification is used.

6.3.3 Spreading resistance measurement procedure

Crystal samples were ultrasonically soldered to brass discs (if they had not already been soldered, prior to polishing), to allow single-probe spreading resistance measurements to be made. In the single-probe spreading resistance technique, current flows from a point contact at the surface of interest (the polished, prepared surface), spreads throughout the body of the sample, across equipotential contours dictated by the sample geometry, and flows out of the entire back surface contact (Figure 6.11). The predominant contribution to the resistance

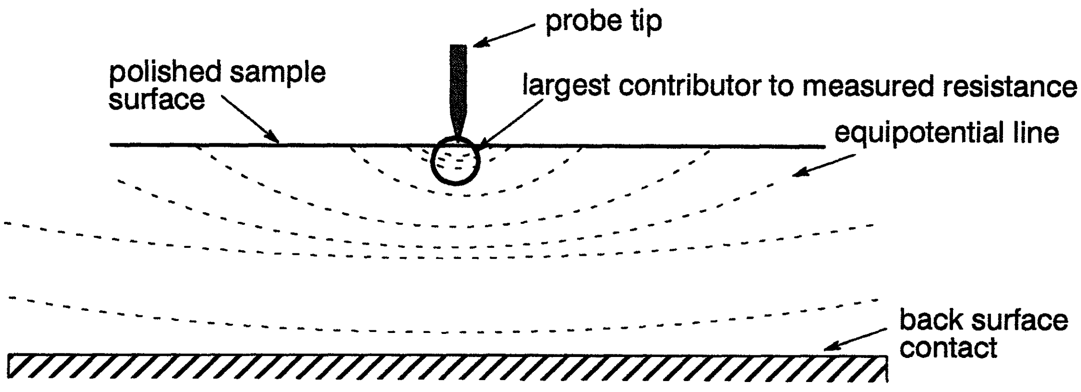

Figure **6.11** : Schematic of potential distribution in single point spreading resistance measurements of the circuit comes from the small volume immediately beneath the probe's contact point. Hence, a measurement of the resistance of the circuit gives the resistance of a small volume near the probe.

Through appropriate calibration, the resistance can be directly related to the resistivity of the material composing the small volume of interest. Similar calibration can be used to relate the measured resistance to the carrier concentration in the sampled volume at the contact point. Hence it is possible to map the carrier concentration with a spatial resolution of 10 μm, using the spreading resistance technique. Details of the equipment used, and of the calibration procedure, are provided in Appendix A.

6.4 Analysis of crystal growth experiments

6.4.1 Surface features of grown crystals

It was invariably found that the quartz ampoule (1mm wall thickness) had been cracked during cool-down, *after* growth of the crystal. Cracking could be avoided by using a quartz crucible of 2mm wall thickness. Such a modification was not made to maximize the cross-sectional area of the grown crystal, and since cracking of the crucible was occurring at non-critical times. It was also found that the graphite electrodes were keyed into the surface of the grown crystal. They were removed by cutting partway into the graphite, and then dissolving the graphite in saturated solution of $K_2Cr_2O_7$ in H_2SO_4 at 150°C. It was verified that this solution did not attack germanium at any measurable rate in the time scale involved (a 10-minute immersion was sufficient to release the crystal from the graphite contacts).

The surface of all crystals was shiny, and 'pockmarked' by bubbles. Such bubbles were not found on cast polycrystalline charges. This suggests that the impermeability of the quartz crucible, coupled with the fact that crystal growth was carried out in a helium ambient at 2×10^5 Pa (2 atm), was responsible for bubble formation. No bubbles were entrapped in the interior of the grown crystals. On the surface of the charge, the average diameter of the bubbles was found to increase along the growth direction (Figure 6.12). A ‘denuded zone’ devoid of bubbles could be observed around the bigger bubbles. In between the denuded zones, a high density of smaller bubbles could be be observed (Figure 6.13). These

Figure **6.12 :** Surface of as-grown crystal, showing bubble distribution

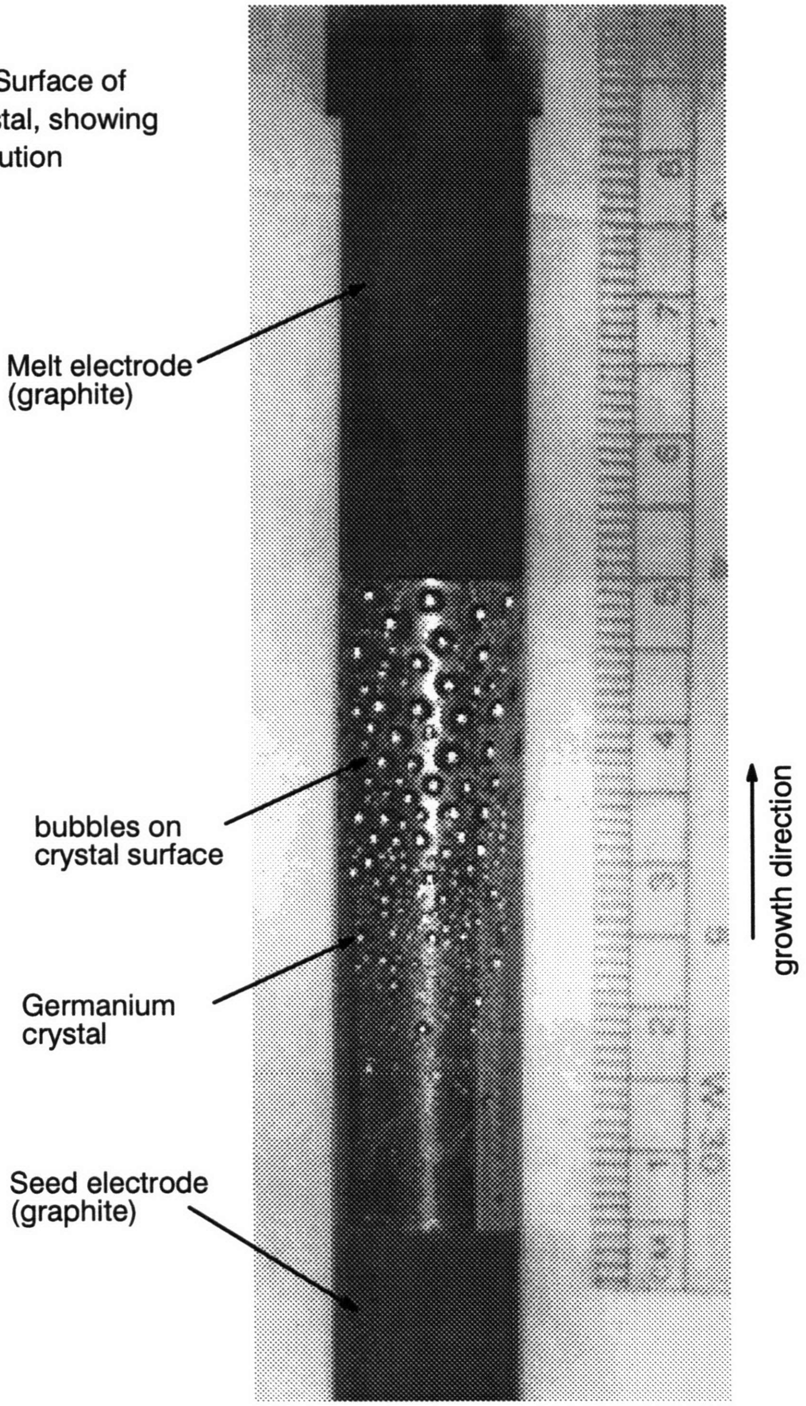

Figure **6.13** : Schematic of the denuded zones observed around the larger bubbles.

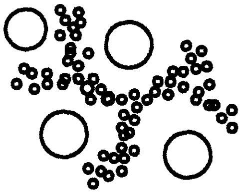

observations are consistent with a model which assumes a considerable quantity of dissolved He in the melt. As growth proceeds, He is rejected into the melt, due to the decreased solubility of gases in the solid phase. The gas concentration in the melt increases as growth proceeds, increasing the driving force for bubble formation, and increasing the total bubble volume. (Discussions with Mr. Yu Zheng on the issue of nucleation and growth of the bubbles are gratefully acknowledged). The bubble formation can clearly be decreased by using an ampoule that is sealed under vacuum[59].

6.4.2 Results of growth rate stabilization experiments

A growth run was conducted in the 'Bridgman mode of operation' using thermocouples A and B (separated by 10mm and located at the wall of the furnace cavity, in the gradient zone) as the control points. Thermocouples A and B were controlled to be within 0.5°C of the setpoints of 950°C and 917°C respectively(Figure 6.14), after the initial transient (when the sensors were within 2°C of the setpoints) . The melting point of germanium being 932°C, the interface is expected to be 5mm above the location of thermocouple A, with the setpoints chosen. That is, the interface is localized at a point15mm below the top end of gradient zone (which is 60mm long). In the grown crystal, it was confirmed that the seeding point was at the location expected, to within 1 mm. (This agreement between the actual and the expected seeding position was seen in all crystal growth runs conducted in the 'Bridgman mode of operation').

The length of the full-diameter portion of the charge was 60mm, with a 10mm extension, at reduced diameter, into the cavity within the melt electrode. The seed length was 46mm, which was melted back by 10mm for seeding. The total

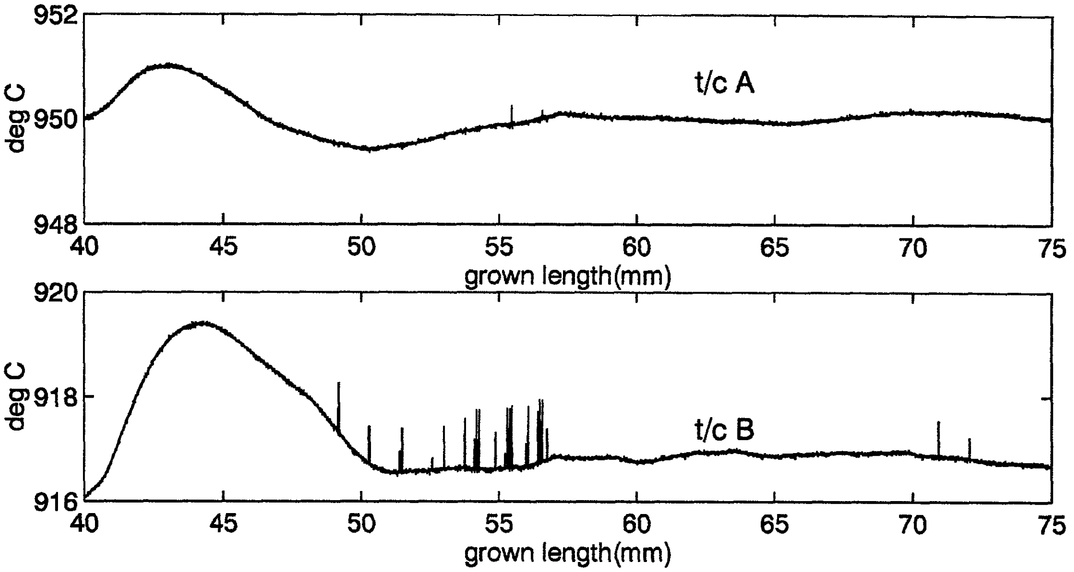

Figure **6.14** : Temperature readings of the two control sensors during growth in the Bridgman mode of operation.

melt length at the seeding point was hence 80mm. This length was chosen to accentuate transients caused by short charges. After 40mm of growth at a rate of 5.55 μm/s, the translation rate was stepped up to 8.5 μm/s, and interface demarcation turned on, simultaneously. The growth rate along the centerline of the crystal was measured, and the results show that the growth rate and the translation rate coincide (Figure 6.15).There is an initial transient in the growth rate, extending

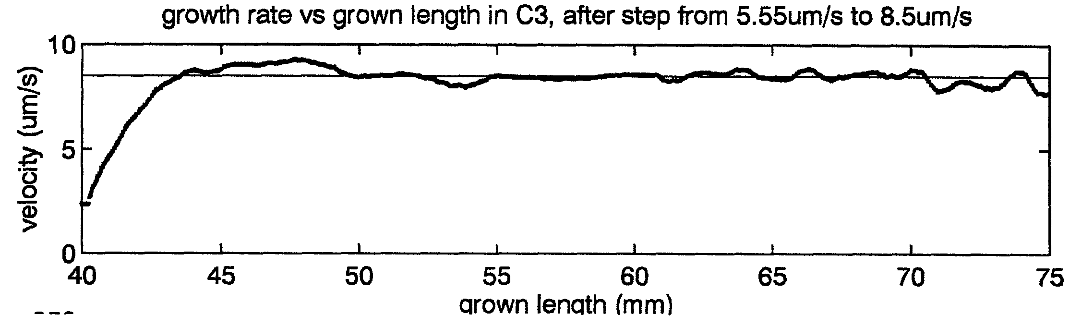

Figure **6.15** : Measured growth rate *vs* distance grown

through about 5 mm of growth. This contributes to most of the interface relocation seen over the course of the growth run (Figure 6.16). It should be noted that the transient in Figure 6.15 starts from a (measured) initial velocity of 2.5 μm/s, even

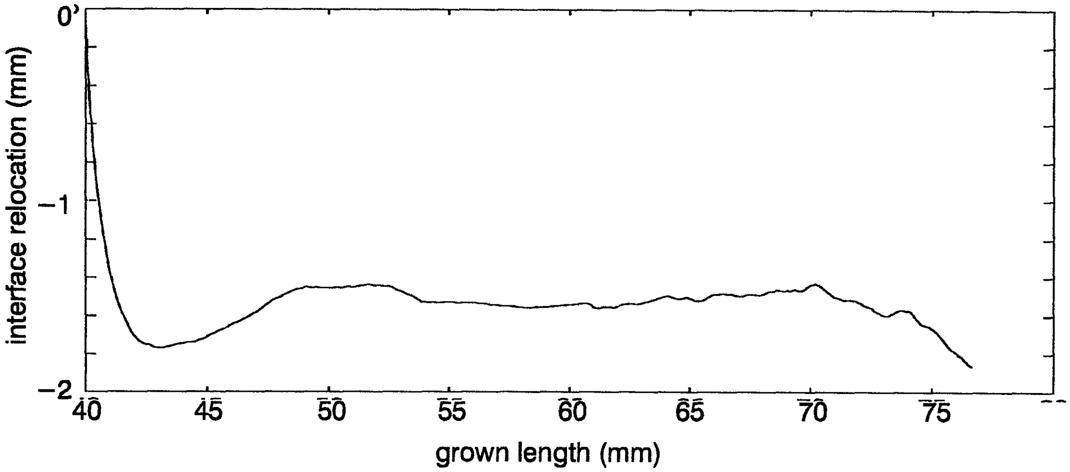

Figure **6.16** : Interface relocation as a function of length of crystal grown.

though the translation rate prior to this instant had been held at 5.55 μm/s. It is also known that the growth rate of the crystal ought to have been close to 5.55 μm/s, since the start of the sequence of interface demarcation lines was seen at a location commensurate with a previous growth rate of 5.55μm/s.

The reason for the initially lower growth rate is Joule heating of the bulk of the growth ampoule associated with current flow related to current induced interface demarcation. The axial heat fluxes in the system have been computed (page 97) to be about 30 watts. The resistance of the growth ampoule is about 0.2 ohms (a large percentage of which is due to the graphite and the contact resistance between the graphite and the charge, since the resistivity of germanium at the melting point is low). With current pulses of 36 A, lasting 75ms, at a rate of 0.1 Hz, the average power input to the growth ampoule due to Joule heating is about 2 watts. Hence Joule heating due to interface demarcation contributes to about 7% of axial heat fluxes in this crystal growth system. In ground-based experiments using the NASA Crystal Growth Furnace, (prior to growth experiments in the Space Shuttle), the start of interface demarcation was associated with a rise in temperature of the gradient zone by several degrees[59]. Such Joule heating effects due to interface demarcation pulsing are not seen in Czochralski furnaces, due to the fact that furnace heat fluxes are typically much higher. At such higher base fluxes, the start-up transient in growth rate due to the generation of Joule heat is not noticeable.

To avoid a recurrence of this transient due to Joule heating in later growth runs, the interface demarcation was turned on an hour prior to commencement of growth (and re-initialized at that instant, to ensure that the time base could be known in an absolute fashion). The PID parameters employed for the above run were: (a) for the control of the top heater using sensor A : $K_p = 0.08$, $T_i/T_s = 500$, $T_d/T_s = 80$, antiwindup = 5°C; (b) for the control of the bottom heater using sensor B: $K_p = 0.13$, $T_i/T_s = 300$, $T_d/T_s = 100$, and antiwindup = 5°C. Since the temperature control was found to be less than optimal during the initial transient, the PID loops were retuned before the next growth run. In a subsequent experiment, growth was initiated at a rate of 8.5 μm/s, to study the controllability of the process at this high rate of translation. The control exerted over the temperature of the sensors A and B is better (Figure 6.17). The PID parameters

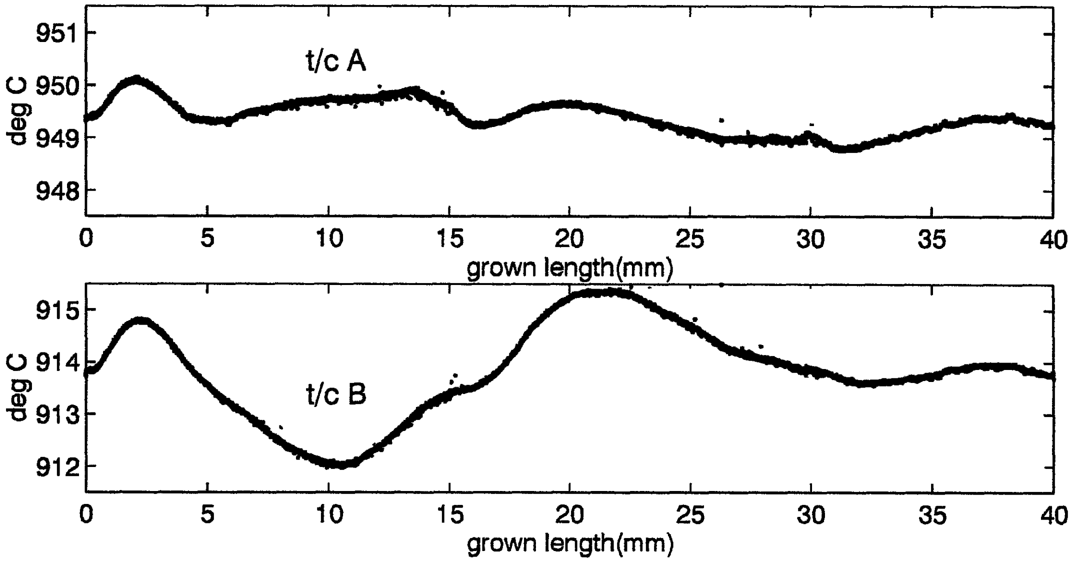

Figure **6.17** : Temperature readings of the two control sensors during growth in the Bridgman mode of operation.

used here were : (a) for the control of the top heater using sensor A : $K_p = 0.08$,

$T_i/T_s = 500$, $T_d/T_s = 80$, antiwindup = 5°C; (b) for the control of the bottom heater using sensor B: $K_p = 0.13$, $T_i/T_s = 400$, $T_d/T_s = 90$, and antiwind- up=5°C. The measured growth rate along the centerline shows behavior that is similar to an underdamped system, with an overshoot, followed by a dip under the required rate, before settling into the required rate (Figure 6.18). The control over the interface location is maintained to nearly the end, at which point the high doping caused constitutional supercooling and interface breakdown. The data also shows that a very large step in growth rate cannot be accomodated by the current system without a correspondingly large initial transient. There appears to be no strong correlation between variations in the temperature records of thermocouples A and B, and the growth rate variations. However, this issue needs to be pursued after the control algorithm has been changed to improve temperature control over gradient zone sensors. (If large steps in translation rate are necessary, it might be advisable to increase the rate gradually, rather than in a single large step. If the thermal mass of the system were to be reduced, while still retaining adequate thermal insulation, the time constant of the system would be decreased, and larger step in translation rate could be successfully employed).

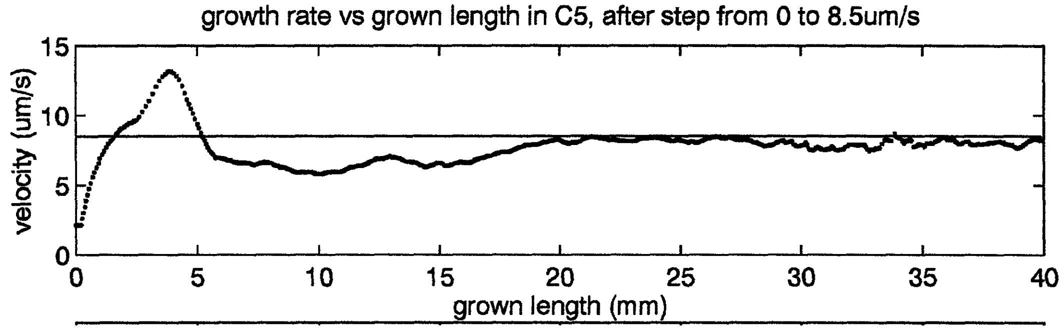

Figure **6.18** : Measured growth rate *vs* distance grown

A conventional growth run was also conducted, with the furnace being controlled in the conventional manner (using thermocouples in the hot and cold heat-pipes, and allowing the gradient zone to take on whatever temperatures are dictated to it by the specifics of charge/furnace coupling). It can be seen that, though the two heat-pipes were controlled to within 0.1 °C of the set point, the gradient zone became steadily hotter during the growth run (Figure 6.19). The figure also shows that for most of the run, the measured growth rate (along the centerline) is well below the translation rate, giving rise to interface relocation and transient effects. This is because of the short charge length, and the 'infinite length criterion' not being satisfied.

Favier[60] developed a methodology for predicting the time constant for the rate of increase of the crystal growth rate when the ampoule was subjected to a steady translation (this assumption is satisfied in the experiment). He also assumes constancy of the furnace thermal field. From Figure 6.19, it can be seen that the assumption of constant thermal field is not satisfied, due to the short length effects. If the expression is nonetheless applied, we get :

$$\tau \approx \frac{a\varrho C_p}{h}$$

where τ is the characteristic time, R is the radius of the crucible, ϱ is the density of the charge, C_p is its heat capacity, and h is the surface heat transfer coefficient. h is already known to be 430 W/m^2. C_p for liquid germanium at 1000 °C is 350 J/kgK, R = 0.2 m, ϱ, the density of liquid germanium is 5.48 x 10^3 kg/m^3. Hence τ, the time constant, should be about 850 seconds. From the growth rate data, it was found that the time constant is 500 seconds. This is considerably quicker than predicted, but the discrepancy should come as no surprise since the basic assumption, one of constant thermal field, used in the Favier analysis is not met in the growth of short lengths of germanium.

6.4.3 Axial segregation measurements and analysis

The effective segregation of dopants is affected by variations in growth rate, and by the nature of convection in the semiconductor melt. If convection is intense, the melt is well mixed, and the Scheil equation, below, gives the distribution of dopants along the growth direction (the axial segregation behavior) for a batch solidification process.

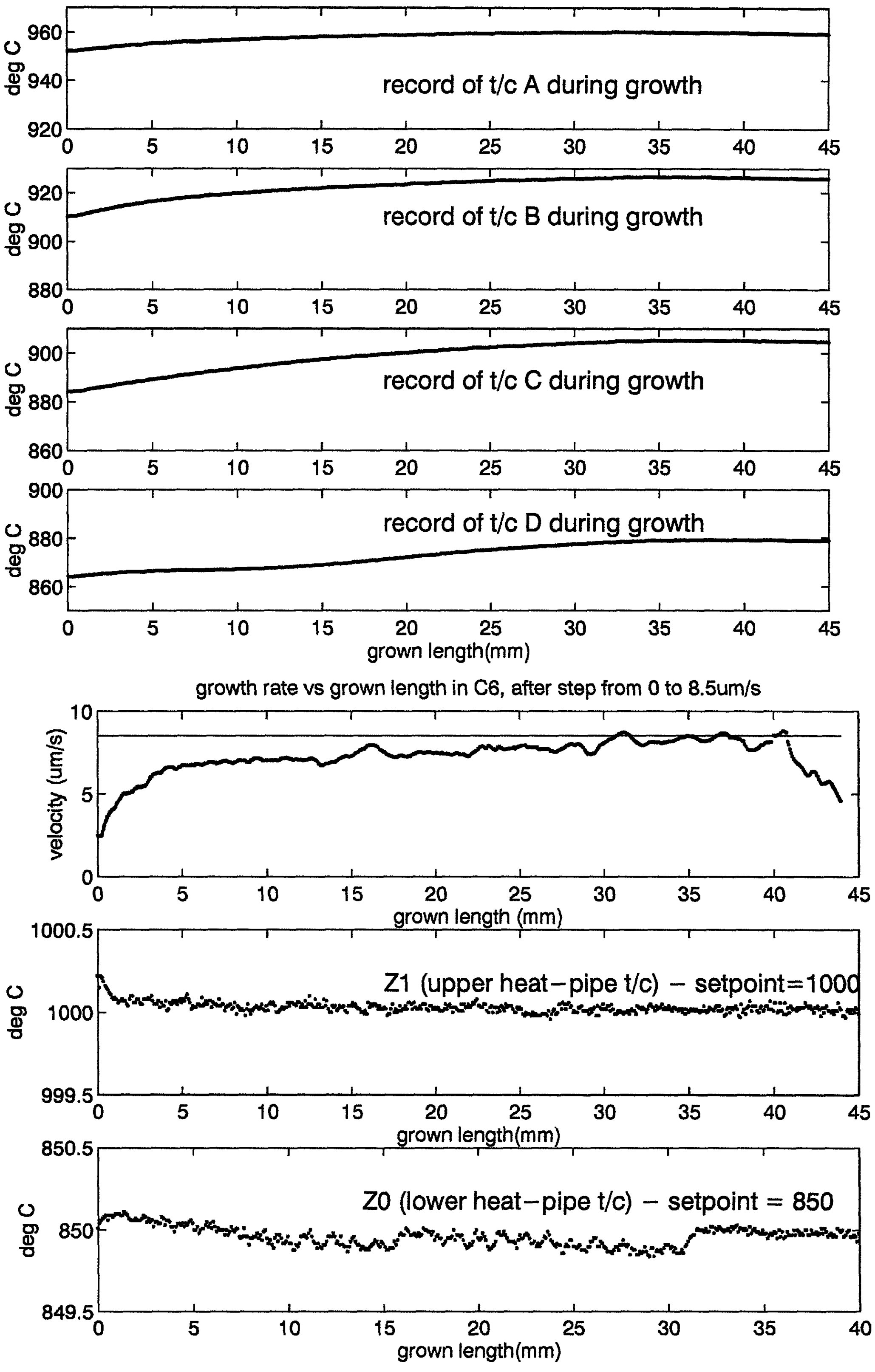

Figure **6.19** : Gradient zone excursions, and non-steady growth rate seen for furnace control in the conventional fashion.

$$C_s(z) = k_{eff}C_0(1 - \frac{\varrho_s z}{\varrho_l L})^{(k_{eff}-1)}$$

where C_S is the dopant concentration in the crystal, k_{eff} is the effective segregation coefficient, C_0 is the starting dopant concentration in the liquid, ϱ_S/ϱ_L is the ratio of densities of the liquid and the solid, z is length of crystal solidified, and L is the total length of the charge, upon solidification.

The Burton-Prim-Slichter (BPS) equation, below,

$$k_{eff} = \frac{k_0}{k_0 + (1 - k_0)\exp(-\delta\frac{V}{D})}$$

relates the effective segregation coefficient under steady state conditions to the growth rate, V, the boundary layer thickness, δ, and the diffusivity of the dopant in the liquid, D, and the equilibrium segregation coefficient k_0. For Ga in Ge melt, $D = 1.9 \times 10^{-4}$ cm^2/s[48].

Under conditions when the dopant rejected at the growth interface is transported into the bulk of the melt by diffusion alone (*ie,* in the absence of convection), the approximate Tiller[61] equation, given below, can be used (the exact solution by Smith *et al*[62] improves the accuracy by about 17%) :

$$C_s(z) = C_0(1 - (1 - k_0)\exp(- k_0\frac{Vz}{D})$$

In the following analysis, the starting dopant concentration in the liquid, C_0, was chosen to match the measured concentration at the start of growth, due to the uncertainty in *a priori* knowledge of that parameter. The uncertainty arises from losses due to evaporation during casting of the charge, and from the non-uniform distribution of dopants in the cast charge itself. As a result, C_0 can be greater or smaller than the nominal doping (of 9×10^{19} cm^{-3}, in this case), perhaps even by a factor of 2. The growth rate has been assumed constant, at 8.5 μm/s. This assumption is not true for the first 10mm or so of growth.

Single point spreading resistance measurements were made along the centerline of the samples, and the carrier concentration calculated using the calibration presented in Appendix A. The measured dopant concentration, the fully-mixed solution, and the purely diffusive solution are all shown in Figure 6.20.

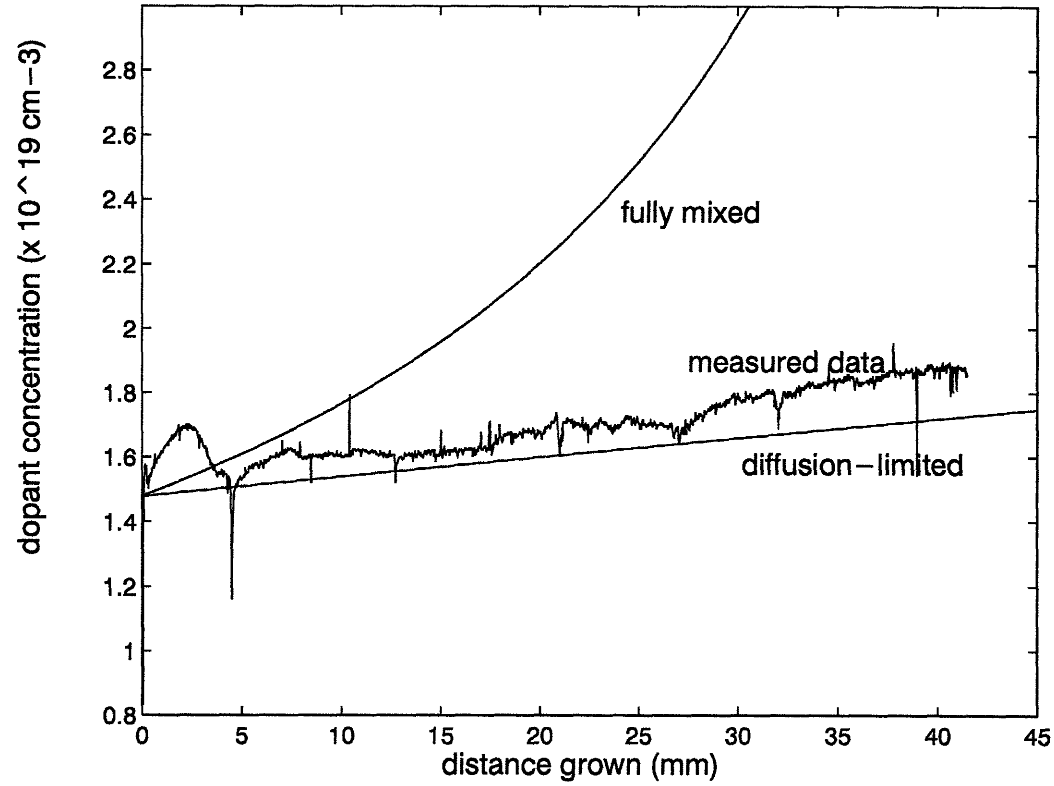

Figure **6.20** : Axial segregation in the Bridgman mode of operation, compared with the limiting cases of purely diffusive and fully-mixed transport.

It can be seen that neither limiting case describes the measured axial segregation satisfactorily, but the measured segregation behavior is better approximated by the diffusive transport model, with the caveat that convection is present and is influencing the dopant segregation. Optical microscopy showed that the intensity of striation increases as growth proceeds, *ie* as the melt aspect ratio decreases. Hence the extent of convective interference increases as growth proceeds.

For comparison, the value of k_{eff}, the effective segregation coefficient, was calculated at a few chosen points along the growth axis, in a different fashion. A recursive form of the Scheil equation was used to calculate k_{eff} :

$$\log k_{eff} = \log(\frac{C_s(z)}{C_0}) + k_{eff}\log(1 - \frac{\varrho_s z}{\varrho_L L})$$

where $C_s(z)$ is the concentration of the dopant in the solid after distance z had solidified. Using $C_0 = 1.7 \times 10^{20}$ cm^{-3}, the value of k_{eff} so calculated was found to decrease from 0.1 near the start, to 0.083, at the end of growth, a change of about 10%. At equilibrium, the value (k_0) of the segregation coefficient of Ga in Ge is 0.087[48]. From the BPS equation, we see that as δ is decreased by increased convective perturbance, the effective segregation coefficient approaches k_0. Towards the end of growth, the melt volume left is smaller, but it has the same axial temperature gradient at the interface as at the start of growth. (The temperature gradient is kept constant, due to the fact that the sensors A and B, which are close to the interface, are maintained at the same temperature). Since the gradient is not allowed to decay (as would be the case in conventional Bridgman growth), convection is higher towards the end of growth. In addition, due to the small melt volumes, the influence of any amount of convection is felt more strongly. It is therefore understandable that the computed values of k_{eff} tend towards k_0 at the end of growth, as the convective interference rises. The value of $k_{eff} = 0.1$ can be associated with a boundary layer thickness of about 450 microns, through the BPS equation.

6.4.4 Interface morphology measurements and analysis

The interface shape was measured in a manner similar to the measurement of the growth rate, *ie* using the on-screen image put out by a CCD camera attached to a Zeiss microscope equipped with a 4x Nomarski objective. The sample was aligned to micrometers on the microscope stage, which were used to take interface shape measurements spaced by 500 μm.

Reported measurements were conducted on the crystal whose growth rate is reported in Figure 6.18. It was grown at steady translation rate of 8.5 μm/s, in the Bridgman mode of operation, with sensors A & B used as the control points to hold a gradient of 46°C/cm about the interface location. The shapes of the seeding interface and four other interface demarcation lines were measured (Figure 6.21). The line of intersection between the interface and the plane along which the crystal was sectioned is taken as the interface shape. Clearly, this does not offer any information on the three-dimensional shape of the interface. An effort was made to keep the sectioning plane parallel to the plane along which the gradient zone sensors were deployed, and to include the crystal axis. The interface shape was found to be tilted by an angle of 1.5° with respect to the growth axis. The tilt is real, since care was taken to ensure that the geometrically straight edge of the sample was parallel to the microscope's positioning micrometers. The error in measurement of the interface deflection is estimated to be less than +/− 10 μm (calculated by considering that error in the on-screen position measurement was at most +/− 2mm, which at a magnification of 245X, translates to a interface shape measurement error of +/− 10 μm). The accuracy of radial position was +/− 50 μm, the vernier accuracy of the x-axis micrometer. The maximum deflection (difference between the highest and lowest points on the interface) in the full-diameter portion of the crystal was 400 μm. In the seed well region, the maximum interface deflection was 600 μm. The interface shape measurements were made only over a 16 mm length near the seeding position. The diameter of the crucible was 14mm. The effective length of the melt volume changed from 75 mm to 55mm (corrected for the smaller melt diameter in the graphite melt contact) over this region, implying an aspect ratio change from 5 to 3.6 over the region of the interface shape measurements.

The interface shape is not constant, nor is it symmetric except in the seed well of the graphite seed electrode. The tilting of the interface could arise from many factors, for example, from eccentricity of the ampoule within the furnace cavity, or from non-uniformity of the thermal properties of the gradient zone material. The asymmetry is reduced within the seed well because the surrounding graphite helps to even out the heat flux. The fact that the interface shape changes over time is to be expected, even though the axial gradient is constant. The growth

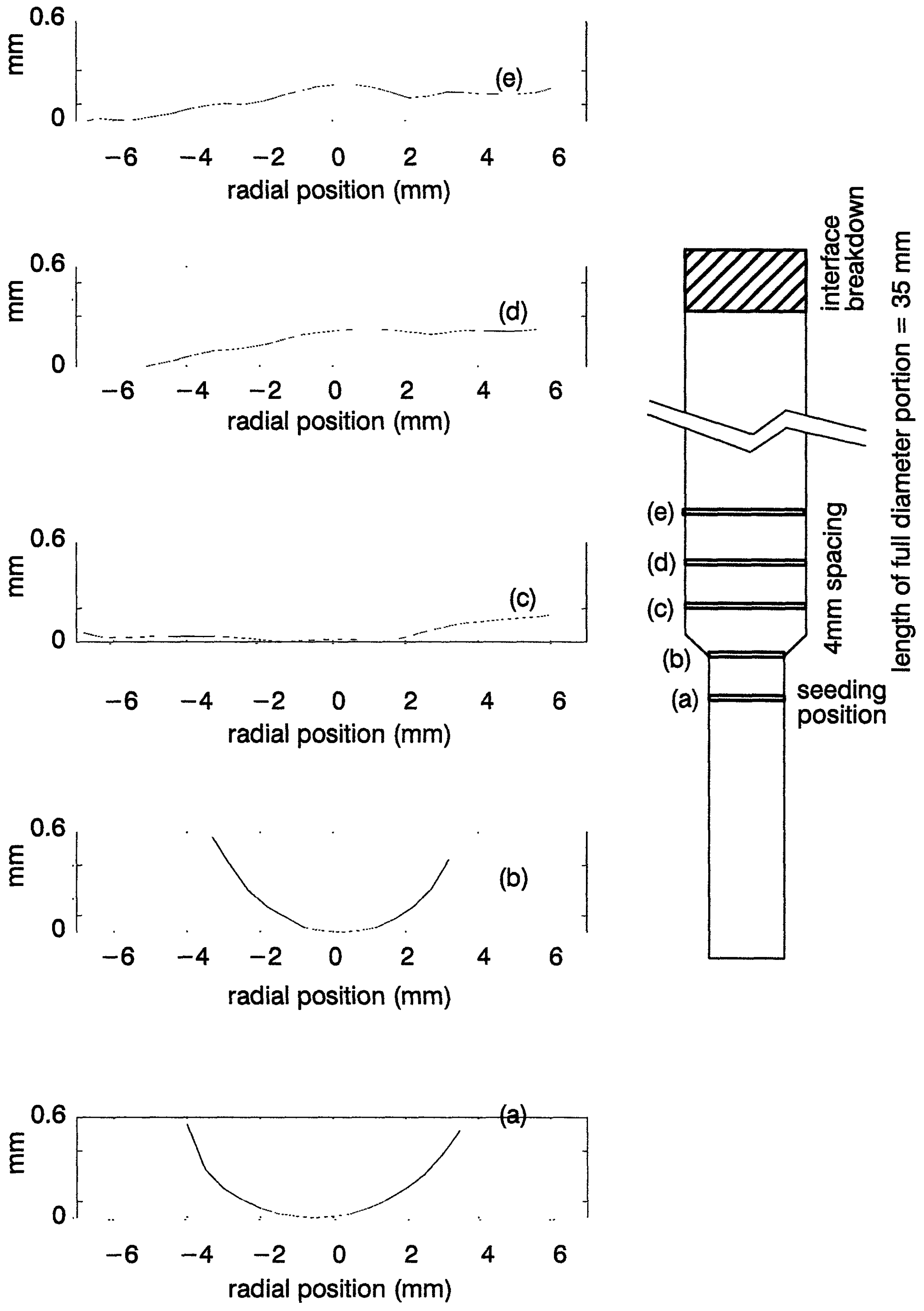

Figure **6.21** : Evolution of interface morphology along the growth direction, at the seeding end.

rate in this run exhibited an overshoot and undershoot, as discussed before. The interface relocation over the course of this run was 6mm. Some of the change in interface shape would be due to interface relocation. More importantly, the radial heat flux will change, as a result of changing thermal coupling, resulting in a change in shape. In the topmost interface demarcation line, we note a w-shape superposed on the canted interface. This, taken along with the radial segregation data to be presented below, suggests the presence of a toroidal flow cell in the melt.

6.4.5 Radial segregation measurements and analysis

Spreading resistance analyses were carried out in the radial direction at the same positions where the interface shape had been recorded. The measured data is to be compared with the calculated radial segregation profile. The calculations are based on Coriell and Sekerka's analysis[40], where the interface shape is taken to be given by the solution of a conductive heat flow analysis, and purely diffusive mass transport is assumed to be operative in the melt. The analytical expression developed by them is true for small deviations from planarity.

$$\frac{[C_{sl}(r) - C_{sl(0)}]}{C_{sl,av}(t)} \approx -\frac{V(t)}{D}(1-k)[W(r) - W(0)]$$

where $C_{sl}(r)$ is the dopant concentration at radius r, $C_{sl,av}(t)$ is the average concentration in the solid at the interface at that time, t, V(t) is the instantaneous velocity, D is the dopand diffusivity and W(r) is the interface morphology (the height of the interface at radius r, measured with respect to some reference position). The validity region of the equation is established by (i) $W \ll D/V$, where W is the maximum interface deflection, D the diffusivity of the dopant in the liquid, and V the growth rate; and (ii) the Fourier series that represents the interface shape should be capable of approximation by the first few terms. These conditions are satisfied by the measured morphologies in the full-diameter portion of the crystal (curves c,d, and e in Figure 6.21). Accordingly, these three interfaces were used in the analysis.

The agreement between the measured and calculated radial segregation profiles is poor (Figure 6.22). In all cases, the measured radial segregation is more severe than a purely diffusive case would allow. The measured segregation profile also shows the w-shape that a toroidal flow cell would create. These two points taken together indicate that a toroidal cell is indeed present, inspite of the slight asymmetry in the thermal field. The presence of a thin boundary layer (rather than an extended diffusive field) would explain the stronger segregation results. These conclusions are in agreement with the axial segregation data, which also indicated the presence of convection, and a boundary layer that was a few hundred microns thick. Radial segregation data did not reflect the interfacial tilt that had been measured.

6.5 Summary

Growth of Ga:Ge was carried out in the vertical Bridgman-Stockbarger technique with control sensors (spaced by 1 cm) located in the gradient zone.

- It was shown that the interface location is stabilized during the growth run (except for an initial transient) at growth rates upto 3 cm/hr (8.5 μm/s). The location was controlled to the point of interface breakdown due to constitutional supercooling. After the start-up transient, the location of the interface was controlled to within 50 μm.
- The interface morphology was found to be tilted, but almost planar, with a slight w-shape was superposed. The interface morphology was found to change during growth, even though the location was held fixed. This effect is attributed to changes in radial heat fluxes a different points in the growth crucible, the interface is very concave within the graphite seed well, due to the lower conductivity of graphite compared to molten Ge.
- Axial segregation data showed that convection is present but is weak, with the dopant profile falling very close to that of purely diffusive behavior. The k_{eff} value decreases by about 10% during growth. Use of the BPS formalism resulted in a boundary layer thickness estimate of around 450 μm.
- Radial segregation data confirmed the controlling influence of convection upon segregation, and gave additional evidence of the presence of a toroidal flow cell in the melt, by showing a w-shaped distribution across the diameter, and by not reflecting the interface tilt in the segregation.

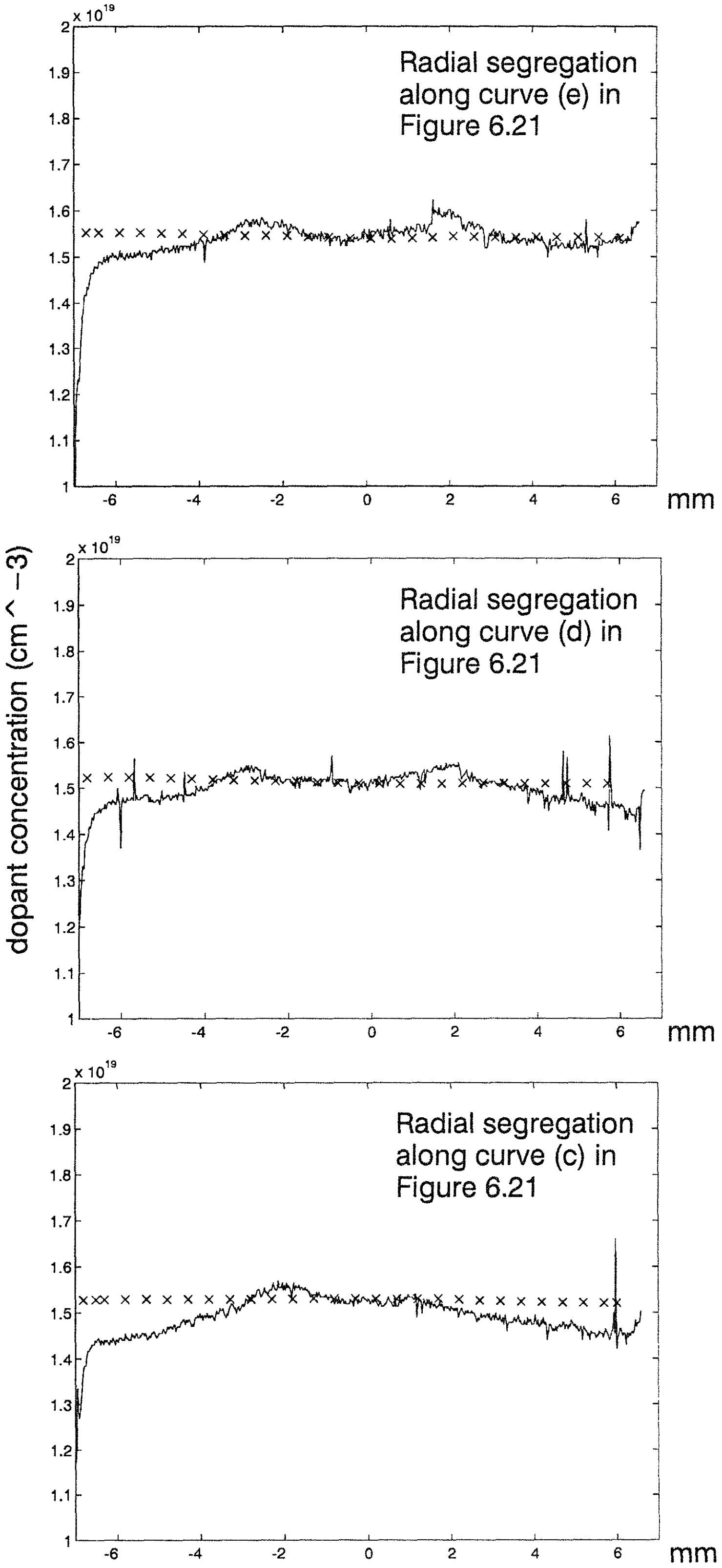

x : Coriell analysis
– : measured data.

Figure **6.22** : Radial segregation profiles (and calculated profiles, assuming diffusive transport)

Chapter 7 Conclusions

(i) The furnace can successfully be used in the gradient freeze mode of operation for controlling the growth rate and the axial temperature gradient about the growth interface. The use of a controller that can alter its control parameters as growth proceeds is considered important since the spacing between the sensor and the actuator of the control system is changing continuously. It was shown that in the gradient freeze mode of operation the growth rate can be controlled at speeds of 3 cm/hr (8.5 μm/s), and at axial gradients as low as 5°C/cm. It should be noted that the gradient zone design used here included an inconel liner, which resulted in high axial heat flows even at low axial gradients. The radial heat flux was also increased, but did not significantly affect the axial thermal profile, because the radial heat flux was small compared to the large axial heat flows caused by the inconel liners.

(ii) It was found in the Bridgman characterization phase of this work, that the presence of inconel enveloping the gradient zone increases the radial heat fluxes in the charge. With use of an alumina liner, radial heat losses were reduced.

(iii) It was found that the thermal conductivity of the insulation material used in the gradient zone was too high for the establishment of temperature gradients smaller than 15°C/cm. At low nominal gradients, the radial heat loss (though small) in the gradient zone became comparable to the axial heat flux in the center of the gradient zone, creating a 'dip' in the temperature profile. In conventional Bridman-Stockbarger furnaces, such dips are generally neglected.

(iv) The axial temperature profile in the heat-pipe based Bridgman furnace was found to be sensitive to the location of the heater. This is attributed to the limited ability of the heat-pipe to adequately compensate for excessive heat loss at its ends (considering that there are limitations to the heat fluxes that can be supported by the heat-pipe while still maintaining isothermality). Hence the use of a heat-pipe in a Bridgman furnace for the purpose of maintaining isothermality should be done with attention paid to the heat loss fluxes over the heat-pipe surface, particularly at the thick end-caps.

(v) Measurements of furnace wall temperature in the gradient zone, with an accuracy sufficient for use as a furnace control point, are subject to heat loss along the thermocouples. Due to the fact that the body of the thermocouple passes through a region with a large temperature gradient, substantive heat is conducted away from the junction to cause artificially low temperature readings. Hence the temperature sensors in the gradient zone should be of low conductivity and placed in such a fashion that this heat loss does not affect the junction temperature. This was achieved by having a length of thermocouple near the junction experience no temperature gradients.

(vi) In both the gradient freeze and the Bridgman modes of operation with the control thermocouples in the gradient zone, the control is more sensitive to noise in the thermocouple than when operated in the conventional manner. This is because simple proportional control is inadequate, and derivative and integral terms need to be incorporated into the control law for adequate response. The derivative term increases noise sensitivity. Hence high quality data acquisition and control systems need to be used.

(vii) During Ga:Ge crystal growth, with the furnace controlled in the conventional manner (at the hot and cold zones), the growth rate was found to differ substantially from the translation rate, due to transients in thermal coupling caused by “finite” (short) charge lengths. It was found that the thermal field in the gradient zone did not remain constant, even though the hot and cold zone temperatures were constant to within 0.25°C.

(viii) For growth of Ga:Ge in the Bridgman mode of operation, with the control sensors located in the gradient zone, it was shown that the transients associated with changing thermal coupling were compensated for, and that the axial temperature gradient in the vicinity of the crystal-melt interface held constant.

The interface location was also held fixed during the growth run, except for an initial transient. With a step in charge displacement rate from 2 cm/hr (5.5 μm/s) to 3 cm/hr (8.5 μm/s), the transient was slightly overdamped, and the growth rate settled at the final value within 3.5mm of growth. With a step from 0 to 3 cm/hr (8.5 μm/s), the initial transient in the growth rate was underdamped, exhibiting an overshoot of about 60%. Control over growth rate was demonstrated till the point of interface breakdown in the crystals grown.

(ix) Studies of the crystal-melt interface showed that its morphology changed during growth, though its axial position remained localized to within 1.5 mm of its original position. This was found to be related to the specifics of radial heat flow at different points in the growth ampoule. Within the graphite seed well of the ampoule, the interface was concave and symmetric. Improved planarity was observed in the full diameter portion, though the symmetry was degraded. In addition, a w-shaped morphology had developed, related to the formation of a toroidal flow cell in the melt. The increased curvature in the seed well is attributed to the relatively lower thermal conductivity of the graphite compared to germanium melt.

(x) Axial and radial spreading resistance analyses showed that there was convective interference with segregation behavior. Convection was weak, with the axial segregation behavior falling close to the purely diffusive segregation curve. The "boundary layer thickness" was estimated to be about 450 μm, using the BPS formulation. The radial segregation data also showed the presence of convection, and exhibited a w-shaped profile, related to the toroidal flow cell in the melt.

Chapter 8 Suggestions for future work

(i) The control algorithm used can and should be improved. This would reduce the magnitude of the observed start-up transients in growth rate. It would also reduce error with respect to the setpoints, after completion of the transient. A possible approach would be to develop a lumped-parameter model of the dynamics of the furnace, and use state-space control techniques[53]. Such an approach would make it possible to move the control points even closer to each other, since coupling between the two zones can be handled by a state-space representation.

(ii) Thermal coupling between the hot zone and the cold zone should be restricted to the charge – this maximizes controllabity of the interface, by reducing parasitic heat flows between the control points and the actuators. This would also simplify the dynamical model of the furnace (which is needed for effective state-space control techniques to be developed). In addition, it would make the heat transfer characteristics of the furnace approach those assumed in most heat transfer models of the Bridgman process (*viz.* an adiabatic gradient zone).

A possible approach[5] would be to develop a gradient zone that is encased in a skeleton of recrystallized alumina, and which is essentially a stack of quartz tori. Each torus would be evacuated, and filled with hollow glass spheres (which are commercially available), and having concentric, metallic radiation shields. The advantages of using a stack are: the gradient zone length can be changed between growth runs, if necessary; the increase in number of interfaces will reduce heat flow through the gradient zone between the top and bottom zones; an increased mechanical strength will be obtained by reducing the aspect ratio of the torus; and the breaks can be used for the insertion of sensors that reach the inner wall of the gradient zone. Filling the torus with hollow glass spheres and concentric metal rings increases mechanical strength. The glass beads increase scattering, which will reduce radiative heat loss in the radial direction of the gradient zone, and remove parasitic coupling between the hot and cold zones. Evacuating the torus that contains the glass spheres and the metal rings removes heat conduction through the gas phase. The metal rings will also serve to increase azimuthal symmetry of the temperature profiles in the gradient zone - thereby decreasing the sensitivity of the heat-flux distribution to inhomogenities in the conductivity of the gradient zone.

Another possible design would be to encase the glass beads in a silica cloth bag, which would be held in a canister of adjustable height (using a piston mechanism to change the aspect ratio of the gradient zone, and redistribute the beads at the same time. At the present time, it is difficult to conceive of a method whereby vacuum could also be used in this gradient zone design, which however has the advantage that the gradient zone width can be changed easily.

It would also be useful to redesign the furnace assembly – so that the furnace is not built by stacking the various elements on top of each other. Instead each zone should be supported independantly, through radial scaffolding. This will reduce parasitic heat flows between the hot and cold zones – and ensure that the zones communicate only through the charge volume. The use of a quartz, evacuated, and highly scattering gradient zone will reduce the thermal conductivity of the gradient zone considerably.

(iii) Thermocouples could be replaced by fiber optic black body radiation sensors. This would reduce the measurement problems caused by heat conduction along the thermocouple. Use of single mode fibers, if possible, would reduce the problem that might otherwise be caused by radiation entering into the fiber optic at points away from the "junction" where a hermetically sealed black body would be located.

(iv) Further studies are needed to understand how interface morphology can be held constant at all stages of the growth process, and then to develop an approach which permits active control of radial segregation, through stabilization of the interface location and of the morphology at that location. Finite element modeling efforts should be used to model the heat transfer characteristics and dynamics, both during the development process and during operation (through reduced-order models).

(v) With the interface localized, it might be feasible to introduce (radially through the gradient zone) image forming fiber optics at a specific location in the gradient zone to monitor the crystal growth process.

(vi) Given the rising importance of silicon-germanium alloys in gigahertz communications, the vertical Bridgman-Stockbarger furnace with the interface control modifications could be used to study the feasibility of single crystal growth of alloys of Si-Ge. At germanium concentrations higher than 20 or 25%, it will be necessary to replace the sodium-based inconel heat-pipes with TZM (Titania-Zirconia- strengthened Molybdenum) heat-pipes with Lithium as the working fluid. This would allow operation at temperatures in excess of 1100°C.

(vii) A continuous Bridgman technique might be feasible using the interface control techniques developed here. In such a process, charge is continually added to the melt, from the top of the furnace. The crucible is open at both ends, and the grown crystal is withdrawn from the tube (crucible) that confines the melt. The growth is best started using a full-diameter seed, since that would remove the perturbations involved in increasing the crystal diameter. The full-diameter seed would be held in an appropriately designed chuck and withdrawn to accomplish growth. The use of a full diameter seed will also make it possible to use just one tube, open at both ends, as the melt confinement system. The use of an open, tubular crucible to contain the melt implies that control over the crystal-melt interface be tight. The location of the interface must be known a priori and it must not vary during growth. This work presents a method by which that condition can be met, in principle. Development of continuous Bridgman would mean that the problems of segregation caused by the batch nature of crystal growth are removed. It also the advantage that the grown crystal surface is free, as in the Czochralski technique, thereby reducing the crucible induced thermal stresses which are an issue in Bridgman growth.

Appendix A. Spreading Resistance Characterization

A.1. Introduction

Figure A.1 below is a schematic of the system used to make spreading resistance measurements of the Ge:Ga samples. It consists of the pneumatic and timing subsystems of an old Solid State Measurements Inc. ASR-100 unit, integrated with a Keithley 220 current source and Keithley 615 electrometer.

The current source and the electrometer were controlled by a PC across a HPIB bus. The pneumatic subsystem moves the sample between measurements (to within 2.5 microns) and allows the probe to settle on the sample surface at a slow, controlled rate. The rising edge of a voltage pulse produced by the motor-driven cam timing mechanism of the ASR-100 was used by the PC to synchronize the measurement process. The cam timing mechanism also drove the pneumatic subsystem to lower the probe slowly onto the sample, raise the probe after exactly 1 second, and move the sample by the predetermined amount between spreading resistance measurements while the probe was not in contact.

The current source was configured to produce a 50 ms pulse of current only while the probe was in contact with the sample. The electrometer's autoranging function was disabled to increase measurement accuracy, and the instrument zeroed itself after every measurement. The electrometer was triggered over the HPIB bus to take a single reading slightly after the probe made contact. The voltage reading was immediately brought to the PC over the HPIB bus for on-screen display as a spreading resistance value at that point. After the requisite number of points were measured, the data was plotted on paper, if so desired.

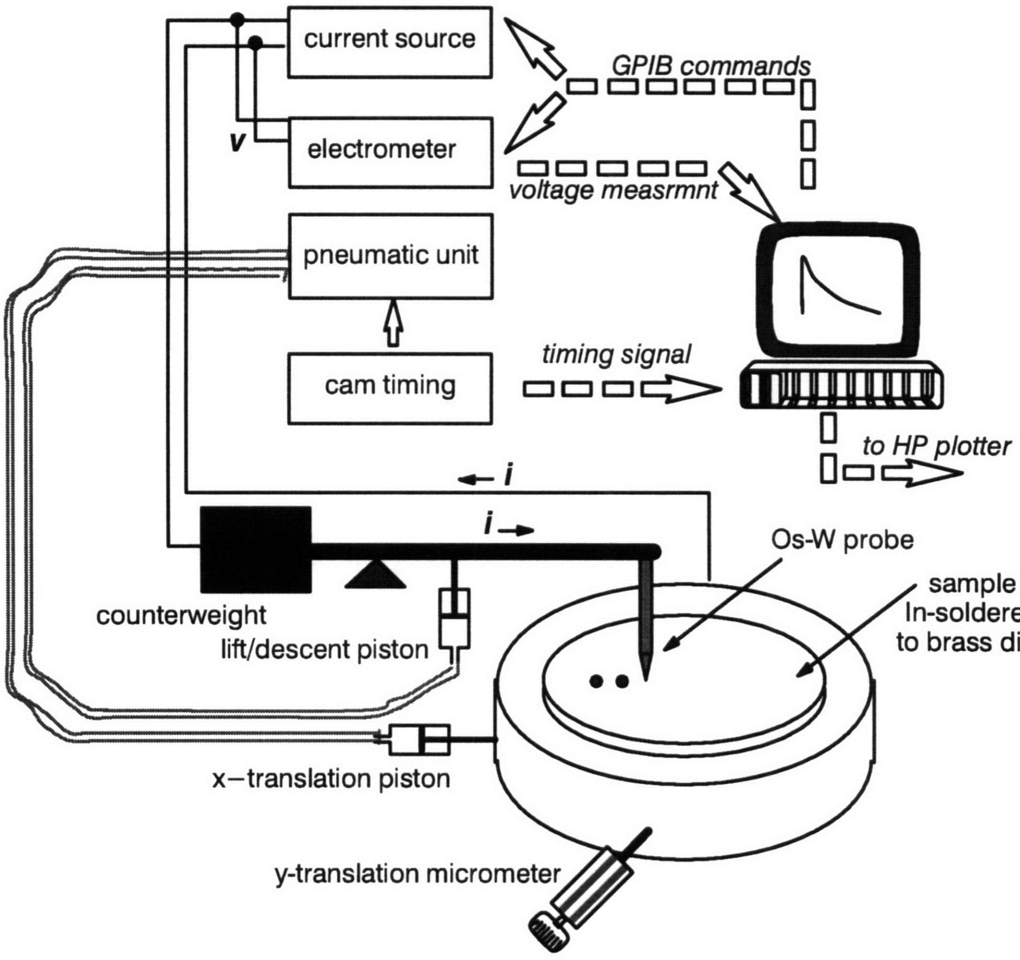

Figure **A.1** : Spreading Resistance System Schematic

The sample was lapped on an optically-flat glass plate with Harrick Fine Polishing powder (17 micron garnet), and then chemo-mechanically polished on a Rodel #204 pad for 30 minutes using a solution of 600 ml DI water, 400 ml colloidal silica (Syton) and 60 ml of 5.25 vol% NaOCl (Clorox). The pad was changed for every 10 polishes or if the pad surface had become prematurely abraded. It was found that the polishing solution could be left to stand for a maximum of 4 days, with no deterioration in polishing efficacy. It was established that this procedure yielded Germanium surfaces that were suitable for making spreading resistance measurements with better than 5% accuracy and reproducibility.

The spreading resistance values were also stable over time, as long as the surface was cleaned with a detergent (Ivory) and hand-washed in DI water immediately prior to measurement. It was also found that the spreading resistance values did not depend materially on whether or not the surface was etched in CP-4 or kept as-polished. The advantage of etching prior to measurement was that observed variations in spreading resistance could be immediately, and precisely correlated with features seen via etching. The samples were ultrasonically bonded onto brass discs with In-Sn solder as the backside contact for single-probe spreading resistance measurements. Etching of the brass disc also occurred when the sample was etched to reveal interface demarcation lines (10 second dip in 49% HF : 30% H_2O_2 : glacial CH_3COOH :: 1:1:1).

A.2. Measurement Characteristics

The various sources of noise that might impact the sensitivity of measurements made by the system in use were studied. To obtain the data in Figure A.2, the probe was held stationary at a given point on the sample, and spreading resistance readings taken in an otherwise normal manner, at various current values. Comparison of the readings taken at 1 mA and at 100 μA indicates that at the lower current levels, the measurement accuracy is limited by the resolution of the electrometer (10 μV). Hence spreading resistance measurements were made typically at 1 mA. Considering the resistivity of samples generated in this work, the voltage drop across the probe and sample was less than 10mV (which is roughly ½kT at 300K). Figure A.2 also shows that, even under the best of conditions, when the probe is resting motionless at a given point on the sample, the reproducibility of the spreading resistance measurement is about ± 5%. This might be considered below par for the technique[63], but not by too much. Spreading resistance measurements in this work were typically made at 1 mA. It was also ensured that the measured values were not affected by the polarity of the applied current of 1 mA.

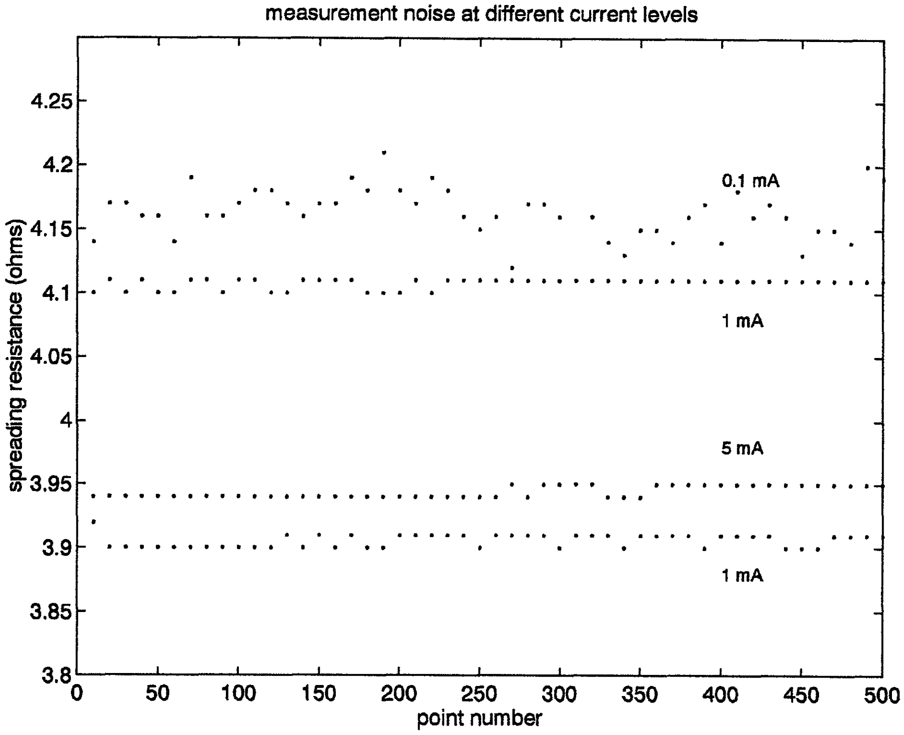

Figure **A.2** : Measurement of spreading resistance at a single point on the sample at different levels of impressed current. The figure also indicates the limits of reproducibility of the spreading resistance data.

In Figure A.3, each curve corresponds to the spreading resistance at 200 points at 25 micron increments (thereby spanning a 5 mm distance) perpendicular to the growth axis in a Czochralski-grown sample from Eagle Picher, Inc. The two runs were separated by 15 microns, and since the sample was reasonably uniform, the two runs are expected to be very similar. This figure is a typical example of the 5% reproducibility that was observed during spreading resistance measurements, even over extended data collection runs.

A.3. Calibration of the Spreading Resistance Probe

The carrier concentration and mobility of the calibration specimens were measured by Hall effect measurements using square van der Pauw structures. This permitted the conversion of the spreading resistance data to carrier concentration values. The calibration data used are tabulated in Table A.1 and graphed in Figure A.4, along with least square fits to the data. The x-intercept of the straight line fit in the second plot of Figure A.4 is 0.5 ohms, which was indeed the resistance of the lead wires, as measured by shorting out the probe-sample contact. There is, unfortunately, considerable spread in the carrier concentration data, which limits the reliance that can be placed on the absolute values of the carrier concentrations determined through this calibration. In the third and fourth plots of Figure A.4, the measured mobilities and resistivities are plotted against the measured carrier concentration in the calibration samples, along with data from the literature.

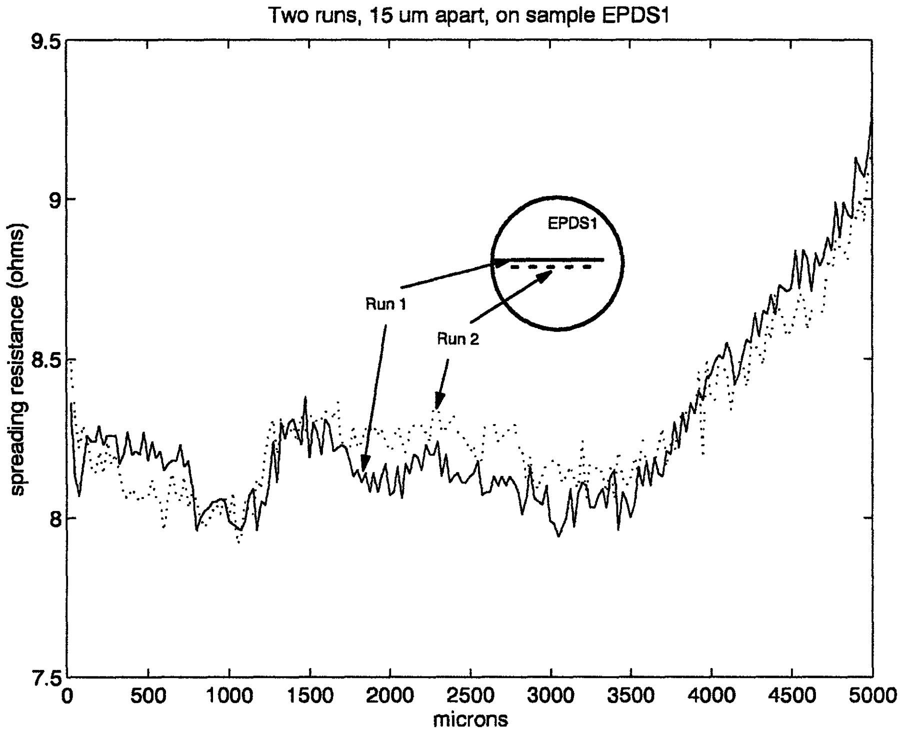

Figure **A.3** : Better than 5% reproducibility in spreading resistance data, as shown by two parallel runs spaced by 15μm on a calibration sample.

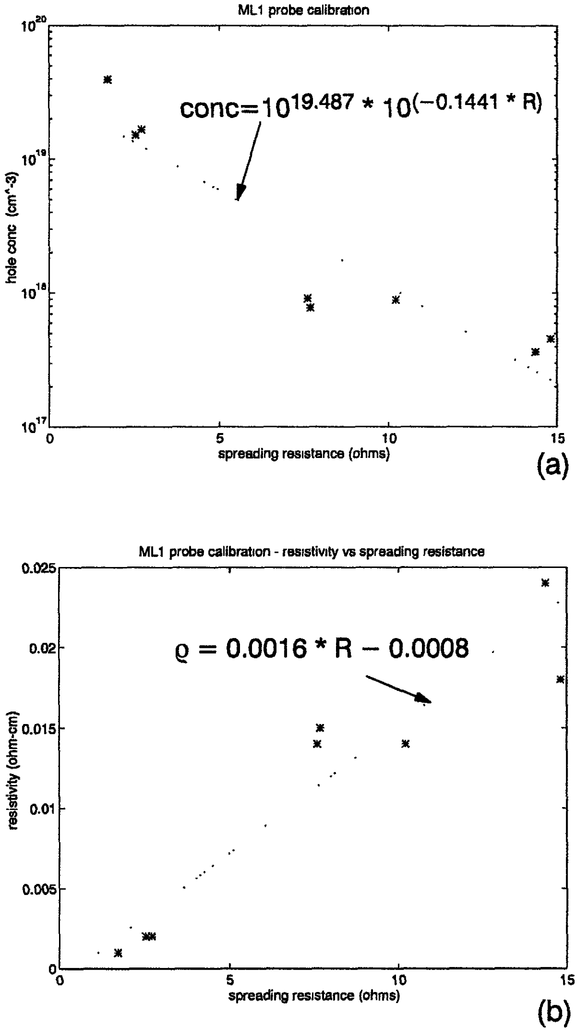

Figure **A.4** : Calibration of probe "ML1".
(a) gives the hole concentration *vs* spreading resistance and a first order semilog fit to the data,
(b) gives resistivity *vs* spreading resistance along with a first order fit to the data.
The data points are also recorded in Table A.1

Table A.1 : Spreading resistance calibration sample information.

Sample name	Avg. Spreading Res(ohms)	Carrier conc (cm^{-3})	Mobility (cm^2/Vs)	Resistivity (ohm−cm)
B4−1	1.71	3.94×10^{19}	139	0.001
C1−1	2.71	1.65×10^{19}	187	0.002
FSF−2	2.53	1.51×10^{19}	203	0.002
D4−2	10.2	8.91×10^{17}	516	0.014
EPDS3	7.60	9.13×10^{17}	485	0.014
D4−1	7.68	7.77×10^{17}	545	0.015
C2−1	14.36	3.63×10^{17}	705	0.024
C2bRd1	14.81	4.56×10^{17}	748	0.018
Q11		1.486×10^{18}	394	0.011

Sample name	Avg. Spreading Res(ohms)	Carrier conc (cm^{-3})	Mobility (cm^2/Vs)	Resistivity (ohm−cm)
P11		4.783×10^{19}	124	0.001
E11		2.831×10^{19}	258	8.5×10^{-4}
C3bLd1		1.135×10^{19}	208	0.003

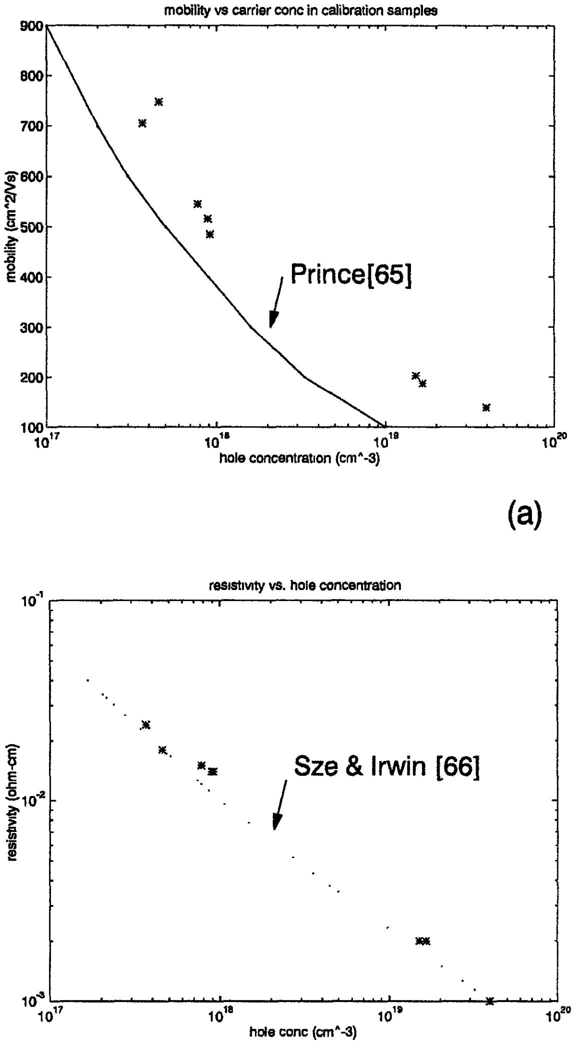

(a)

(b)

Figure **A.5** : (a) is a record of the measured mobility vs hole concentrations in the calibration samples.
(b) is a record of the measured resistivity vs hole conc. in the calibration samples.
Data points are also recorded in Table A.1

Appendix B. Listing of furnace data acquisition and control program (adc5ver3.c) segments

B.1 The data acquisition and control program

```
/**********     MAIN LINE     ***********/
main()
{
  count_time = time(tloc);
  create_low_pass();
  curses_init();
  ad_da_init();
  file_setup();
  az_set();  /** set up the Azonix data acquisition box **/

  erase();  /** clear screen of set-up messages **/

  mvaddstr(SCRHFDWN,SCRLFT,"I hope you have set per1=2s on the PC, and
made sure that the Azonix is transmitting to the MassComp now.");
  refresh();

  batter_up();  /** Stopping stamp-collecting, doing science **/

  point1=0; point2= 0; point3 = 0; point4=0; point5=0;  point6=0; /*shutdown */
  da_out();  tell_guys();  /** update D/A converters and displays **/
  endwin();  /*** get out of curses ***/
}
```

B.2 The Parks-McClellan low pass filter

```
/*****************************************************************
*   This sets the lowpass filter, used by read_temp in noise reduction
*****************************************************************/
create_low_pass()
{
  h_lp[ 0]=0.0027/0.9751; h_lp[ 1]=0.0042/0.9751;  h_lp[ 2]=0.0070/0.9751;
  h_lp[ 3]=0.0108/0.9751;  h_lp[ 4]=0.0155/0.9751;  h_lp[ 5]=0.0210/0.9751;
  h_lp[ 6]=0.0273/0.9751;  h_lp[ 7]=0.0341/0.9751;  h_lp[ 8]=0.0410/0.9751;
  h_lp[ 9]=0.0478/0.9751;  h_lp[10]=0.0540/0.9751;  h_lp[11]=0.0593/0.9751;
  h_lp[12]=0.0634/0.9751;  h_lp[13]=0.0659/0.9751;  h_lp[14]=0.0668/0.9751;
  h_lp[15]=0.0659/0.9751;  h_lp[16]=0.0634/0.9751;  h_lp[17]=0.0593/0.9751;
  h_lp[18]=0.0540/0.9751;  h_lp[19]=0.0478/0.9751;  h_lp[20]=0.0410/0.9751;
```

```
  h_lp[21]=0.0341/0.9751;  h_lp[22]=0.0273/0.9751;  h_lp[23]=0.0210/0.9751;
  h_lp[24]=0.0155/0.9751;  h_lp[25]=0.0108/0.9751;  h_lp[26]=0.0070/0.9751;
  h_lp[27]=0.0042/0.9751;  h_lp[28]=0.0027/0.9751;
}
```

B.2. The PI control segment of “adc5ver3.c”

```
/****************************************************
*   The PI temperature control subroutine
****************************************************/
int tpid(p_c,i_tm,l_point,err,l_err)
float p_c, i_tm, err, l_err, l_point;
{
  float tauS, value;
  int point;
  tauS = 2.0; /* sampling time */
  value=l_point+p_c*(1.0+(0.5*tauS/i_tm))*err-p_c*(1.0-(0.5*tauS/i_tm))* l_err;
  if (value > MAXSIG)
      point = (int)MAXSIG;
  else if (value < -MAXSIG)
      point = -MAXSIG;
  else
      point = (int)value;
  return(point);
}
```

B.3. The segment of “adc5ver3.c” in charge of gain scheduling

```
/**********************************************************
* Read the loop constants file, and compute the required constants.
 *********************************************************/
get_loop_consts(zone_name,file_name,parameters,curr_loc)
char zone_name[7];
char file_name[80];
float parameters[];
float curr_loc;
{
  float trash;
  float kp_a,taui_a,kp_b,taui_b;

  if((in = fopen(file_name,"r")) == NULL)
    {
     fprintf(stderr,"OPEN FAILED %s\n",file_name);
```

```
    fflush(stderr); shut_off();
   }
 if(zone_name[5] == '0')
   {
    fscanf(in,"%f",&kp_a); fscanf(in,"%f",&taui_a);  fscanf(in,"%f",&kp_b);
    fscanf(in,"%f",&taui_b);  fscanf(in,"%f",&parameters[2]);  fclose(in);
   }
 else if(zone_name[5] == '1')
   {
    fscanf(in,"%f",&trash); fscanf(in,"%f",&trash); fscanf(in,"%f",&trash);
    fscanf(in,"%f",&trash); fscanf(in,"%f",&trash);
    fscanf(in,"%f",&kp_a); fscanf(in,"%f",&taui_a); fscanf(in,"%f",&kp_b);
    fscanf(in,"%f",&taui_b); fscanf(in,"%f",&parameters[2]); fclose(in);
   }
 /* now we compute the actual constants based on a linear fit */
 parameters[0] = kp_a + (location/50)*(kp_b - kp_a);
 parameters[1] = taui_a + (location/50)*(taui_b - taui_a);
}
```

Bibliography

[1] J.J. Gilman (ed), *The Art and Science of Growing Crystals*, Wiley, New York,1963.

[2] G. Packeiser, H. Schink, H. Kniepkamp, "Substrate material related yield aspects for GaAs LSI circuits", in *Semi-Insulating III-V Materials*, Ohmsha Ltd, 1986, p.561.

[3] E.S. Meieran, "Industrial implications of crystal quality", in : *Characterization of Crystal Growth Defects by X-Ray Methods, B.K. Tanner and D.K. Bowen (eds)*, Plenum, New York, 1980. p.14.

[4] S. Wolf and R.N. Tauber, *Silicon Processing for the VLSI Era - Processing Technology,* Vol **1**, Lattice Press, CA, 1986, p.51

[5] A.F. Witt, Private communication.

[6] S.K. Ghandhi, *VLSI Fabrication Principles*, Wiley-Interscience, New York, p.98

[7] W. Rosch and F. Carlson, "Computed stress fields in GaAs during vertical Bridgman growth", *Journal of Crystal Growth,* **109** (1991) 75.

[8] G. Müller and A. Ostrogorsky, "Convection in melt growth", in : *Handbook of Crystal Growth, Vol.* ***2b****, D.T.J. Hurle (ed).*, Elsevier, 1994, p.711

[9] D.J. Carlson and A.F. Witt, "Microsegregation in conventional Si-doped LEC GaAs", *Journal of Crystal Growth,* **108** (1991) 508.

[10] D.T.J. Hurle and B. Cockayne, "Czochralski Growth", in : *Handbook of Crystal Growth, Vol. 2a, D.T.J. Hurle (ed).*, Elsevier, 1994. p.116

[11] A.S. Jordan, A.R. Von Neida and R. Caruso, "The theoretical and experimental fundamentals of decreasing dislocations in melt grown GaAs and InP", *Proceedings of the 8th International Conference on Crystal Growth, York, England, July 1986, Journal of Crystal Growth*, **76** (1986) 243.

[12] K.W. Kelly, K. Koai, and S. Motakef, "Model-based control of thermal stresses during LEC growth of GaAs, Part I : Validation of thermal model", *Journal of Crystal Growth*, **113** (1991) 254; K.W. Kelly, S. Motakef, and K. Koai, "Part II : Crystal growth experiments", *Journal of Crystal Growth*, **113** (1991) 265.

[13] W.R. Wilcox and T. Fu, "Influence of insulation on stability of interface shape and position in the vertical Bridgman-Stockbarger technique", *Journal of Crystal Growth,* **48** (1980) 416.

[14] E.M. Momberg, H. Brown and C.E. Bonner, "The dynamic gradient freeze growth of InP", *Journal of Crystal Growth*, **94** (1989) 109.

[15] D.J. Carlson, Private communication.

[16] D. Hofmann, T. Jung, and G. Müller, "Growth of 2 inch Ge : Ga crystals by the dynamical vertical gradient freeze process and its numerical modelling including transient segregation", *Journal of Crystal Growth*, **128** (1993) 213.

[17] C.R. Abernathy, A.P. Kinsella, A.S. Jordan, R. Caruso, S.J. Pearton, H. Temkin, and H. Wade, "Growth and characterization of low defect GaAs by vertical Gradient Freeze", *Journal of Crystal Growth*, **85** (1987) 106.

[18] W.A. Gault, E.M. Momberg, and J.E. Clemans, "A novel application of the vertical Gradient Freeze method to the growth of high quality III-V crystals", *Journal of Crystal Growth*, **74** (1986) 491.

[19] A.F. Witt, Private communication.

[20] C.A. Wang, A.F. Witt and J.R. Carruthers, "Analysis of crystal growth characteristics in a conventional vertical Bridgman configuration", *Journal of Crystal Growth,* **66**(1984) 299.

[21] C.W. Lan, and C.C. Ting, "Numerical investigation on the batch characteristics of liquid encapsulated vertical Bridgman crystal growth", *Journal of Crystal Growth*, **149** (1995) 175.

[22] P.G. Barber, R.F. Berry, W.J. Debnam, A.L. Fripp, G. Woodell, and R.T. Simchick, "Growth rates and interface shapes in germanium and lead tin telluride observed in-sity, real-time in vertical Bridgman furnaces", *Journal of Crystal Growth*, **147** (1995) 83.

[23] C-H. Hirsch, M.S. Thesis, "Analytic approach to the determination of the crystal-melt interface morphology in a vertical Bridgman-Stockbarger geometry", MIT, Cambridge, July 1989.

[24] P.C. Sukanek, "Deviation of freezing rate from translation rate in the Bridgman-Stockbarger technique" – "I. Very low translation rates", *Journal of Crystal Growth*, **58** (1982), 208. and "II. Moderate translation rates", *Journal of Crystal Growth*, **58** (1982) 219.

[25] C. Batur, W.M.B. Duval, and N.B. Singh, "Solid-liquid interface profile control for transparent multizone Bridgman type crystal growth furnaces", *Advances in Instrumentation and Control (Proceedings of the ISA 90 International Conference and Exhibit)*, **45**, (1990) 921.

[26] S. Miyazawa, "Shaped melt lowering (SML) : a novel growth technique permitting $k_{eff} = 1$", *Journal of Crystal Growth*, **60** (1982), 331.

[27] C.A. Wang, Ph.D. Thesis, "Crystal growth and segregation in vertical Bridgman configuration", MIT, Cambridge, February 1984.

[28] H. Wenzl, Private communication.

[29] T.Jasinski and A.F. Witt, "On control of the crystal-melt interface shape during growth in a vertical Bridgman configuration", *Journal of Crystal Growth,* **71** (1985) 295.

[30] E. Momberg, "Bridgman and related growth techniques", in : *Handbook of Crystal Growth, Vol. 2a, D.T.J. Hurle (ed)*. Elsevier, 1994.

[31] P.S. Ravishankar, "Liquid encapsulated Bridgman (LEB) method for directional solidification of silicon using calcium chloride", *Journal of Crystal Growth*, **94** (1989) 62.

[32] C.E. Chang and W.R. Wilcox, "Control of interface shape in the vertical Bridgman-Stockbarger technique", *Journal of Crystal Growth*, **21** (1974) 135.

[33] E.D. Bourret and A.F. Witt, "Seeded crystal growth of pseudobinary systems with large liquidus-solidus separation", *Advances in Ceramics,* **5** (1983) 159.

[34] A.F. Witt, H.C. Gatos, M. Lichtensteiger, and C.J. Herman, "Crystal growth and segregation under zero gravity : Ge", *Journal of the Electrochemical Society,* **125** (1978) 1832.

[35] D.H. Matthiesen, M.J. Wargo, S. Motakef, D.J. Carlson, J.S. Nakos and A.F. Witt, "Dopant segregation during vertical Bridgman-Stockbarger growth with melt stabilization by strong axial magnetic fields", *Journal of Crystal Growth*, **85** (1987) 557.

[36] R.S. Feigelson and R.K. Route, "Vertical Bridgman growth of $CdGeAs_2$ with control of interface shape and orientation", *Journal of Crystal Growth*, **49** (1980) 261.

[37] P.S. Dutta, K.S. Sangunni, H.L. Bhat, and V. Kumar, "Experimental determination of melt-solid interface shapes and actual growth rates of gallium antimonide grown by vertical Bridgman method", *Journal of Crystal Growth*, **141** (1994), 476.

[38] U. Möller, B.O. Hildmann and G. Bähr, "Shape of the solid-liquid interface and dopant distribution of Bridgman grown Ge : Ga", *Journal of Crystal Growth*, **131** (1993) 165.

[39] K. Koai, K. Sonnenberg, and H. Wenzl, "Influence of crucible support and radial heating on the interface shape during vertical Bridgman GaAs growth", *Journal of Crystal Growth*, **137** (1994) 59.

[40] S.R. Coriell and R.F. Sekerka, "Lateral solute segregation during unidirectional solidification of a binary alloy with a curved solid-liquid interface", *Journal of Crystal Growth*, **46** (1979) 479.

[41] S.R. Coriell, R.F. Boisvert, R.G. Rehm, and R.F. Sekerka, "Lateral solute segregation during unidirectional solidification of a binary alloy with a curved solid-liquid interface - II : Large departures from planarity", **54** (1981) 167.

[42] J.-J. Favier, "Macrosegregation - I Unified analysis during non-steady state solidification", *Acta Metallurgica*, **29** (1981) 197. and "Macrosegregation - II A comparative study of theories", *Acta Metallurgica*, **29** (1981) 205.

[43] A. Rouzaud, D. Camel, and J.J. Favier, "A comparative study of thermal and thermosolutal convective effects in vertical Bridgman crystal growth", *Journal of Crystal Growth*, **73** (1985) 149.

[44] P.M. Adornato and R.A. Brown, "Convection and segregation in directional solidification of dilute and non-dilute binary alloys : Effects of ampoule and furnace design", *Journal of Crystal Growth*, **80** (1987) 155.

[45] D.H. Kim and R.A. Brown, "Transient simulations of convection and solute segregation of GaAs growth in gradient freeze furnace", *Journal of Crystal Growth*, **109** (1991) 66.

[46] A.F. Mills, *Basic Heat and Mass Transfer*, Irwin, Chicago, 1995, p. 562

[47] W.W. Bienert, "Isothermal heat pipes and pressure controlled furnaces", *Isotech Journal of Thermometry*, **2**, No.1 (1991) 32.

[48] E.P. Martin, A.F. Witt, and J.R. Carruthers, "Application of a heat pipe to Czochralski growth, Part I : Growth and segregation behavior of Ga-doped Ge", *Journal of the Electrochemical Society*, **126** (1979) 284.

[49] Y.S. Touloukian (ed), *Thermophysical Properties of High Temperature Solid Materials*, **Vol 12**, MacMillan Co, NY, 1967.

[50] A.V. Oppenheim and R. Schaefer, *Discrete Time Signal Processing*, Prentice Hall, 1989 p.415

[51] K. Ogata, *Modern Control Engineering*, 2nd ed., Prentice Hall, 1990, p.595

[52] S.S. Papa Rao, J. Guzek and A.F. Witt, "Thermal characteristics of a Heat Pipe Based Vertical Bridgma System with Growth Rate Stabilization", Abstract bulletin and oral presentation at the Ninth American Conference on Crystal Growth, Baltimore, August 1-6, 1993.

[53] G.F. Franklin, J.D. Powell, and M.L. Workman, *Digital Control of Dynamic Systems (2nd ed)*, Addison-Wesley, 1992, p.222

[54] T. Jasinski and A.F. Witt, Private communications

[55] J.A. Hubert, A.L. Fripp, Jr, and C.S. Welch, "Resolution of the discrepancy between temperature indicated interface and radiographically determined interface in a vertical Bridgman furnace", **131** (1993) 75.

[56] R.B. Bird, W.E. Stewart, and E.N. Lightfoot, *Transport Phenomena,* John Wiley & Sons, New York, 1960, p.250

[57] W.M. Rohsenow and H.Y. Choi, *Heat, Mass and Momentum Transfer,* Prentice Hall, N.J, 1961.

[58] Inconel 601 Datasheet, Inco Alloys International, Inc, Huntington, WV 25705.

[59] M. Lichtensteiger, Private communication

[60] J-J Favier, "Initial transient segregation during unidirectional solidification of a binary alloy in a furnace with thermal damping", *Journal of Crystal Growth*, **49** (1980) 373.

[61] W.A. Tiller, K.A. Jackson, J.W. Rutter, and B. Chalmers, "The redistribution of solute atoms during the solidification of metals", *Acta Metallurgica*, **1** (1953) 428.

[62] V.G. Smith, W.A. Tiller, and J.W. Rutter, "A mathematical analysis of solute redistribution during solidification", *Canadian Journal of Physics*, **33** (1956) 723.

[63] A.F. Witt, M. Lichtensteiger, and H.C. Gatos, "Experimental approach to the quantitative determination of dopant segregation during crystal growth on a microscale: Ga doped Ge", *Journal of the Electrochemical Society,* **120** (1973) 1119

[64] M.J. Wargo and A.F. Witt, "Determination of the Peltier coefficient from current induced growth layers : InSb / Melt", *Journal of Crystal Growth*, **66** (1984) 289.

[65] M.B. Prince, "Drift Mobility in Semiconductors I, Germanium", *Phys. Rev.* **92** (1953) 681.

[66] S.M. Sze and J.C. Irwin, "Resistivity, Mobility and Impurity levels in GaAs, Ge and Si at 300 K", *Solid State Electronics,* **9** (1966) 143.